Functional Photonic Structures Fabricated by 3D Laser Lithography

Zur Erlangung des akademischen Grades eines

Doktor-Ingenieurs

von der KIT-Fakultät für Elektrotechnik und Informationstechnik
des Karlsruher Instituts für Technologie (KIT)

genehmigten

Dissertation

von

Dipl.-Phys. Philipp-Immanuel Dietrich

geboren in

Mainz, Deutschland

Tag der mündlichen Prüfung: 30.06.2022
Hauptreferent: Prof. Christian Koos
Korreferent: Prof. Dr. Dr. h. c. Wolfgang Freude
apl. Prof. Dr. Hendrik Hölscher

Table of Contents

Table of Contents ..... **i**

Preface ..... **vii**

Kurzfassung ..... **x**

Achievements of the Present Work ..... **xiv**

1 Introduction **1**

2 3D Laser Lithography **5**

2.1 Two-Photon Polymerization 5

2.2 Resist for Two-Photon Polymerization 9

2.3 Resolution of Two-Photon Lithography 14

3 Selected Application Fields of 3D-printen Micro-Optical Structures **26**

3.1 Material Platforms for Integrated Photonic Systems 26

3.2 Monolithic and Heterogeneous Integration 31

3.3 Hybrid Integration 33

3.4 Hybrid Integration with 3D-printed Micro-Optics 35

3.5 Ground-Based Observation of Stars 39

3.6 Scanning Probe Microscopy (SPM) 42

3.7 Atomic Force Microscopy (AFM) 43

3.8 Scanning Near-Field Optical Microscopy (SNOM) 46

4 In situ 3D Nano-Printing of Freeform Coupling Elements for Hybrid Photonic Integration **51**

4.1 Introduction 53

4.2 Concept, Design, and Fabrication 56

4.3 Experimental Verification and Discussion 58

4.3.1 Coupling experiments with facet-attached lenses. 59

4.3.2 Compact Assemblies with Facet-Attached Freeform Mirrors 61

4.3.3 Coupling Experiments with Facet-Attached Optical Beam-Expanders 63
4.3.4 Summary and Outlook 67

5 Printed Freeform Lens Arrays on Multi-Core Fibers for Highly Efficient Coupling in Astrophotonic Systems 69
5.1 Introduction 70
5.2 Concept, Design, and Fabrication 72
5.2.1 Simulation and Design 72
5.2.2 Fabrication by 3D-printing 75
5.3 Characterization and Measurement of Coupling Efficiency 75
5.4 Demonstration as a Tip/Tilt Sensor 76
5.4.1 Adaptive Optics Testbed 76
5.4.2 Use as a Tip/Tilt Sensor 77
5.4.3 Summary and Outlook 79

6 3D-printed Scanning Probe Microscopes with Integrated Optical Actuation and Read-Out 81
6.1 Device Concept, Fabrication, and Characterization 85
6.2 Atomic Step-Height Resolution 89
6.3 Measurements in Liquids 90
6.4 3D-printed SNOM Engines 93
6.5 Wafer-Level Fabrication of SPM Arrays 95
6.6 Summary and Outlook 98

7 Thesis Summary and Outlook 100
7.1 Summary 100
7.2 Outlook and Future Work 102
Reliability Demonstration 102
Fabrication Speed 104

Appendix 109

A. 3D-printed Lenses and Mirrors for Optical Coupling 111
A.1 Methods 111
A.2 Determination of Surface Roughness by Atomic Force Microscopy (AFM) 117

A.3 Coupling Experiments with Facet-Attached Lenses 118
A.4 Power-Current Curves for Lasers With and Without Lenses 119
A.5 Fresnel Reflection in Low-Index Contrast Micro-Optical Systems (LIMOS) 120
A.6 Absorption Measurement of Photoresist 122
A.7 Coupling to TriPleX Chips 124
A.8 Reproducibility and Accuracy 125

B. 3D-printed Functional Microsystems 128
B.1 Architecture and Optical Design of the Printed SPM Engine 128
B.2 Simulation and Measurement of Cantilever Deformation 130
B.3 Characterization of the AFM Position Detector 133
B.4 Thermo-Mechanical Simulation and Modeling 134
B.5 Highly Sensitive Position Readout 140
B.6 Scanning Near-Field Optical Microscope (SNOM) Measurements 142
B.7 Wafer-Level Fabrication and Reproducibility of SPM Engines 147
B.8 Controlling and Fine-Tuning of Individual SPM Cantilevers 149

C. Bibliography 153

D. Abbreviations and Symbols 169
D.1 Abbreviations 169
D.2 Symbols 171

Danksagung 175

List of Publication 177
Journal publication 177
Patent publications 178
Conference publications 178

Preface

Integrated photonic systems are critical to a wealth of highly relevant applications in science and industry ranging from optical communications over metrology to astro-photonics. They also play an integral role in the development of novel technologies such as quantum computing and devices for solid-state light detection and ranging (LiDAR).

From an engineering perspective, integrated photonic systems mainly rely on functional waveguides that generate, guide, modulate, and detect light. There are two main approaches to realize integrated photonic systems. The first aims at embedding all functionalities monolithically, implemented by processes that are compatible with wafer-level fabrication. This approach allows highly scalable and cost-effective mass production, as it can rely on mature processes developed for the production of electronic integrated circuits. However, it requires multi-billion Euro investments in chip foundries. Additionally, for this monolithic approach, compromises in terms of performance of individual functionalities must be made to make all processes compatible with fabrication on a single wafer.

A second approach aims at combining discrete photonic components such as lasers, modulators and detectors into a hybrid photonic system. Again, all components are fabricated on wafer level, however, each component is realized on a material platform, optimized for the respective functionality. This approach exploits complementary strengths of different material platforms, thereby offering superior performance and design flexibility compared to the monolithic approach. Another advantage is that all components can be individually tested and selected before integration into a complex system.

However, the assembly of such systems consisting of discrete components still represents a major challenge. For efficient coupling between photonic components, complex and expensive processes for high-precision alignment and careful adaptation of optical mode-profiles are needed.

Moreover, as wafer-level fabrication for both, the monolithic and hybrid approach, is inherently limited to planar structures, the functionalities to create photonic systems are severely limited. In particular, free-space emission is difficult to implement, as light emitted from planar waveguides is highly divergent. Therefore, many applications that require light emission into free-space, such as sensor systems, or free-space coupling among photonic components represents an unsolved challenge.

This work demonstrates how the advantages of the monolithic and the hybrid approach can be combined by *in situ* nano-printing of 3D functional photonic structures. These functional structures are directly printed to the facet of photonic components and allow adaptation of vastly dissimilar mode profiles while considerably relaxing alignment tolerances to the extent that scalable and cost-effective passive assembly techniques can be used. The presented approach is applicable to a wide variety of waveguide types, material platform and assembly concepts. Additionally, *in situ* nano-printing of 3D functional photonic structures solves the challenge of free-space light emission, as 3D functional structures can collimate and manipulate light emitted from planar waveguides.

The concept of manipulating light with 3D nano-printed functional structures is not limited to the assembly of photonic integrated systems but can be used in many scientific and industrial fields. As an example, this work shows the applicability in astro-photonics for optical coupling of starlight into single-mode fibers (SMF). To this end, micro-lenses are 3D-printed on an SMF facet and serve as a coupling device to an integrated wave front sensor of a terrestrial telescopes. By the help of this integrated wave front sensor, the correction of optical turbulence can be improved.

Based on these developments, this work extends the possibilities of 3D nano-printing to the degree that the fabricated structures can have themselves a functionality beyond optical coupling. To demonstrate this concept, optical engines with integrated optical actuation and read-out are printed onto SMF arrays and are tested for the use in relevant applications like scanning probe microscopy (SPM). The presented structures show the ability to detect atomic steps and measure the optical near-field of photonic structures and devices.

Parts of this work were published in the international journals *Nature Photonics*, *Small* and *Optics Express*.

Chapter 1 provides a general introduction to optical system assembly, SPM, and wave front sensing in astro-photonics.

Chapter 2 explains the fabrication strategy, including two-photon polymerization principles, suitable photoresists, and resolution constraints.

Chapter 3 provides background information on selected application fields that are addressed by the functional structures explored in this work.

Chapter 4 demonstrates how *in situ* microfabrication of freeform lenses and mirrors can simplify and improve any optical system assembly. Low coupling losses and high alignment-tolerances are demonstrated. Moreover, a novel concept to reduce reflection losses is shown.

Chapter 5 demonstrates how wave front sensing for single-mode coupling in astro-photonics can benefit from *in situ* micro fabrication of freeform lens arrays. A new, highly integrated device concept to sense deformations of wave fronts is implemented.

Chapter 6 demonstrates how 3D-printing is exploited to fabricate complex micro-optomechanical systems on the facet of fiber arrays. To this end, a complete dynamic mode scanning-near-field microscope (SNOM) is printed onto a fiber facet. The capability of these 3D-printed optical engines is demonstrated by performing scanning probe microscopy (SPM) with the ability to resolve atom-sized steps, to measure in a liquid environment, and to detect optical near-fields.

Chapter 7 summarizes this work and provides an outlook on further improvements of two-photon polymerization, and on new applications.

Kurzfassung

Integrierte photonische Systeme sind Grundlage für eine Vielzahl hochrelevanter Anwendungen, welche sich von optischer Kommunikation über Metrologie bis hin zu Astronomie erstrecken. Zudem spielen sie eine wichtige Rolle bei der Entwicklung von neuartigen Technologien wie Quantencomputern und Licht-Radar (Light Distance and Ranging, LIDAR).

Integrierte photonische Systeme verwenden optische Wellenleiter, welche Licht erzeugen, führen und detektieren. Es gibt zwei wichtige Ansätze, solch integrierte photonischen Systeme zu realisieren. Zum einen wird versucht, alle Funktionalitäten monolithisch durch Prozesse auf Waferebene umzusetzen, ähnlich der Herstellung von elektronischen integrierten Schaltkreisen. Dieser Ansatz erlaubt hochgradig skalierbare und kostengünstige Massenfertigung. Um alle Funktionalitäten auf Wafer-Ebene umzusetzen, sind jedoch Investitionen in Höhe mehrerer Milliarden Euro notwendig. Zudem müssen bei einem monolithischen Ansatz aus Kompatibilitätsgründen Kompromisse in Bezug auf die Leistungsfähigkeit der einzelnen Funktionalitäten gemacht werden, um die Herstellung auf einem Wafer zu ermöglichen.

Ein weiterer Ansatz zielt auf die Kombination diskreter Komponenten, wie Laser, Modulatoren und Detektoren ab. Auch hier können die einzelnen Komponenten auf Wafer-Ebene hergestellt werden, jedoch auf einer für die jeweilige Funktionalität besonders geeigneten Materialplattform. Dieser hybride Ansatz für die photonische Integration nutzt die komplementären Vorteile verschiedener Materialplattformen und ermöglicht so eine überlegene Leistungsfähigkeit und Flexibilität im Vergleich zu einem monolithischen Ansatz. Ein weiterer Vorteil ist, dass alle Komponenten individuell getestet und selektiert werden können, bevor sie in ein komplexes System integriert werden.

Allerdings stellt die Verbindungs- und Aufbautechnik solcher aus Einzelkomponenten bestehenden Systeme eine große Herausforderung dar. Für effizientes optisches Koppeln zwischen den einzelnen Komponenten sind komplexe und kostspielige Prozesse für die hochpräzise Ausrichtung sowie die Anpassung der optischen Modenprofile notwendig.

Da die Herstellung auf Wafer-Ebene inhärent auf planare Strukturen limitiert ist, sind auch die Funktionalitäten der mit beiden Ansätzen hergestellten photonischen Systeme begrenzt. Insbesondere ist eine Freiraumabstrahlung schwierig umzusetzen, da Licht, emittiert aus planaren Wellenleitern, sehr divergent ist. Somit stellen Anwendungen, welche Freistrahlemission vorausetzen, eine nicht gelöste Herausforderung dar.

Diese Arbeit demonstriert, wie die Vorteile beider Ansätze durch In-situ-Nanodruck von funktionalen, dreidimensionalen (3D) photonischen Strukturen kombiniert werden können. Die funktionalen Strukturen werden hierbei direkt an die Facetten der optischen Komponenten gedruckt und erlauben eine Anpassung von unterschiedlichen Modenfeldern sowie eine Strahlaufweitung. Dadurch werden die Genauigkeitsanforderungen an den Ausrichtungsprozess der photonischen Komponenten derart herabgesetzt dass kosteneffiziente, durchsatzstarke Assemblierungstechnik verwendet werden kann. Zusätzlich lösen die 3D-gedruckten funktionalen Strukturen das Problem der Freistrahlemission planarer Wellenleiter, da sie Licht kollimieren und manipulieren können. Der Ansatz ist somit auf eine große Vielfalt von optischen Komponenten und Assemblierungskonzepten anwendbar.

Das Konzept, Licht mit 3D-gedruckten, funktionalen Strukturen zu beeinflussen, ist nicht auf Anwendungen in der Verbindungs- und Aufbautechnik limitiert, sondern kann in vielen wissenschaftlichen und industriellen Feldern genutzt werden. Als Beispiel demonstriert diese Arbeit die Anwendbarkeit in der Astronomie, indem das Einkoppeln von Sternenlicht in einmodige Fasern (single-mode fiber, SMF) gezeigt wird. Hierfür werden Mikrolinsen auf die Facette einer optischen Faser gedruckt und dienen so als Kopplungselement zu einem integrierten Wellenfrontsensor für terrestrische Teleskope. Durch diesen integrierten Wellenfrontsensor ist eine Korrektur von optischen Turbulenzen möglich.

Basierend auf der Technologieentwicklung für optische Kopplung erweitert diese Arbeit die Möglichkeiten von 3D-Druck. Es wird gezeigt, dass 3D-gedruckte Strukturen selbst eine Funktionalität aufweisen können, welche über die Vereinfachung einer optischen Kopplung hinaus geht. Hierzu werden optische Systeme mit integrierter optischer Aktuator- und Ausleseeinrichtung auf

photonische Komponenten gedruckt. Die Einsatzmöglichkeiten der 3D-gedruckten Sensorsysteme werden durch die Anwendung als Rastersondenmikroskop gezeigt. Die Strukturen zeigen die die Fähigkeit, Stufen mit atomaren Abmessungen aufzulösen und das optische Nahfeld von optischen Komponenten zu detektieren.

Teile dieser Promotion wurden in den internationalen Fachzeitschriften *Nature Photonics*, *Small*, *Applied Physics Letters* und *Optics Express* publiziert.

Achievements of the Present Work

This work explores 3D-printed functional micro-optical structures that are directly attached to the facets of optical devices such as lasers, photonic integrated circuits, and optical fibers. This work comprises the underlying device concepts, models, and designs, the associated fabrication techniques, as well as the characterization and the functional demonstration of the resulting structures in the fields of optical system assembly, astro-photonics, and scanning-probe microscopy.

In the following, an overview of the achievements of this work is given:

First demonstration of 3D freeform-optical elements printed to device facets showing highly efficient and position-tolerant coupling: This work explores and demonstrates a toolbox of essential beam-shaping elements required to build hybrid optical assemblies: freeform lenses, freeform mirrors and multi-lens beam expanders that relaxes tolerances such that passive alignment can be used. The associated results were published in Nature Photonics [J3] and are described in more detail in Chapter 4.

First demonstration of 3D-printed micro-optics embedded in index matching material: For reducing the Fresnel reflection in multi-lens systems, this work introduces the concept of low index-contrast micro-optical systems (LIMOS). The viability of the approach is shown by coupling a pair of SMF via a pair of LIMOS beam expanders that comprise a total of 18 lens surfaces. The low-index contrast cladding reduced the loss below the minimum loss that can be theoretically achieved by lenses operated in air. The associated results were published in Nature Photonics [J3] and are described in more detail in Chapter 4.

First demonstration of 3D-printed micro-optical elements in astro-photonics: Demonstration of a highly compact and highly efficient wavefront sensor realized by 3D-printing a micro-lens array onto a multi-core fiber facet. The associated results were published in Optics Express [J4] and are described in more detail in Chapter 5.

First demonstration of a 3D-printed microsystem with both mechanical actuation and optical sensing functionalities: The system consists of a cantilever and a tip suitable for atomic force microscopes (AFMs) and for scanning near-field optical microscopes (SNOMs). Optical heating actuates the cantilever while a Fabry-Perot cavity is used for position read-out. This work demonstrates a resolution capable of resolving atomic layers, *in situ* measurement in air and an aqueous environment without realignment, SNOM measurements, and a high degree of fabrication reproducibility. The associated results were published in Small [J2][J3] and are described in more detail in Chapter 6.

1 Introduction

Optical systems consist to an increasing degree on functional single-mode waveguides. This approach allows miniaturization by integrating many functionalities on photonic integrated circuits (PICs). Such PICs rely mainly on optical waveguides that control optically coherent light. In particular, waveguides can generate, amplify and detect light.

An industrially highly relevant example for the use of PICs are transceivers for optical communication [1]–[3]. A transceiver typically contains several lasers with different wavelengths. Each laser's light is modulated and then multiplexed into one waveguide coupled to a single-mode fiber (SMF). The other end of the SMF is coupled to a receiver, featuring a demultiplexer and detectors.

Technological challenges make the combination of many functionalities on one PIC complex and expensive [4]. Therefore, many technical implementations rely on discrete photonic components such as lasers and PICs for modulation, multiplexing, and light amplification. The fabrication of these PICs can rely on planar optical waveguides that are lithographically defined on wafers using well-established manufacturing processes, similar to the processes known from electronic integrated circuits (ICs). Just as ICs, PICs are well suited for low-cost mass manufacturing.

However, the individual components have to be optically coupled to each other. A key problem connecting waveguides of different chips are their inherently small waveguide dimensions resulting in small and often vastly different mode-field sizes, requiring complex and expensive processes for high-precision alignment and careful adaptation of optical mode profiles. Such accurate alignment processes result in slow and expensive manufacturing. Therefore, photonic system assembly accounts for the majority of the overall manufacturing costs [4] in existing implementations of transceivers. In many other applications, assembly cost prohibits the widespread use of integrated photonic systems.

Besides the challenge of optically coupling light from waveguides of different PICs, also emission of light from a waveguide into free-space results in

technological problems. Due to the small mode-field diameters, the light leaving a waveguide is highly divergent. Collimation with discrete micro lenses is difficult due to optical aberration of spherical micro-lenses and the requirement of sub-micrometer precise lens placements. Therefore, many applications that require light emission into free-space from PICs such as sensor systems, integration of optical free-space isolators or free-space coupling to other PICs, e.g., for the sake of thermal isolation, represent a major challenge.

This work explores a new approach to assemble and build photonic systems. Functional photonic structures such as beam-shapers for coupling between PICs [J3] and for light collection from free space [J4] as well as opto-mechanical sensor systems [J2] are 3D microprinted onto photonic components using two-photon polymerization.

To this end, an immersion objective lens of a two-photon lithography system is brought in close proximity to the photonic component. The space between the objective lens and a photonic component is filled with a light-curable resist. Prior to 3D-printing, photonic chips are localized with sub-100-nm precision using different methods integrated in the lithography system. Due to this precise localization method, the alignment of a 3D-printed beam shaper to photonic chips is nearly perfect, and the alignment challenges of discrete micro-lenses do not occur. The beam shapers are subsequently 3D-printed by scanning a femtosecond laser causing two-photon polymerization that locally cures the resist. The remaining liquid resist is then developed using chemical solvents, leaving only the 3D-printed functional structures.

While discrete micro-lenses are in many practical cases limited to spherical lenses that always cause aberration, and often couple inefficiently, 3D-printed lenses couple light more efficiently as they can have any programmable, aspherical shape. Furthermore, as is the case with discrete micro-lenses, 3D-printed lenses allow expanding optical beams and adjusting the required alignment tolerance requirements. The fabrication of beam shaping elements can take place on a die-, array- or wafer-level, which is helpful for large-scale fabrication.

This work demonstrates the fabrication of beam-shaping elements [J3] with coupling losses approaching the theoretical optimum dictated by Fresnel

reflection. It is shown that in terms of alignment accuracy, the fabrication of beam shapers attached to the component with the smallest mode field diameter is preferred. Moreover, a relaxation of the required transverse alignment accuracy is demonstrated. The relaxed alignment accuracies allow to assemble photonic components using automated high-throughput assembly technologies [5], [6].

This work moreover uses 3D-printed micro-lenses for wavefront sensing in astro-photonics. Within the scope of this work, a microscopic, highly efficient wave front sensor is realized by equipping a multi-core fiber (MCF) with facet-attached 3D-printed lenses [J4]. In case of an optical turbulence, the 3D-printed lenses guide light to a detector array and thereby generate an error signal. The error signal can be fed to an adaptive optical element. This enables an improved compensation of optical turbulence

Based on the development of lenses for photonic system assembly and application in astro-photonics, this work demonstrates that 3D-printed elements themselves can have a functionality beyond facilitating optical coupling. To this end, optical engines with integrated optical actuation and read-out are printed onto fibers that serve as a scanning probe microscope (SPM) [J2]. The optical engines consist of a cantilever that can be actuated and excited resonantly by optically induced heating. A Fabry-Perot cavity reads out the position.

To demonstrate the viability of the concept, a series of experiments demonstrate atomic force microscopy (AFM) with atomic step resolution, AFM operation in liquid as well as optical measurements with sub-wavelength resolution using a scanning near-field optical microscope (SNOM). The technique is amenable to wafer-scale mass fabrication of SPM arrays and may unlock a wide range of novel application fields that are inaccessible to current SPM concepts.

Based on technology developed in this work, novel application are currently explored that range from various coupling demonstrations [7][8][J6], including experiments at cryogenic temperatures for quantum applications [9], 3D-printed optics for LIDAR [10] and novel application for SPM [11] and wafer-level testing [12] as well as application in astro-photonics [13][14] that may lead to the discovery of more exoplanets.

2 3D Laser Lithography

2.1 Two-Photon Polymerization

Direct-write lithography based on two-photon polymerization, features resolution in the sub-micrometer range. It is suitable to fabricate 3D-structures with a typical dimension of 500 µm and more, limited by the write field of the lithography tool. For two-photon polymerization, a femtosecond (fs) laser with a wavelength of 500 ... 800 nm is focused into a photo-curable polymer resist by a high numerical aperture (NA) objective lens, typically in the range of 0.5 to 1.4. Due to the high intensity in the focus region, see Figure 2.1(b), the simultaneous absorption of two (or more) photons is likely, see Figure 2.1(c). For processes, relying on m simultaneously absorbed photons, the probability is proportional to the m^{th} power of the intensity I. For two-photon absorption, multiplying the square of intensity with the total exposure time τ_{exp} provides a two-photon dose, which in the following is simply referred to as "dose,"

$$D = \text{const} \times I_{\text{Laser}}^2 \tau_{\text{exp}}.$$

Two-photon absorption allows triggering chemical reactions with activation energies corresponding to photon energies in the UV range, leading, e.g., to a change in the photoresist's solubility. In most cases, acrylic resist is used. Acrylic resists typically solidify by radical formation triggered by photoinitiators in a small region around the focus, within which the intensity is high enough for two-photon absorption to become likely.

These radicals generally diffuse a certain distance, before either reacting with monomers causing polymerization or being deactivated by a substance such as oxygen or another radical. This deactivation process is often referred to as "quenching". The volume element in which polymerization occurs is called "voxel" in analogy to a "pixel", corresponding to the smallest feature that the respective 3D-printer can create for a given resist, see Figure 2.1(a) for an exemplary illustration, adapted to the main use case targeted by this work.

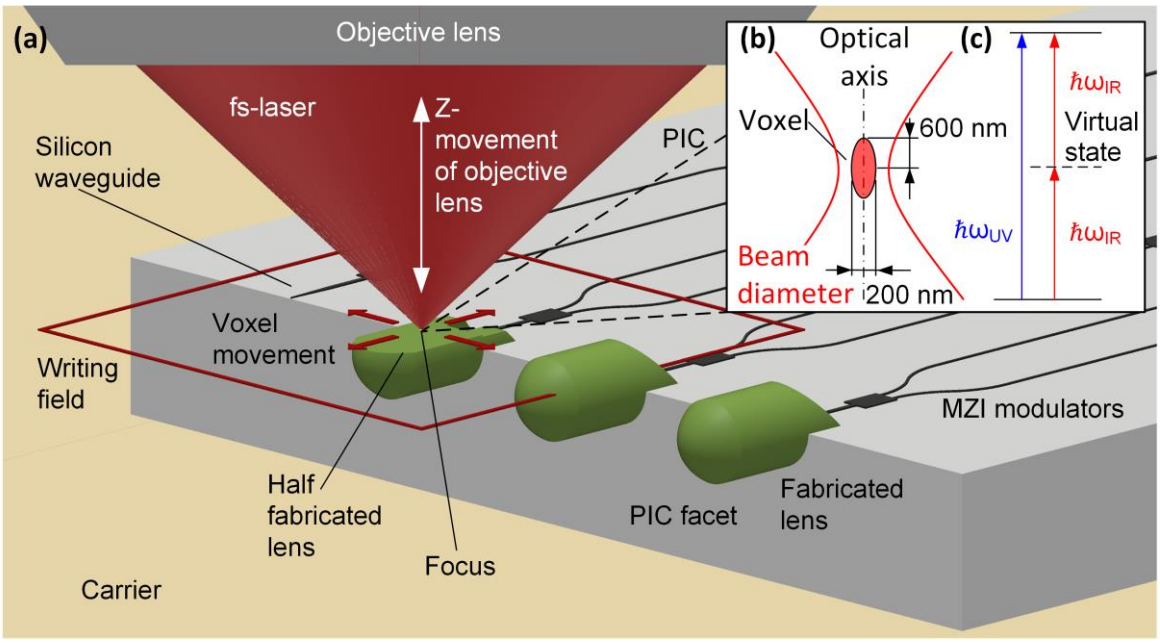

Figure 2.1: Exemplary illustration of 3D-printing based on two-photon polymerization **(a)** Schematic of the fabrication process of facet-attached 3D-printed micro-lenses. A photonic integrated circuit (PIC) with Mach-Zehnder interferometer (MZI) modulators is fixed on a carrier (brown). A liquid photoresist, not shown here, see Figure 2.2, fills the space between the objective lens and the PIC. The end section of a waveguide (e.g. a silicon waveguide) is localized using automated machine vision, and lenses are fabricated in a layer-by-layer process. Within one layer, the focus of a femtosecond (fs) laser is scanned (red arrows) within a writing field (red rectangle). By changing the distance of the objective lens with respect to the PIC, different layers can be fabricated. The printing process results in a 3D-printed, facet-attached micro lens that allows to focus or collimate light emitted by the waveguide. The working distance is typically in the range of 200 ... 300 µm. As a consequence, features of the optical assembly must not protrude more than 200 µm beyond the top surface of the PIC. **(b)** Cross-section through the focus of the fs laser beam. The beam profile is indicated by a red line and the optical axis by a black dash-dotted line. The elliptical voxel indicates the region where polymerization occurs; typical dimensions are indicated. **(c)** Energy diagram of two-photon polymerization. Instead of the absorption of one ultraviolet (UV) photon with energy $\hbar\omega_{UV}$ as in UV lithography, two infrared photons (IR) are absorbed simultaneously. The photon energies $\hbar\omega_{IR}$ add up via a virtual state.

Scanning the focus along a pre-programmed trajectory defines the desired structure by concatenating a multitude of voxels. The laser scanning is usually done layer-by-layer, see Figure 2.2, where each layer is in the focal plane of the objective lens. For each layer, rotatable galvanometer mirrors within the beam path of the 3D-printer move the focus along a pre-programmed trajectory, often in the form of serpentine hatching lines. This approach allows fast scanning of

the focal point within one focal plane of the objective lens, and only requires to physically change the sample-to-objective lens distance for stepping to the next layers. The layer-to-layer distance d_l as well as the distance d_s of two neighboring focus trajectory lines is typically in the range of 50 … 100 nm for optically smooth surfaces, while d_l is in the range of 400 … 1000 nm and d_s in the range of 100 ... 400 nm for coarser structures. After exposure, the unexposed resist is dissolved in a development step.

Depending on wavelength, initiator and intensity used, also multi-photon processes are involved [15] in the fabrication process. However, these multi-photon processes do not necessarily imply that three photons are absorbed simultaneously. For common photoinitiators, the initial initiator excitation is assumed to be a two-photon process, while a third photon is required to create a radical [16].

For the generation of pulses with sufficient intensity for two-photon polymerization, a fs laser is generally required. Historically, two-photon processes were excited by titanium-sapphire lasers at a wavelength of 800 nm. As these lasers tend to be expensive and difficult to maintain, fiber lasers are today more common. Fiber lasers for two-photon polymerization are typically implemented by mode-locked lasers for generation of short pulses combined with erbium-doped fiber amplifiers (EDFA) operated at a wavelength 1550 nm. By frequency doubling, a wavelength of 780 nm is generated with 100-fs-pulses at the laser exit [17], [18] and a repetition rate in the range of typically 80 … 100 MHz. The pulses may be subject to broadening to some extent when passing the optics of the lithography system due to chromatic dispersion of refractive elements. The chromatic dispersion can be made undone by pulse compression. Alternatively to fs-pulses, pulses in the picosecond (ps) range have been used [19]; this requires, however, higher pulse energies [20] and may result in inferior fabrication performance.

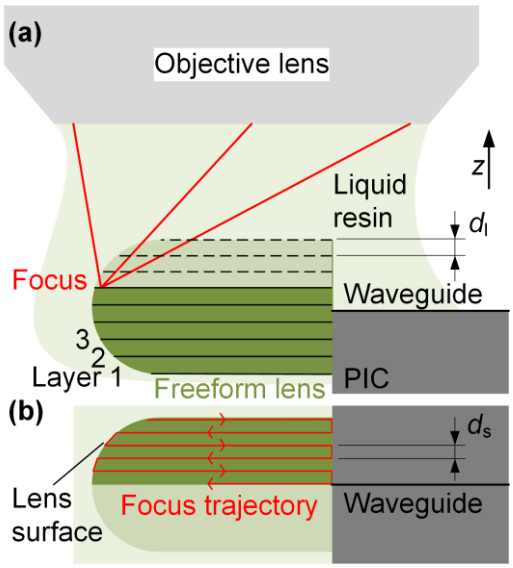

Figure 2.2: Schematic of a side view **(a)** and top view **(b)** of the fabrication process for a micro-lens that is in contact with a photonic integrated circuit (PIC). Both objective lens and PIC are in contact with liquid photoresist. The fabrication starts at Layer 1, and the various layers are then adressed by changing the distance from the objective lens to the PIC with layer spacings d_l. Fabricated parts of the structures are indicated in dark green and marked with solid lines, wheras light green and dashed lines refer to regions and layers are still to be exposed. Within one layer, the focus is scanned along a trajectory indicated by a red line in the top view schematic; the line spacing is d_s. Note that the sketch is not to scale - the objective lens in relation to the chip is typically 100 larger in horizontal direction than shown.

For 3D-printing, it is crucial to switch the laser light dynamically on and off. The pulse train of a femtosecond laser is additionally intensity modulated by an external modulator such as an acousto-optic modulator (AOM) or a Pockels cell. At a scanning speed of 10 mm/s, a modulation bandwidth of 100 kHz translates into a spatial discretization of 100 nm. This discretization is sufficient for most structures. A bandwidth of 100 kHz can be achieved by commercially available AOMs. Also modulation speeds in the 10-MHz-range and beyond can be achieved, sufficient for scanning speeds [21] of 1 m/s. Within this work, fabrication speed was mainly limited by the digital and analog bandwidth of the laser scanning mechanism.

The ultimate fabrication speed assuming perfect control over the voxel movement strongly depends on the available laser power. The average power of fiber based fs-lasers is typically in the 100…250 mW range; special lasers emit up to several watts, however, they are not suitable for long-term operation over months and years, which is required for both reproducible experiments and industrial applications. The power is up to a factor of 5 lower in the objective plane due to beam clipping at apertures in the 3D-printer, reflection loss, or limited efficiencies of optical components such as the AOM, temporal and spatial beam compressor or the objective lens.

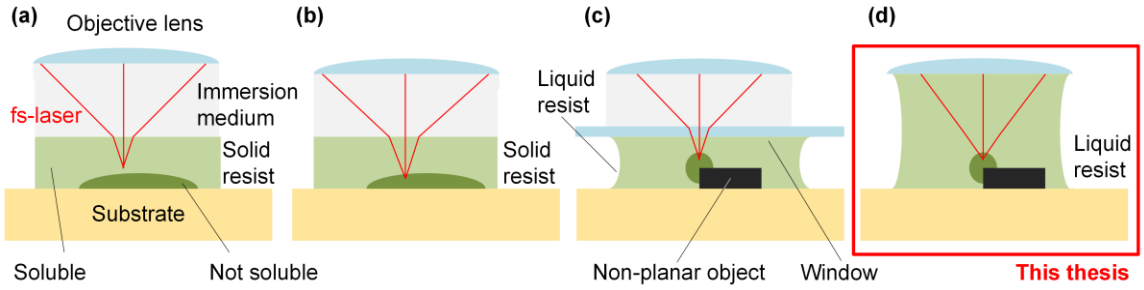

Figure 2.3: Different photoresist types on an opaque substrate exposed to fs laser radiation (red). Portions soluble in a subsequent development step are depicted in light green, insoluble portions depicted in dark green. In most cases, the free space between photoresist and objective lens is filled with an immersion medium, which allows the use of immersion objective lenses. (**a**) Solid, positive-tone photoresist. Here, the photoresist portion to be removed by development is irradiated. (**b**) Solid, negative-tone photoresist. The photoresist portion to remain after development is irradiated (**c**) Liquid, negative-tone photoresist separated from the objective lens with a cover slide and an immersion medium. **(d)** Liquid negative-tone photoresist. Here, the objective lens's front lens is brought into direct contact with the photoresist, which simplifies sample preparation.

2.2 Resist for Two-Photon Polymerization

Three-dimensional (3D) printing with light irradiation relies on changing a photoresist's solubility with respect to a certain solvent. In general, the change of solubility is triggered by the photon absorption of an initiator substance that subsequently triggers a chemical reaction. The photon-energy required to activate photoinitiator is typically equivalent to photons in the ultra-violet (UV) range. The required photon energy may come from a single UV-photon, or by a simultaneous absorption of two or more photons.

There are several configurations and photoresists suitable to fabricate 3D structures with two-photon polymerization, see Figure 2.3. Generally, there are positive-tone photoresists and negative-tone resists. For a positive-tone resist, Figure 2.3(a), the photoresist portion to be removed in development is irradiated. For a negative-tone photoresist Figure 2.3(b), the photoresist portion to remain after development is irradiated. While negative-tone photoresist may be liquid, Figure 2.3(c) and Figure 2.3(d), positive-tone resist is always solid, Figure 2.3(a). Solid resist layers can be deposited by spin-coating of a solution containing the resist material. To this end, a solvent-based resist is drop cast onto a

Table 1: Comparison of typical properties of the most relevant negative tone resists used for two-photon polymerization. Commercially available acrylate-based resists tend to exhibit lower performance in terms of shrinkage upon development and polymerization compared to epoxy-based resists and Zr-based resists. However, as acrylate-based resists are liquid, they are simple to process and are thus widely used.

Resist type	**Epoxy**	**Acrylate**	**Hybrid resist**
Typical example	SU-8	IP-Dip	SZ2080
Shrinkage upon polymerization	Low	High	Medium
Shrinkage upon development	Low	Low, to medium	Low
State prepared for fabrication	Solid	Liquid	Gel
Preparation method	Spin coating	Drop casting	Sol-gel process
Post-treatment	Heat	No	No

rotating wafer. While the wafer rotates, the solvent evaporates in a well-controlled manner and leaves a film with homogeneous thickness.

In this work, structures are always printed onto photonic elements like a single-mode fiber (SMF) or an optical chip. Resist preparation that relies on spin coating is not suitable for such non-planar objects. The non-planar objects would cause the photoresist layer to buckle or detach during spin coating. Also, solid resists that are prepared by drop-casting followed by a curing step are not suitable, as they do not form an optically smooth surface towards the objective lens. Also exposure through the substrate is not applicable in this work, as the substrate is usually opaque. Therefore, only liquid negative-tone photoresist is considered. Due to the simple sample preparation, the configuration in Figure 2.3(d) is used throughout this work.

Here, the objective lens is in direct contact with the photoresist that also serves as an immersion medium. Consequently, the resist affects the focusing properties of the lithography objective lens and must have a well-defined refractive index in the liquid state to avoid optical aberration. Additionally, it must be ensured that the resist stays in physical contact with both the objective lens and the sample.

A liquid negative-tone resist consists of a liquid blend of molecules that are in the following referred to as monomers. Each monomer carries reactive groups that allows linking different monomer molecules. A photosensitive initiator initiates polymerization of monomers, which thereby become less mobile and

form a solid material. The reactive groups used in photopolymerization are usually either epoxies or (meth)acrylates, see Table 1 for an overview.

One of the first resist systems used for two-photon polymerization has been epoxy-based SU-8 [22]. Epoxies are solid negative resins and polymerize by a ring-opening process initiated by irradiating a photoacid generator (PAG) which subsequently creates a photoacid. The polymerization reaction takes several seconds up to minutes after irradiation, and often requires a post-bake process.

Epoxies have very advantageous properties in terms of shrinkage upon polymerization, as the ring-opening polymerization only induces minor distance changes of polymerized molecules compared to the distance of liquid monomer molecules. To achieve optically smooth surfaces, epoxy type SU-8 has to be spin-coated, which is not possible for many relevant processes such as fabrication on 3D-components.

Polymerizable epoxies are also available in liquid form. However, such photoresists are not common for two-photon polymerization and were so far not successfully used. The problem is most likely that in a liquid environment, the photoacid diffuses during exposure and polymerization, resulting in lower resolution or incomplete polymerization.

Acrylates are the most common material systems for two-photon polymerization. To polymerize an acrylate, see Figure 2.4(a), the photoinitiator creates a radical [23] and thereby triggers polymerization of monomers. The polymerization releases a new radical, in a “chain growth,” eventually resulting in a solidified resist portion. A single radical can cause the complete photoresist volume to polymerize in a single chain, at least in theory. However, chain growth is in practice terminated by other radicals, by oxygen, or by other inhibitors, or it stops due to steric hindrance.

As an example, the commonly used acrylate monomers, pentaerythritol triacrylate (PETA), is shown in Figure 2.4 (b). The three functional groups of PETA make a linear growth very unlikely, and instead result in random growth in different directions, or in cross-linking with other polymer chains. Thus, the resist becomes solid long before all acrylate groups have reacted, as the cross-linked molecules’ mobility is highly reduced, resulting in incomplete polymerization.

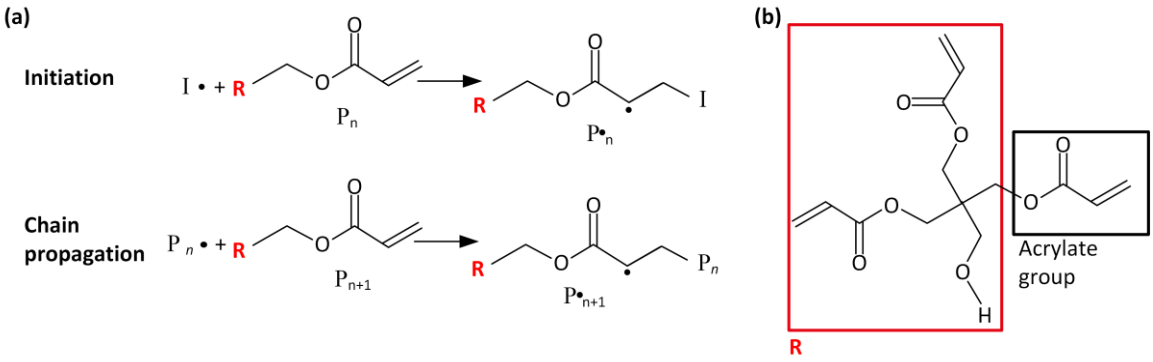

Figure 2.4: Schematic of the reaction of one acrylate group of pentaerythritol triacrylate (PETA). (**a**) Polymerization reaction. A primary radical I• initiates the chain growth by opening a C=C double bond in a monomer P_n, and thereby radicalizing the monomer, denoted by $P•_n$. In a subsequent and repetitive chain propagation, the monomers $P•_n$ polymerize with other polymers P_{n+1} by again opening a C=C bond and creating a radical. (**b**) Formula of PETA. The part labelled with a red frame R is indicated in (a). A black frame indicates the reacting functional acrylate group. Other groups may react subsequently and create a dense network.

The completeness of polymerization can be described by the degree of conversion C, which is defined as fraction of reacted compared to the total amount of reactive groups.

The degree of conversion is a crucial parameter for long-term stability of photoresist, as unreacted photoresist may either lead to volatile material or to post polymerization, in particular during exposure to heat. Both effects lead to shrinkage and thus deformation and mechanical stress. Development of photoresist suitable for this work should thus usually aim at high degree of conversions. As complete simulations of photoresists are not possible, the development of photoresist systems, to some degree, relies on empirically determining a suitable blend of various acrylates with different functionality, molecular weight, and structure to satisfy different photoresist requirements.

While materials for macroscopic 3D-printing can rely on decades of experience of the UV-curing industry, microscopic 3D-printing has to explore novel approaches. The problem arises from the fact that a resolution in the sub-micrometer range has very different requirements for the photoresist system compared to the fabrication of macroscopic structures with minimum feature sizes of 100 µm. For example, each radical will diffuse upon light activation, with a

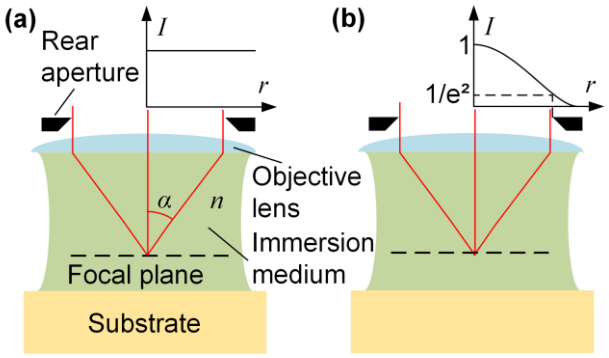

Figure 2.5: Illumination of the rear-aperture of an immersion objective lens with a collimated beam (red) and intensity *I*. The objective lens focuses the collimated beam with an angle α into an immersion medium with refractive index *n*. **(a)** Illumination with a beam having a flat-top intensity profile in radial direction *r*. An Airy disc intensity distribution at the focal plane is to be expected. **(b)** Realistic illumination with a Gaussian beam, for which the beam diameter at $1/e^2$-intensity level is matched to the diameter of the rear aperture.

typical range of up to several micrometers. While this is not relevant for 3D-printing with 100-µm-resolution, sub-micrometer resolution is heavily affected by diffusion. Photoresists for 3D-microprinting therefore have to show very different viscosity compared to photoresists for standard 3D-printing [24]. Therefore, existing commercial photoresists for macroscopic 3D-printing cannot be transferred to micro 3D-printing with two-photon polymerization.

Besides two-photon-polymerization-related challenges, acrylates also have inherent disadvantages associated with shrinkage during fabrication and development. The first type of shrinkage, during polymerization, is well known, e.g., from curing acrylic adhesives: When acrylate polymerizes, the loose van der Waals binding of monomer molecules changes to a covalent bond. The distance between monomers is strongly reduced, causing linear shrinkage of more than 5 %, i.e., more than 15 % in volume. As the shrinkage happens at a faster time scale than the fabrication of a complete structure, and in most cases also faster than the time scale of fabricating one layer, the shrinkage during polymerization is not always apparent in the final structure. However, it may cause inner tension of the structure that may lead to deformation during 3D-printing, in the development process, or during the lifetime of the 3D-printed device.

In addition to polymerization shrinkage, acrylates also tend to shrink during development, as part of the material has not reacted due to material impurities or incomplete monomer conversion. Both shrinkage processes, during polymerization and shrinkage during development, are very low when using a hybrid resist [25]. Here, a condensation reaction prior to 3D-printing induces a sol-gel

process, and the material is structured in a solid form rather than as a liquid. A radical photoinitiator then triggers formation of covalent meth(acrylate) bonds. As the fraction of these covalent bonds is much lower than in pure acrylic resist and the material is already solidified, no shrinkage can be observed. However, such hybrid resist requires solidification prior to 3D-printing, which is incompatible with the fabrication processes in this work. Therefore, either an adaptation of the fabrication process that allows to use solid resists or further research on standard acrylic materials is needed, see discussion Section 7.2 for details.

2.3 Resolution of Two-Photon Lithography

Optical resolution

The achievable resolution of the lithography process is determined by the photoresist and the intensity distribution in the focal region. The intensity distribution in the focal region is primarily dictated by the vacuum wavelength λ and the numerical aperture $\mathrm{NA} = n \sin \alpha$ of the objective lens. Here, n is the refractive index of an immersion medium within which the beam is focused, and α is the half opening angle, see Figure 2.5. The lithography wavelength used in this work is 780 nm, the refractive index n amounts to approximately 1.51 at 780 nm, and the numerical aperture is 1.4.

A flat-top illumination of the rear aperture of the objective lens, see Figure 2.5(a), would result in an Airy disc intensity distribution in the focal plane. In reality, however, the objective lens is illuminated with a Gaussian-like intensity distribution typically emitted by the fs-laser, see Figure 2.5(b). Here, it is common to adjust the beam diameter defined by the $1/e^2$-intensity levels of the laser beam to the size of the rear aperture of the objective lens. Therefore, an apodised Gaussian intensity distribution is a more appropriate scenario.

For a coarse approximation of the focus spot dimension transversal to the optical axis of the objective lens, one can calculate the waist radius w_0 at the $1/e^2$-intensity level in paraxial approximation for a given numerical aperture NA = 1.4 at a vacuum wavelength λ = 780 nm:

$$w_0 = \frac{\lambda}{\pi \mathrm{NA}} = 177\ \mathrm{nm}.$$

This corresponds to a full width of half maximum of

$$\mathrm{FWHM} = \sqrt{2 \ln 2}\ w_0 = 208\ \mathrm{nm}.$$

The focus dimension in axial direction can be described by the Rayleigh range z_R, where $2z_R$ corresponds to the full width at half maximum. The Rayleigh range z_R for a refractive index of approximately n = 1.51 of the immersion medium amounts to

$$z_R = \frac{n \pi {w_0}^2}{\lambda} = 191\ \mathrm{nm}.$$

This corresponds to a full width at half maximum of 382 nm.

However, due to the strong divergence of an objective lens with a numerical aperture of 1.4, a paraxial approximation and assuming a scalar electric field to calculate the focal intensity is not accurate. Therefore, wide-angle calculations of the resulting intensity distribution are required. Simulations of an objective lens at a wavelength also used in this work can be found in [26]. Also, calculations for different illuminations of the rear aperture in Figure 2.5 are provided in [26]. These calculations give a full width at half maximum of 322 nm transverse to the optical axis of the lithography system (546 nm full width at $1/e^2$ value) and 786 nm in axial direction (1336 nm full width at $1/e^2$ value). The scalar and paraxial calculation thus underestimates the focus dimension both in transverse and axial direction.

The axial focus dimension, *i.e.*, along the lithographical optical axis, scales with λ/NA^2, while the radial dimension scales with λ/NA in paraxial approximation. Therefore, a high numerical aperture is essential for a high resolution in the axial direction. As numerical apertures of one objective lens in excess of 1 can only be achieved by immersion objective lenses, immersion lithography is the preferred method for two-photon polymerization.

Threshold processes and resolution

The dimension of the focus alone cannot define the achievable resolution of the lithography system. Instead, the smallest achievable structure is defined by a combination of optical resolution and photoresist properties. Within this work, only negative-tone resist has been used. An ideal negative-tone photoresist either fully polymerizes or does not polymerize at all, see threshold dose D_t and blue curve Figure 2.6(a), where the degree of conversion C is plotted over the dose D. Such an ideal resist creates a voxel with homogeneous and complete polymerization and with $C = 1$ above D_t, see Figure 2.6(b), where the dose D is plotted over the transversal position x and the resulting voxel size is indicated. Assuming a perfectly intensity-stable laser, such an ideal resist would be suitable for the fabrication of arbitrarily small structures by adjusting the dose D in the center of the voxel to be just above the polymerization threshold D_t, see Figure 2.6(c).

However, realistic photoresists do not show an ideal binary transitional behavior, but a gradual change of the degree of conversion C upon increasing the dose, see Figure 2.6(a), red curve. At a dose D_1, the resist reaches a degree of conversion C_{min}, and can just withstand the subsequent development process. At a dose D_2, the photoresist reaches its maximum degree of conversion. Note that this maximum degree of conversion is still well below 100 % - a degree of conversion close to 100 % can in practice not be reached, due to a decreased mobility of acrylate molecules with increasing chain length. Typical values for C_{min} are around 0.5 while C_{max} is below 0.75 [27], both estimated from the degree of conversion of 3D-printed structures measured by vibrational spectroscopy.

The non-ideal threshold behavior of real photoresists is described by the slope $\gamma = \Delta C/\Delta D$ of the contrast function, see Figure 2.6(a). For a given change of the degree of conversion ΔC upon a dose increase ΔD, the contrast is defined as the slope $\gamma = \Delta C/\Delta D$. The resist's contrast function is an important factor that limits the achievable resolution: if the dose distribution of the voxel would be chosen such that it is everywhere below D_1, no material would sufficiently polymerize to withstand the developing process.

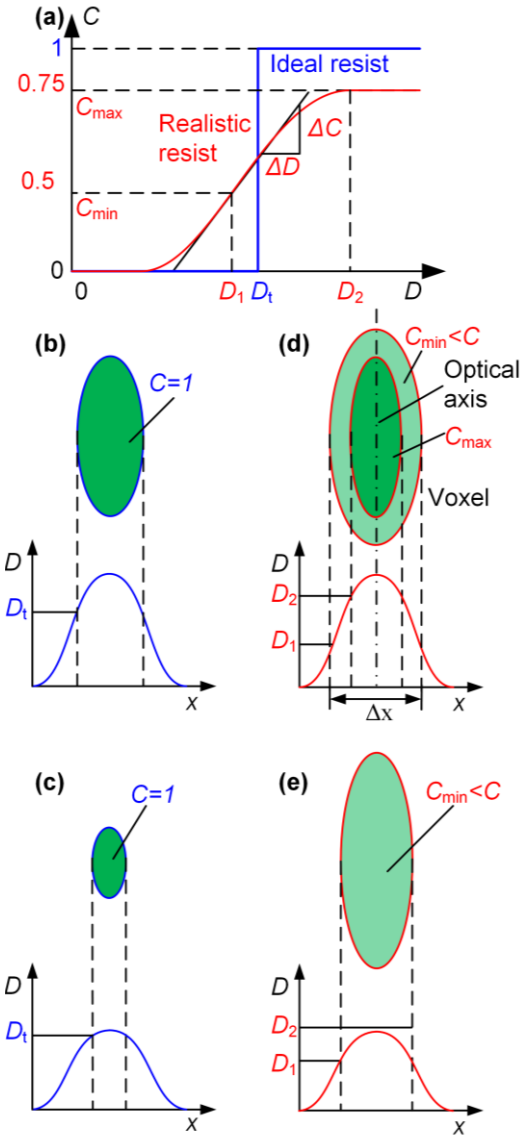

Figure 2.6: Schematic description of ideal (blue) and realistic photoresists (red). **(a)** Contrast curve of an ideal photoresist (blue) and a realistic photoresist (red). At a low irradiation dose, neither photoresist shows an increased degree of conversion C. At a threshold dose D_t, the ideal photoresist instantaneously fully polymerizes, see blue curve. The realistic photoresist shows a gradual increase of C with the dose D, characterized by the slope of the contrast function $\gamma = \Delta C / \Delta D$, and becomes insoluble at a lower threshold dose D_1. At a higher threshold dose D_2, the photoresist reaches the maximum degree of conversion C_{max}, which may still be $C = 1$. **(b)** A voxel produced in an ideal resist only shows a region of full polymerization $C = 1$. **(c)** Ideal resist at low dose. The ideal resist can have an arbitrarily small region with fully polymerized resist. **(d)** Cross-section of a voxel along the plane defined by the lithographical optical axis (dot-dashed line) and the transverse x-direction for a realistic resist. At a given dose-distribution, only the inside volume of the voxel reaches C_{max} while the outside region of the voxel only partially polymerizes, *i.e.*, $C_{min} < C < C_{max}$. **(d)** At a lower total dose, the realistic resist shows a region of partial polymerization. Such a structure withstands development, is however likely to exhibt shrinkage upon development and exposure to temperature. Therefore a higher dose, as indicated in (e) must be used.

Therefore, the dose must be chosen such that a substantial part of the voxel has a dose higher than D_2 associated with a degree of conversion C_{max}, see Figure 2.6(d). The dose required to achieve structures that are fully polymerized in the center dictates a certain voxel size Δx and thereby limits the resolution of the lithography process.

Voxel with doses below $D_{2\,a}$ lead to high resolution at low degree of conversion, Figure 2.6(e), light green. The low degree of conversion results in structures that are mechanically not stable and may shrink upon development or exposure to temperature.

Optical proximity effect

In the case of complete structures or closely spaced writing lines or features, optical proximity effects strongly limit the resolution [28], [29]. In general, proximity effects in lithography are a consequence of the fact that the polymerization at a certain point depends on the irradiation in its vicinity, which may lead to an unwanted accumulation of dose and hence to a polymerization reaction, see Figure 2.7. The total dose at a certain point is defined by summing the dose distribution of all focus positions in the vicinity of this point. As at points P_c, close to the corner of the programmed structure, there are fewer voxel positions contributing to P_c, there is a lower dose around the corners of the programmed structure than at points P_m close to the middle of the outline of the programmed structure. As a result, the structure is under exposed at the corners and the iso-dose line for the threshold dose D_t has a shape as shown in Figure 2.7. This is a purely optical effect that is also present for an ideal photoresist.

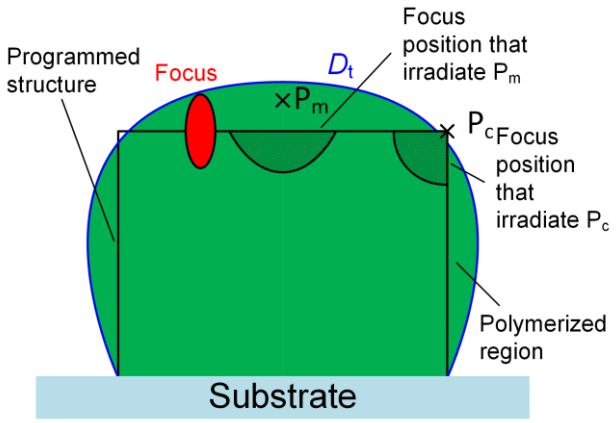

Figure 2.7: Schematic illustrating the optical proximity effect by showing a cross section of a block on a substrate. The total dose at a certain point is defined by summing up over the dose distribution of all focus positions in the vicinity of a point that irradiates the point. As at points P_c, close to the corner of the programmed structure, fewer voxel positions contribute to the total dose, there is a lower total dose around the corners of the programmed structure than at points P_m close to the middle of the outline of the programmed structure. As a result, the iso-dose line for the threshold dose D_t (see Figure 2.6) is closer to the corners, or even inside, of the programmed structure at the middle of the outline of the programmed structure. This is a purely optical effect that is also present for an ideal photoresist. Also temporal effects, e.g., the final lifetime of radicals was not considered so far.

The proximity effect is also one of the main reason why multi-photon polymerization is preferred over one-photon polymerization [30]. Figure 2.8 depicts for a one-photon process (blue) the intensity distribution and for two-photon processes (red and green) the squared intensity distribution along the optical axis close to the focal region. The function was calculated for an objective lens with NA=1.4 using a normalized Lorentz-function as a paraxial approximation to the actual intensity distribution along the optical axis. A vacuum wavelength of 780 nm and 520 nm was considered for two-photon processes; the squared intensity is shown in both cases. For comparison to a one-photon process, an intensity distribution for 405 nm is also depicted. The actual numerical values only give an order of magnitude estimate, as the Lorentzian approximation strongly overestimates the resolution.

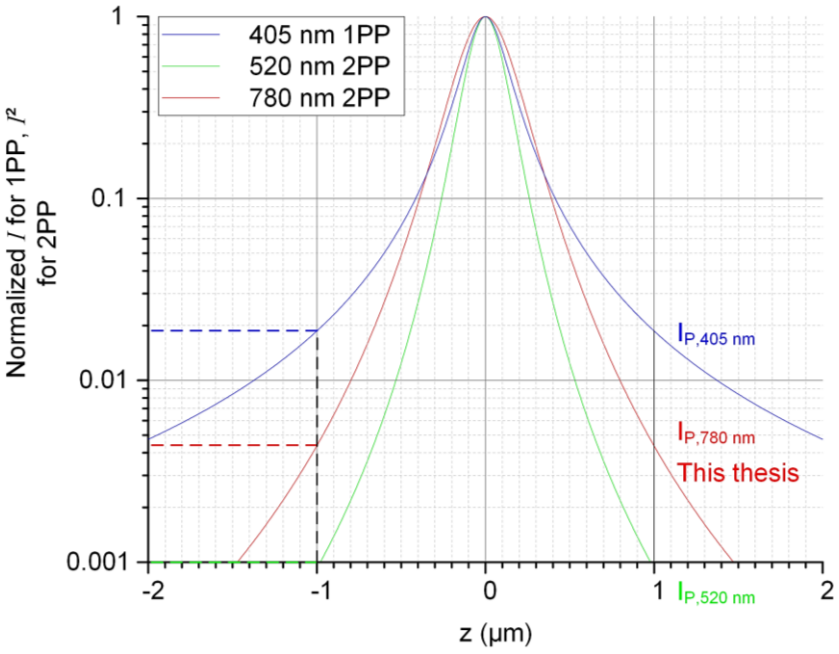

Figure 2.8: Normalized intensity (blue) and suqared intensity (green, red) in axial direction for one-photon processes (1PP) and light at a wavelength of 405 nm (blue) and for two-photon processes (2PP) at a wavelength of 520 nm (green) and 780 nm (red), shown on a logarithmic scale. For 1PP the intensity is shown, for 2PP the squared intensity.

For one-photon absorption, the proximity dose $D_{\mathrm{p,405\ nm}}$ at 1 µm distance from the focus is still at 2 % compared to the maximum intensity. When considering two-photon absorption at 780 nm and 520 nm, the dose $D_{\mathrm{p,780\ nm}}$ and $D_{\mathrm{p,520\ nm}}$ at 1 µm from the focus spot amounts to 0.4 % and 0.1 %, respectively. Calculating the optical dose accumulation by summing over the dose exposed in the vicinity of a certain point would therefore result in extreme proximity effects in the range of micrometers and more for one-photon polymerization, while the effect is significantly smaller for two- or multi-photon polymerization.

Advantages of multi-photon over one-photon polymerization

The optical proximity effect is one of the reasons, why multi-photon polymerization is preferred over one-photon polymerization. For one-photon lithography, the proximity effect would be even more pronounced [30], see Figure 2.8, resulting in an even higher dependence of the resulting structure from the focus trajectory. Therefore two-photon polymerization is advantageous compared to one-photon polymerization, as the optical proximity effect is strongly mitigated.

Letting aside the lower proximity effect, two-photon polymerization is still preferred due to the absence of a photoinitiator reaction of resist between the focus and the objective lens. For one-photon absorption, the photoinitiator outside the voxel region creates radicals that are, however, quenched before they trigger a

polymerization reaction. In two-photon polymerization, the photoinitiator does not react far outside the voxel region. Therefore, in both cases, no polymerization occurs outside the voxel region; however, in the case of one-photon polymerization, the initiator is consumed also outside the focal region. The consumption of photoinitiator in one-photon lithography makes process instabilities very likely. For example, the photoinitiator in the region between voxel and objective lens may have already degraded, while other areas still contain fresh photoinitiator material. Consequently, the polymerization of a certain structure will heavily depend on whether the resist material between structure and objective lens have been previously penetrated by light or not.

Moreover, by polymerizing resin with UV light, there is a considerable risk of polymerizing photoresist at the front surface of the objective lens, making a suitable protection mechanism [20] indispensable.

Suppose that structures are fabricated spaced at a relatively large distance, such that proximity effects are not relevant. In that case, two-photon polymerization does not have advantages over one-photon polymerization. On the contrary: The smaller wavelength of one-photon polymerization leads to a smaller diffraction limited focus than for light used for two-photon polymerization. This smaller optical focus can be also advantageous for lithography resolution. Indeed, there are publications [31], [32] using a lithography tool with a laser at 405 nm and 532 nm. The experimental results indicate higher resolution than with two-photon polymerization, at least for isolated features.

The role of radical lifetime

Experimental observations [33] indicate that depositing the same optical two-photon dose in a short time with high laser power will yield higher polymerization than depositing the same optical two-photon dose in a longer timeframe with lower laser power. The “fast” irradiation will cause a higher degree of conversion. This effect is analogues to the Schwarzschild effect in photography: Here a short illumination with high intensity provides a higher exposure of photographic films than a long illumination with lower intensity, provided that in both scenarios the total energy is identical.

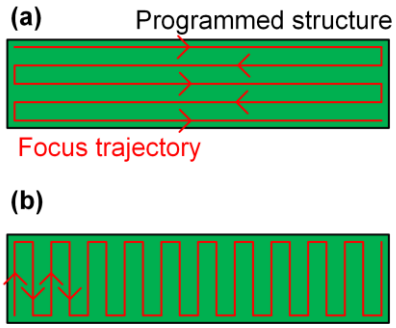

Figure 2.9: Effect of different focus scanning strategies on the polymerization of a structure. **(a)** The fast scanning axis is aligned along the long direction of the structure. **(b)** The fast scanning axis is aligned along the short direction of the structure. The situation in (b) may lead to quencher depletion and the radical liefetime is increased. Therefore polymerization in (b) can be higher than in (a).

The "Schwarzschild Effect" in two-photon lithography can be explained by quencher depletion [33], assuming that during a quenching reaction the quenching species is consumed. If the radical generation rate is high enough to significantly reduce the presence of the quenching species, such as oxygen, the radical lifetime is increased. A radical is thus more likely to trigger a polymerization reaction. Therefore, if a high two-photon dose is emitted within a short time, the degree of conversion may be higher than in a situation in which the same two-photon dose is emitted within a longer time.

The spacing of neighboring writing lines is typically well below the voxel size and thus writing lines significantly overlap. If a structure is fabricated with different focus trajectories, see Figure 2.9, the laser thus irradiates a certain point multiple times within a long, Figure 2.9(a), or a short, Figure 2.9(b) time interval. In the latter case, quencher depletion may significantly increase radical lifetime and make a polymerization reaction more likely than in case of Figure 2.9(a).

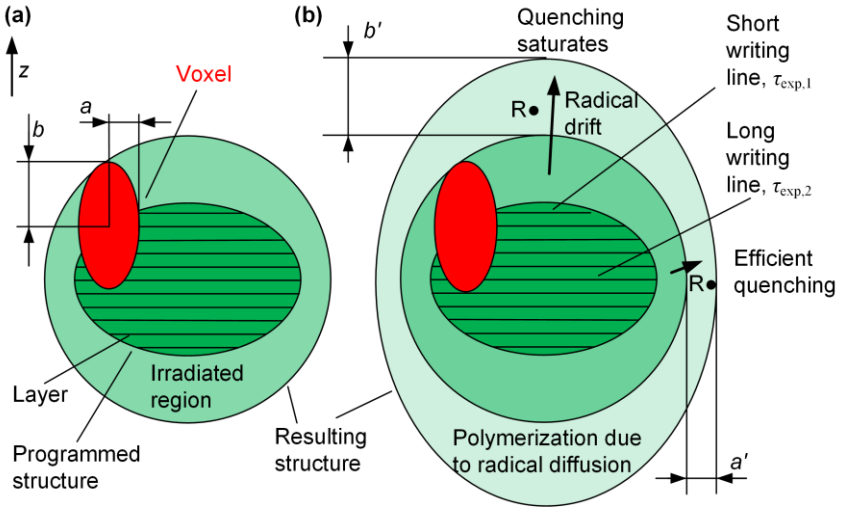

Figure 2.10: Effect of radical diffusion on resolution showing a cross-section of an elliptical structure to illustrate different types of shape deviation. **(a)** Ideal resist without radical diffusion and a infinitively small radical lifetime. The resulting structure is purely defined by the irradiated region. The deviation of the resulting structure from the programmed structure is defined by the shape of the voxel and amounts to an distance *b* along the *z*-direction and *a* transverse to the *z*-direction. **(b)** Realistic resist showing radical (R●) diffusion that expands the resulting structure from the irradiated region by a maximum distance *b'* in *z*-direction and *a'* transverse to the *z*-direction. Writing lines fabricated with different time intervals $\tau_{exp,1}$ and $\tau_{exp,2}$ results in different radical generation rates. High radical generation rates due to lines fabricated with $\tau_{exp,1}$ saturate quenching mechanisms and lead to longer radical diffusion. Therefore the deviation *b'* may be larger than *a'*.

Radical diffusion

So far, it was assumed that radicals remain stationary. In fact, diffusion of radical molecules plays a highly relevant role [24], [29]. If a radical diffuses during its lifetime, it may initiate a polymerization reaction at a different site than its generation site, which will lead to a further decrease in resolution. At the same time, quenchers, in particular oxygen, will reduce radical lifetime and thus limit the diffusion length. There is thus a dependence of the fabrication strategy on the radical diffusion.

If, for example, structures are fabricated that both contain relatively short and long writing lines, see Figure 2.10, the interval $\tau_{exp,1}$ and $\tau_{exp,2}$ between scanning subsequent writing lines varies. As the voxel is typically larger than the writing line distance, short lines fabricated with $\tau_{exp,1}$ will lead to higher radical concentrations, resulting in quencher depletion and higher diffusion length. Therefore, the resolution may be significantly lower at parts of structures with relatively short times $\tau_{exp,1}$, e.g., at the apex of a 3D-printed micro-lens. This may result in

a “hump” at the apex of a 3D-printed micro-lens, significantly reducing its performance.

Approaches to increase resolution

In most relevant applications, complex 3D-printed features are to be fabricated rather than isolated single features. Therefore, almost all research activities in 3D microprinting focus on two-photon absorption, despite the theoretically lower resolution compared to one-photon absorption for isolated features.

In particular, great effort was dedicated to increasing the resolution by concepts that are based on similar principles as stimulated emission depletion (STED) in high-resolution microscopy [34]. In the optical depletion scheme, a doughnut-shaped intensity distribution around the voxel de-excites the photoinitiator prior to creating radicals, and thereby restricts radical creation to the voxel center. This scheme is available for several photoinitiators [35], but requires a very complex optical setup and limits the choice of initiators.

Additional measures to increase the resolution addressed the resist viscosity for balancing radical and quencher diffusion. While at low viscosities, both quenchers and radicals can diffuse, at very high viscosities neither quenchers nor radicals are able to do so. However, at intermediate viscosities, quenchers, in particular oxygen, can still diffuse due to its smaller atom size, while radicals are largely immobilized. This regime is expected to show very low effective radical diffusion length and therefore appears to be advantageous for high-resolution multi-photon lithography [24].

An alternative approach to increase the resolution relies in quenchers that are intentionally added to the photoresist [36]–[38]. The quenchers limit the photoinitiator diffusion, and effectively reduce the voxel size. Compared to the optical depletion approach, chemical radical “depletion” was not investigated in comparable depth. The approach may provide a resist with a lower proximity effect, high resolution and simple applicability. Potentially, higher laser power is needed to counteract the increased quenching rates.

Besides the strategies for increasing the resolution during photopolymerization, there are also approaches that “shrink” structures after fabrication [39], [40], [41]. The problem with such strategies is in general that shrinkage may lead to

shape deviations and is highly problematic for the alignment accuracy with respect to photonic components. Therefore, shrinking structures after fabrication cannot be considered as a suitable approach to increase fabrication resolution for the structures investigated in this work.

3 Selected Application Fields of 3D-printen Micro-Optical Structures

This work applies fabrication approaches based on 3D-lithography in various technological fields ranging from optical system assembly, micro-optics for photonics in astro-photonics as well as scanning probe microscopy (SPM). This chapter provides background information on the respective technological fields including state-of-the-art approaches.

3.1 Material Platforms for Integrated Photonic Systems

Hybrid optical systems require the optical connection of different optical devices like lasers, modulators, or single-mode fibers (SMF). In the past decades, a wide range of assembly strategies has been developed for this task. A highly relevant example of such a photonic system is a laser combined with a modulator connected to an SMF. Such systems are currently used as an optical transmitter in large-scale data centers. Figure 3.1 depicts various approaches to realize such a transmitter. These include discrete combination of components and SMF, Figure 3.1(a), where macroscopic components are connected with SMF. Figure 3.1 (b) Shows monolithic integration of all functionalities on one material platform. Figure 3.1 (c) shows Heterogeneous integration of InP lasers on SOI wafers using plasma-assisted bonding. Figure 3.1 (d) to (f) show different hybrid integration schemes including hybrid integration using 3D-printed lenses as used in this work. The following chapters explains and motivates the various approaches and concludes with explaining this work's approach to optical system assembly.

The most common material platforms to implement photonic systems are silicon-on-insulator (SOI), silicon nitride (SiN) and indium phosphide (InP). Table 2 gives a rough comparison of the respective material platform's strengths and weaknesses. The values indicated in Table 2 are based on multi-project wafer (MPW) fabrication which combine several chip designs on a common reticle.

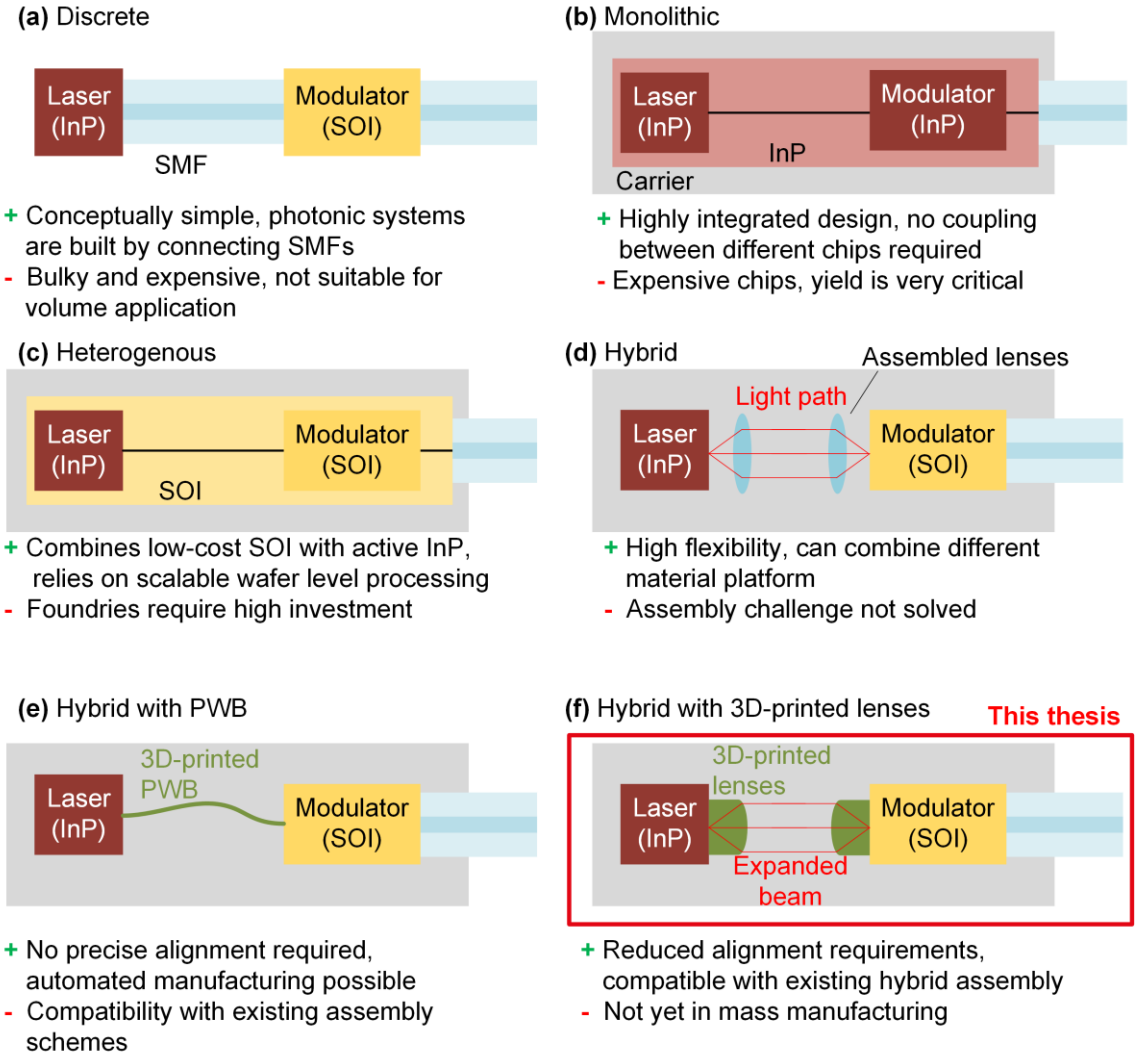

Figure 3.1: Different methods to build a photonic system consisting of an indium phosphide (InP) laser and a silicon-on-insulator (SOI) chip as well as a single-mode fiber (SMF) as a connection to the outside world. The most relevant advantages and challenges are listed below the respective figure. **(a)** Combination of discrete components with an SMF. **(b)** Monolithic integration of all functionalities on one material platform. **(c)** Heterogeneous integration of InP lasers on SOI wafers using plasma-assisted bonding. **(d)** Hybrid integration relying on assembled micro-lenses with, e.g., active alignment. **(e)** Hybrid integration using photonic wire bonds (PWB). PWBs are printed onto already fixed components. **(f)** Hybrid integration using 3D-printed lenses as used in this work. Lenses are directly printed on InP lasers and SOI modulators prior to assembly.

SOI is the most cost-attractive technology platform, as it can rely on technologies developed for silicon (Si) integrated circuits (ICs) for micro-electronics. Therefore, the SOI technology platform is very scalable [42]–[44] as it can benefit from past investments in the semiconductor industry. In particular, SOI chips can be processed on large 300 mm-wafers, which offers a clear cost advantage for volume fabrication. Also, at low volume, SOI is relatively low in cost due to the possibility of routing waveguides with small bending radii that allows in many design scenarios smaller photonic chips, see Table 2. As the cost for photonic chips scales with the surface area of the chips, smaller chips are less expensive. Moreover, the high number of foundries offering SOI fabrication and MPW runs makes the technology easy to access.

The SOI chips as used for silicon photonics consist of a thin, typically 220-nm-thick Si layer, which is bonded onto a buried oxide layer of 2 … 3 µm thickness The buried oxide layer lies on a typically 700 µm thick Si-wafer which acts as a mechanical support. The Si layer is structured to form 400-500 nm wide waveguides that transmit light with a typical wavelength of about 1.2 to 1.6 µm. In a last step, a top oxide with 2 … 3 µm thickness is deposited on the structured Si-waveguides.

Many functionalities, such as modulators and detectors [45], [46], are available on the SOI platform. Detectors, e.g., are implemented as Ge-diodes. To modulate light, a refractive index change upon applying a modulating voltage is required. Si has no sufficiently high electro-optical coefficient. Applying an electric field to an Si waveguide would thus not yield sufficient change of refractive index for technical implementations of phase modulators. Therefore, high-speed modulators are typically implemented as semiconductor junction, and the refractive index change is induced by free-carrier injection.

Silicon is not transparent to light with a wavelength below 1 µm. Thus, SOI is unsuitable for applications in the visible wavelength range, such as biomedical applications [47]. SOI is also not suitable for applications such as LIDAR [48], which require high optical powers. The high intensities within the waveguide cause two-photon absorption inducing free-carrier generation that leads to light absorption, which heats and thereby destroys the waveguide.

Table 2: Comparison of key performance indicators of typical silicon on insulator (SOI), silicon nitride (SiN) and indium phosphide (InP) chips of the foundries from Interuniversity Microelectronics Centre (imec), the company LioniX International and Heinrich Hertz Institute (HHI). For SiN, a multi-layer type waveguide called "TriPlex" is considered. For a price comparison, the largest surface indicated to be available for a multi-project wafer (MPW) by the respective foundry in 2021 was assumed and indicated by footnotes. For SOI, only passive runs were considered – functionalities such as photodiodes in SOI would cause additional costs. Only the costs of chip manufacturing are considered, excluding, for example, the assembly or testing cost. Bending radius and typical propagation loss are taken from the respective foundry website. The "cost of U-turn" indicates the cost of the smallest 180° turn using the minimum bending radius of the respective foundry. As example the minimum footprint of an IMEC-SOI U-turn amounts to 10 µm × 20 µm. This figure of merit considers both the potential of miniaturization and the cost per area of the respective technology.

Material platform	**SOI (IMEC[1])**	**SiN (LioniX[1,2])**	**InP (HHI[3,4])**
Transparency	Near-infrared (NIR)	Visible, NIR	NIR
Light generation and amplification	No	No	Yes
Propagation loss	1.5 dB/cm	< 0.3 dB/cm	2 dB/cm
Bending radius	10 µm	100 µm	150 µm
Cost	16 €/mm²	19 €/mm²	63 €/mm²
Cost of U-turn	0.3 € cent	38 € cent	282 € cent
SMF attachment	Difficult; requires complex mode field converters	Simple, e.g., using TriPlex tapers	Difficult; requires complex mode field converters

Therefore, silicon nitride (SiN) in a stoichiometric mixture of Si_3N_4 is a preferred material platform for bio-sensing and for high-power applications. Moreover, SiN is more suitable for ultra-low loss optical resonators as used for optical frequency comb generation [49]. As is the case for SOI, SiN chips also consist of a silicon wafer and a bottom oxide. The waveguides are defined by Si_3N_4 structures arranged in variable configurations [50] that allow cost-efficient implementation of functionalities such as mode-field converters to efficiently couple light guided on the chip to single-mode fibers (SMF).

[1] Information on pricing of IMEC SOI and Lionix TriPlex (SiN): https://europractice-ic.com/wp-content/uploads/2021/01/Pricelist-EUROPRACTICE-General-MPW_3.pdf

[2] Information on bending radius and propagation loss of TriPLex: https://www.phiconference.com/wp-content/uploads/2017/09/Leinse-Photonics-Integration-Conference.pdf

[3] Information on bending radius and propagation loss of HHI InP: https://www.hhi.fraunhofer.de/en/departments/pc/research-groups/photonic-inp-foundry/research-topics/performance-summary-table.html

[4] Information on HHI INP pricing in 2021https://www.hhi.fraunhofer.de/en/departments/pc/research-groups/photonic-inp-foundry/research-topics/prices.html

For an estimate of the chip costs that also takes into account the potential integration density of the various material platforms, the cost to implement a U-turn is considered, see Table 2. As the fabrication cost of large-scale manufacturing are not publicly available, at least not to a degree that would allow comparing different material platforms, the cost of multi-project runs were used to estimate the cost-per-area. In terms of cost-per-area, SOI is roughly on par with SiN. However, when considering that SOI allows much smaller bending radii than SiN, SOI allows significantly higher integration densities. SOI is two orders of magnitude lower in cost than SiN.

The comparison of the different material platforms assumes that the chip size is limited by the waveguide bend radii and not by other elements such as a Mach-Zehnder modulators, or electrical bond pads. Moreover, only cost for MPW runs were considered. However, for larger volume the cost advantage of SOI-technology is very likely to be even larger compared to SiN, as there is an infrastructure for large-scale manufacturing for SOI that is not available for SiN.

Despite its attractive cost structure and suitability for mass manufacturing, the SOI platform has two shortcomings that are subject to very active research: The first is the difficulty to connect waveguides of PICs to other optical devices such as single-mode fiber (SMF). The second shortcoming is the lack of a silicon laser as a fundamental building block due to the lack of a direct bandgap in silicon.

The challenge in connecting optical fibers lies mainly in the large refractive index contrast of typical PIC waveguides with respect to the surrounding oxide. This refractive index contrast confines light strongly. On the one hand, this is an advantage as it allows tight waveguide bends. Commercial foundries typically offer bending radii down to curvature radius of 10 µm, while the minimum demonstrated bending radius is in the range of few micrometers [51]. As a disadvantage, the resulting mode fields are in the sub-micrometer range. The small mode field diameters are a problem for coupling to SMF as here the mode field diameter is in the range of 10 µm. These highly dissimilar mode fields couple only with very low efficiency to SMF and thus require expensive and large on-chip mode-converters.

The second challenge, the missing functionality of a laser on SOI chips, is due to the indirect bandgap structure of Si that does not allow efficient radiative recombination of electron-hole pairs due to competing non-radiative transitions. Therefore, an SOI chip itself cannot generate light but must be connected to a laser. Connecting SOI chips to lasers using an SMF is a conceptually straightforward approach, see Figure 3.1(a). However, the resulting discrete devices are costly and large, making them unsuitable for mass-market applications.

3.2 Monolithic and Heterogeneous Integration

So far, different material systems have been considered that have different functionalities and advantages and disadvantages. To create an integrated system, components of the different material platforms have to be combined. A conceptionally straight forward approach is to implement all functionalities on one direct-bandgap semiconductor platform, such as InP [1], see Figure 3.1(b). This monolithic integration approach results in highly integrated optical systems featuring lasers, modulators and detectors. InP as a material platform cannot rely on the technological achievements and advantages of silicon-based micro-fabrication such as relatively simple oxide growth, fabrication on 12-inch-wafers and mature etching processes, and is therefore technologically more complex and expensive.

As a result, InP chips are about four times more expensive than SOI already for an identical surface area. Additionally, InP does not allow the high integration density as SOI: The minimum bend radius of an InP waveguide, as provided by foundries, is about 150 µm, while Si waveguides can have a bending radius of 10 µm and below. Assuming that the required surface of an integrated circuit scales with the square of the bend radius, InP circuits are about 200 times larger than SOI circuits. Therefore, InP appears to be three orders of magnitude more expensive than SOI, see Table 2. In reality, the price difference will likely be much lower, as bending radii are usually not the only aspect limiting the size of photonic chips, however, there is a clear trend indicating that SOI chips are significantly lower in cost than InP chips.

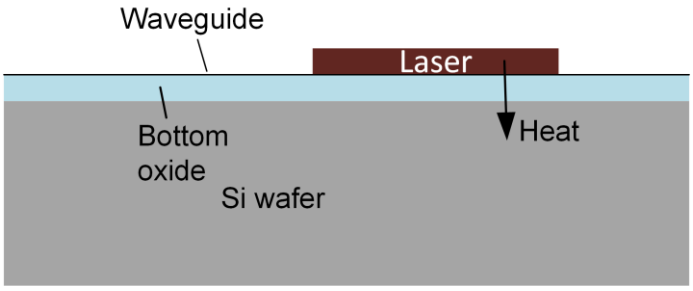

Figure 3.2: Side view of the laser in Figure 3.1(c). The InP portion of the laser is bonded onto a silicon-on-insulator (SOI) wafer. The active region is thus thermally isolated from the silicon (Si) wafer by the bottom oxide, which is a disadvantage for thermal management.

Additionally, when all building blocks such as lasers, modulators, and other functionalities are monolithically integrated on one common substrate platform, individual components cannot be tested and pre-selected. The individual building blocks' fabrication yields thus have to be multiplied to obtain the fabrication yield of the PIC, which makes monolithic integration very intolerant to failure of individual building blocks [4].

The relatively high cost and fabrication complexity of InP and the physical limitation of the SOI platform are well addressed by the approach of "Heterogeneously Integrated InP/Si Photonics" [2], [52]. Here, InP portions of various sizes are bonded to a structured SOI-wafer using a plasma-assisted process; see Figure 3.1(b). The plasma activates the wafer surface and increases the amount of Si-OH groups, which are crucial for good adhesion. In a subsequent step, the InP portions are structured to create waveguides. The structuring of the InP portion can thus rely on high alignment accuracy with respect to the SOI structures and is compatible with large-scale 12-inch-wafer fabrication.

However, the bonding of InP portions to SOI wafers has potential disadvantages concerning thermal management. There is typically 2 µm of buried oxide in-between the active InP region and the Si base wafer, see Figure 3.2. The active lasing region is thus thermally isolated from the Si wafer, which may be a problem for heat dissipation [53], [54] and may limit the operation lifetime of the laser. The fact that Intel is shipping transceivers in large quantities based on heterogeneous integration [55] indicates that the thermal problems and yield problems, at least for the case of coarse wavelength division multiplexing (CWDM) transceivers, are solved.

However, as monolithic integration, the heterogenous integration approach does not allow testing and pre-selection of individual components. Therefore, yield is very likely a critical aspect of the technology. Moreover, heterogenous integration requires large investment in fabrication facilities, and is inherently not very flexible.

3.3 Hybrid Integration

To avoid the complex and technologically inflexible approaches of monolithic and heterogeneous integration, systems can be built by combining different chips on a package level, see Figure 3.1(d), and by optically coupling them to each other [5], [56], [57]. To create a hybrid integrated optical system, individual optical devices, e.g., an SOI chip and an InP laser, have to be carefully aligned and fixed on a common carrier in a way that light is coupled from one optical device to the other forming a multi-chip module (MCM).

An MCM system could, for example, consist of several InP lasers each emitting at different wavelength, and an array of modulators realized in SOI technology. An arrayed waveguide grating (AWG) combines the light of different lasers into one waveguide and may be realized in a low-loss platform like SiN. No performance compromises have to be made, as for each functionality the ideal material platform can be chosen.

Moreover, MCMs allow preselection of components [58]. To this end, all photonic components are tested on wafer-level, e.g., by coupling light in and out of device facets of individual photonic components. As malfunctioning devices may be disregarded for further fabrication, a high component yield can be achieved.

Hybrid integration also offers a high degree of flexibility as different types of MCMs can be built with relatively low process development effort, at least compared with heterogenous or monolithic integration.

Using MCMs also facilitates thermal management [2], [57] as components are not situated on the same substrate and thus thermally isolated from each other. For example, a laser is less likely to heat a nearby component if it is not in

physical contact. In MCMs, the individual chips can also be in thermal contact to heat sinks or are operated using active temperature controllers.

The process flow to assemble hybrid multi-chip modules consists of wafer-level fabrication of optical chips, such as lasers or silicon (Si) photonic integrated circuits (PIC), followed by testing their optical and electrical performance. The test step identifies defect chips. Wafer-level testing is a desirable approach, as it can be automated to a large degree [56], [57]. Subsequent to testing, all components are assembled such that light is coupled between the individual chips.

However, a scalable assembly process of such hybrid optical systems is considered to be one of the critical problems of photonics system manufacturing [44]. The problem is caused by the fact that light has to be efficiently coupled between the waveguides of the different components either by bringing them into direct contact or by free space-coupling. In particular, the position accuracy when fixing single devices of an MCM is challenging: The alignment tolerances must be significantly smaller than the mode-field dimensions. As the mode field diameters are typically in the range of 1.5 µm to 3 µm, chips must be positioned and fixed with sub-micrometer accuracy [57]. Standard pick-and-place technology cannot reach sub-micrometer accuracy as it uses camera vision or optical distance sensors to position components resulting in a best-case accuracy of about ±1 µm.

To achieve sufficiently accurate positioning, active alignment has to be used. During the alignment process, the components must be operated. The position of chips with respect to each other is then optimized to achieve best coupling. In the best coupling position, the components are fixed by, e.g., curing a UV-curable adhesive. Compared to the camera based, passive assembly this so-called active assembly is time-consuming and complex [59], as the operation of components requires complex optical or electrical connections.

Even worse, while curing an adhesive for fixing the components, the devices have to be held at the optimal position during curing. In case of thermally cured adhesives, this is a slow process taking several minutes, depending on the epoxy used [56], [59], [60]. UV curing cannot speed up the process to a sufficient degree, as most low-shrinkage adhesives also have a curing time that extends up

to minutes for reaching a fully cured state. Additionally, there must be little or no heating during curing to avoid freeze-in of thermal stress, limiting the maximum UV light power for curing, and therefore effectively resulting in longer curing times.

In many cases, free-space propagation or mode field matching between optical components is needed. Therefore additional optical elements such as lenses or mirrors [5], [57] must be placed and fixed with sub-micrometer accuracy, further complicating the assembly process. Therefore optical system assembly is the key cost driver for the fabrication of photonic components [4].

Alternatively to free-space propagation, photonic components can often be coupled with direct physical contact. Contact coupling is in particular standard for coupling of photonic chips to SMF. Such physical contact coupling implies that chips require complex and expensive mode field converters to relax alignment accuracy and increase the coupling efficiency. They may, for example, need overgrowth with a high refractive index material or membrane-type mode field converter. However, even these strongly simplified alignment processes may take up to ten minutes, even in a fully automated process [59].

3.4 Hybrid Integration with 3D-printed Micro-Optics

A relatively novel assembly concept to form MCM relies on a very different approach, namely on “Photonic Wirebonds” (PWB) [61]–[63], see Figure 3.1(e). Here, optical components such as InP-lasers and SOI chips or SMF are fixed on a common carrier with a typical accuracy of about ±20 µm. Liquid UV-curable polymer is drop cast onto the assembly and serves both as resist material for 3D-printing and as an immersion medium for a high-NA objective lens.

A lithography system then localizes the device facets with sub-100 nm precision using different machine vision techniques for marker and optical interface detection. Subsequently, a waveguide trajectory is calculated, connecting the two devices. By scanning a femtosecond laser that triggers two-photon polymerization, the liquid photoresist is solidified to define a free-standing optical

waveguide; see Chapter 2.1 for further details on the fabrication method. After the 3D-printing process, the remaining polymer is removed using a chemical solvent as a developer. The PWB is clad by a UV curable polymer that protects the connection. The refractive index of the cladding is chosen such that the PWB is single-mode.

To efficiently couple to individual photonic components, PWBs may also feature a 3D-printed taper, adapting different mode field sizes by altering the waveguide's cross-section towards the device facet. This allows mode field matching over a range between approximately 1.5 µm to 10 µm.

Depending on the device type involved, fabrication times below 10 s per PWB are possible. Coupling losses can be below 1 dB for relevant cases, e.g., for an InP laser coupled to an SOI chip [63]. The coupling losses are mostly caused by a mode field mismatch of the PWB and the respective photonic device.

The PWB concept is, however, not applicable to all scenarios. The need to position optical components on a carrier before fabricating the PWB implies limitations: Typical objective lenses used for lithography have working distances of 250 µm. Therefore, the PWB cannot be manufactured close to anything protruding more than 250 µm above the lowest part of the PWB trajectory. Moreover, the complete assembly is in contact with photoresist and solvent during the PWB-fabrication process. Contact with photoresist and solvent is problematic if incompatible materials or structures are present in the MCM, such as microelectromechanical system (MEMS) actuators that would be destroyed by contact with any liquid substance.

Finally, the assembly of photonic systems with PWBs is a "disruptive" technology. It may require changing the assembly routine to be compatible with the 3D-printing process, making its market penetration challenging.

This work' approach relies on 3D-printed lenses, see Figure 3.1(f). With the same 3D-printing technology as described for PWB, the lenses are fabricated directly on the chip facet, see Figure 2.1 and Figure 2.2 for details on the 3D-printing process of lenses. The 3D-printed lenses allow to shape light emitted by a photonic chip into free space and ensure mode-matching between different chips. The free-space transmission between individual components has

additionally the advantage that other functionalities such as optical isolation can be implemented [5] that so far cannot be efficiently realized within a PIC.

As lenses can be printed on any photonic component, even complex photonic systems can be built, such as transmitter modules for optical communication, see Figure 3.3 for a schematic illustration. Lenses fabricated by 3D-printing can be manufactured prior to assembly of photonic components. Lenses could therefore be fabricated on wafer-level, prior to dicing into single chips. Therefore, 3D-printed lenses are conceptionally suitable for wafer-scale manufacturing.

In most cases, the facet attached beam shapers are lenses or total-internal-reflection (TIR) mirrors. The lens or mirror shape is described by a suitable mathematical function, for example, by a polynomial function. Freeform lenses can match mode fields of different photonic components to each other or to the mode fields of SMFs. Freeform mirrors allow redirecting the light to build very compact optical assemblies of edge- and surface-emitting components.

Additionally to mode-field matching, the 3D-printed lenses can expand an optical beam to 25 µm or more, increasing the 1 dB alignment tolerance to ±5 µm, allowing relatively simple chip alignment. Due to the increased alignment tolerance camera-based passive alignment can be used, see Section 4 for further details.

However, when expanding a mode-field, the divergence of the radiated beam will scale reciprocally with the beam expansion. As a consequence, highly expanded beams are inherently very susceptible to angular misalignment. This behavior can be described by the optical etendue, which consist of the product of the mode-field surface element dA and the solid angle dΩ of the light emission of the mode-field. The entendue is preserved for any lossless optical transformation,

$$\mathrm{d}\Omega_1 \mathrm{d}A_1 = \mathrm{d}\Omega_2 \mathrm{d}A_2.$$

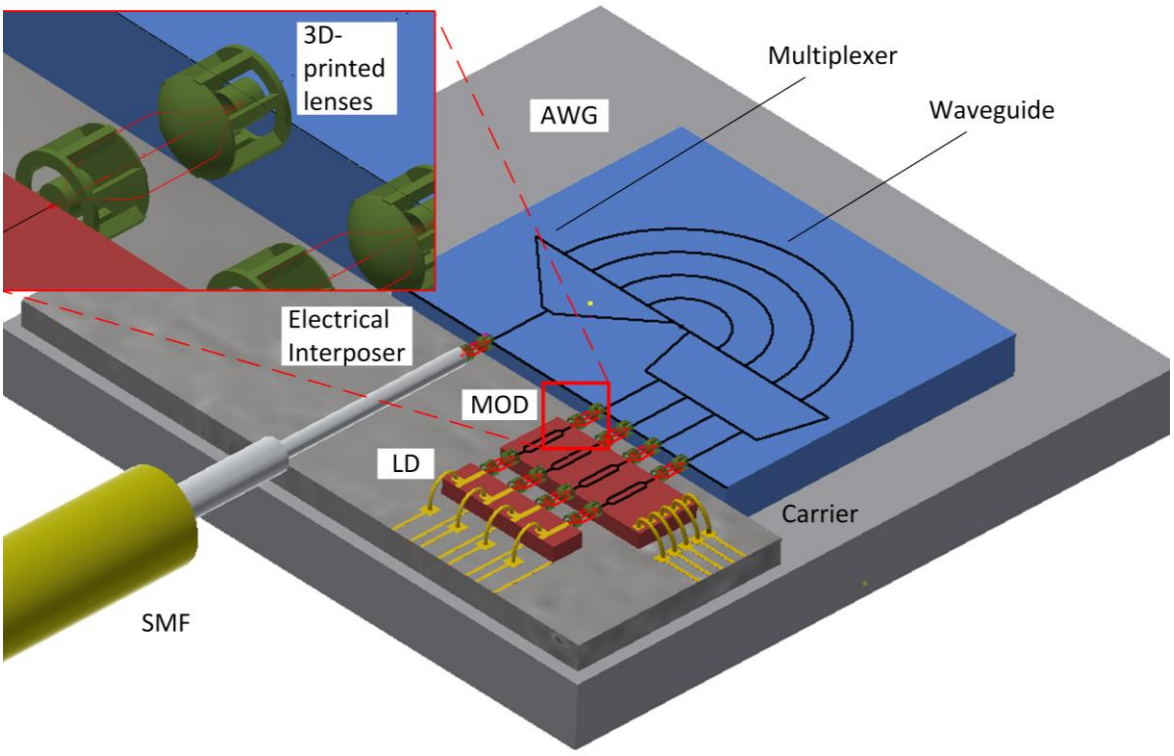

Figure 3.3: Schematic of an optical assembly consisting of laser diodes (LD), a single-mode fiber (SMF), modulators (MOD) and an arrayed waveguides grating (AWG) for optical multiplexing. All components are equipped with tailored coupling elements such as beam expanders. The expanded mode fields relax transverse position accuracy requirements of photonic components and simplify assembly onto a common carrier.

For best coupling, two mode-fields must be identical in phase and intensity. The transverse coupling tolerances scale with extension of the mode-field of a surface A, while the angular coupling tolerances scale with the solid emission angle Ω. If one compares two mode-fields to be coupled with small surfaces A_1, and a large solid emission angle Ω_1, the coupling is more susceptible to transverse offset than two mode-fields with large A_2 and small Ω_2. For angular misalignment, the mode-fields with A_2 and small Ω_2 are more susceptible than the mode fields with small A_1 and large Ω_1. In practice, however, it is typically simpler to control angular alignment [59]. Therefore, mode-field expansions achieved in this work allow a significant simplification of hybrid photonic system assembly.

3.5 Ground-Based Observation of Stars

In ground-based observation of starlight, extraterrestrial objects are imaged, and analysed by spectroscopic methods. A prominent example of such ground-based observation is the discovery of new extraterrestrial planets [64]. Due to a spatially and temporally varying refractive index of the atmosphere, imaging of extraterrestrial objects on the earth's surface is perturbed by optical turbulence. Therefore, most telescopes rely on an adaptive optical (AO) system [68], which consists of a wave front sensor that detects wavefront distortion, and an adaptive optical element that corrects these distortions. To this end, the front-sensor continuously feeds the deviation from an undistorted plane wave front to an AO, which may be implemented as a deformable mirror, capable of correcting the phase-front deviations. The wave front sensor is often implemented as a Shack-Hartman sensor which consists of a micro-lens array in front of a camera chip. As the wavefront sensor always requires a certain intensity level to properly operate, it may need sufficiently strong light from a "guide star" which may be a bright star in the surrounding of the observed object or an artificially generated luminescence by a strong terrestrial laser pointed at the sky.

So far, multimode fibers are employed to couple light from a telescope's image plane to a spectrograph. Multi-mode fibers have some disadvantages, as due to temporarily varying light coupling conditions and vibration inside the telescope, different optical modes may be excited, resulting in modal noise. This is a disadvantage for spectroscopy as the signal will locally fluctuate over time and may thereby decrease resolution [65]. Moreover, a multi-mode fiber has a higher etendue than a single-mode fiber and does not allow for diffraction limited operation of spectrographs.

Recent activities aim therefore at coupling light into single-mode fibers (SMF). Because a single mode can be imaged to a smaller spot on a spectrometer detector than several modes, the resolution of the spectrograph may be increased [66]. In other words, an SMF instead of a multi-mode fiber is similar to using a smaller slit width for the entrance aperture of the spectrometer. Another advantage is reduced modal noise [65], as only a fundamental mode with two orthogonal polarization states can be excited in an SMF. Moreover, SMF offer

the possibility of integrating fiber Bragg gratings [67] for suppression of stray light in the atmosphere. The optical grating reflects unwanted light with very high wavelength selectivity.

The requirements that need to be fulfilled by an adaptive optical system for coupling into an SMF are considerably higher than for multimode fibers due to the smaller mode field diameter. For a sufficiently fast wavefront sensing, current systems require a large fraction of light, resulting in high coupling loss. This is particularly problematic in the absence of bright guide-stars.

Moreover, the adaptive optics is physically never at the same location as the SMF. Therefore, also common-path aberrations (CPA) deteriorate coupling into optical fibers. These occur, as current systems for wavefront sensing do not sense the wavefront at the fiber coupling site, but at a different location in the beam path. Any vibration or aberration that occurs between the fiber coupling site and the wavefront sensing site will thus result in additional coupling loss.

Within this work, a solution to mitigate the effect of optical turbulence was proposed and tested by implementing a lossless wavefront-sensor at the coupling interface from free-space to the SMF. To this end, instead of an SMF with only one fiber core, a multi-core fiber with seven fiber cores was used. Only the center fiber guides light to a spectrograph. The surrounding fiber cores carry an error signal that can be fed to a tip/tilt correction or AO element, see Figure 4.1.

As a main advantage, the approach investigated in this work will only draw light from the spectrograph in the case of a distorted wavefront. It does thus not reduce the coupling efficiency in the undistorted case. As this approach only allows to correct first-order tip/tilt aberration, it has in most situation to be combined with conventional wavefront sensors for higher order correction of aberration. These high-order aberrations vary, however, with a smaller temporal frequency and can thus be corrected using a smaller fraction of light being coupled to a wavefront sensor compared to a situation without tip/tilt correction.

In this work a multicore-fiber with seven single-mode cores was used, see Section 5 for further details. Follow up work [13] relied on fiber bundles with a center single-mode core and surrounding multimode cores for the error signal, allowing a more efficient collection of an error signal.

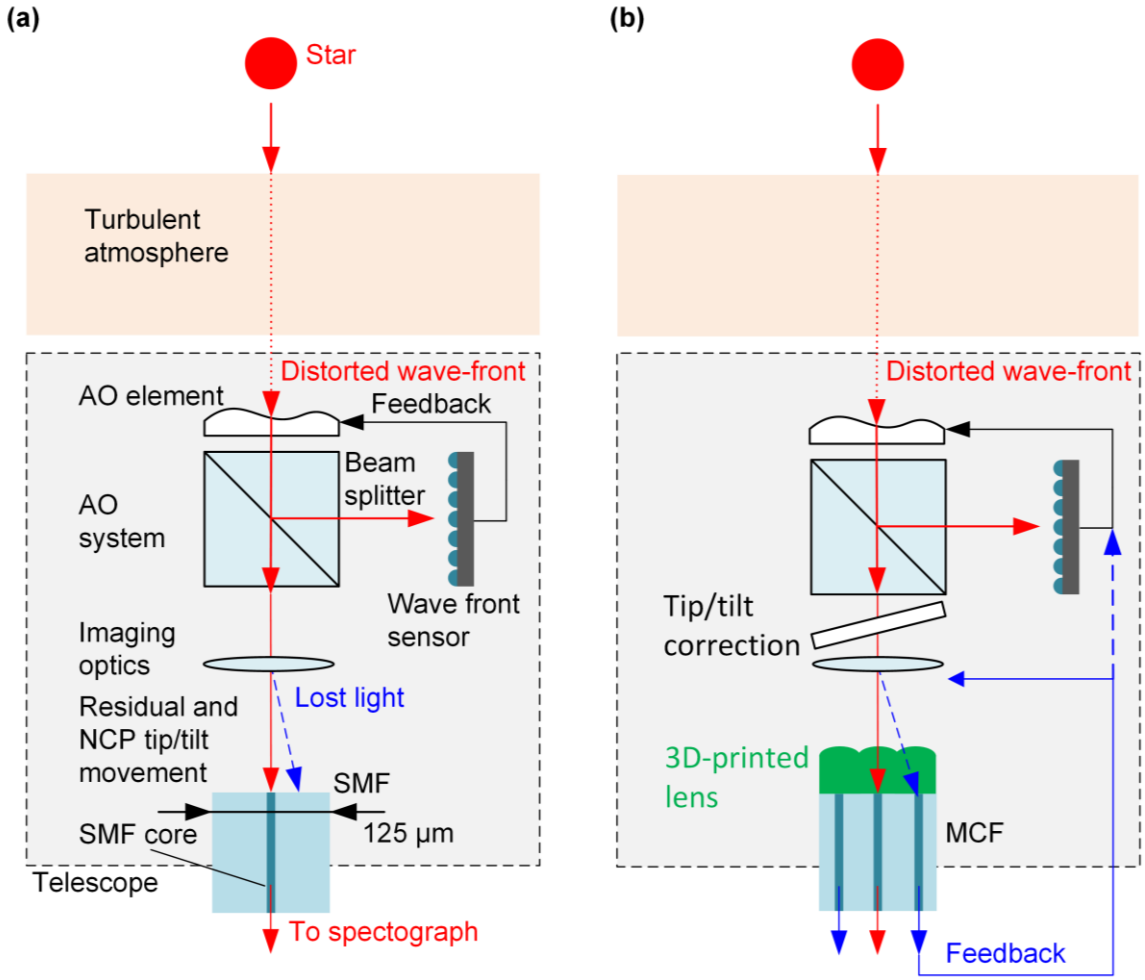

Figure 3.4: Beam path of a terrestrial telescope with an adaptive optical system for coupling into single-mode fibers (SMF). Light (red) from a star as a point source is transmitted through the optically turbulent atmosphere causing wave front distortions. The light is collected by a primary mirror or lens (not shown). Inside the telescope, light propagates through an adaptive optical (AO) system consisting of a beam splitter, an AO element and a wave front sensor. The beam splitter couples light to a wave front sensor. The wave front sensor signal is fed back to the AO element, often realized as a deformable mirror. After coupling into an SMF core, light is guided to a spectrograph located outside the telescope. **(a)** The AO system can only correct part of the aberration. Some residual tip/tilt movement and non-common path aberration (NCP) cause light not to couple into the fiber (blue), resulting in optical loss. NCP results from the fact that the AO system is not located at the SMF, and the telescope shows some vibration or long-term drift. **(b)** 3D-printed lenses (green) on the facet of a multi-core fiber (MCF) allow detecting light (blue). The light (blue) can be used to create a error signal that is fed back to a tip/tilt correction device, for example implemented as a tiltable mirror, or optionally an AO element.

3.6 Scanning Probe Microscopy (SPM)

Scanning probe microscopy (SPM) is a technology that provide local information of a sample surface using a scanning probe. The probe is a sharp tip, often created by an anisotropic Si-etching process. In SPM measurements, a scanning mechanism moves the probe along a trajectory parallel to the sample surface, see Figure 3.5. During the movement in *x*- and *y*-direction, the sample-probe interaction is measured. In most implementations, the signal generated by a sample-probe interaction is fed back to the scanning mechanism to control the *z*-distance between probe and sample.

The resolution of SPM methods is defined mainly by the probe-tip interaction, provided that the scanning instrument is sufficiently stable and accurate. The probe-tip dimension and sample-to-probe gap can be in the sub-nanometer range, which allows probing of single atoms. In practice, the tip is likely to degrade over longer scanning periods, either due to mechanical wear or to contamination by dirt. Therefore, the resolution of SPM devices generally depends on application, measurement time, and tip geometry.

There are many SPM methods, which rely on fundamentally different sample-to-tip interaction methods. Historically, Binnig *et al.* [68] were the first to implement scanning tunneling microscopy (STM) as the first SPM method with high scientific relevance. Here, a tip moves along a conductive sample surface for measuring the tunneling current from sample to tip. The sample-tip tunnel

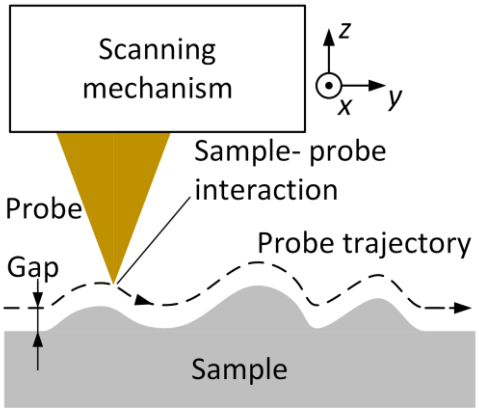

Figure 3.5: Generic schematic of a scanning probe microscope. A scanning mechanism moves a probe along a probe trajectory parallel to the sample surface. During the movement in *x*- and *y*-direction, sample-probe interaction is measured. In most implementations, the signal generated by sample-probe interaction is fed back to the scanning mechanism to control the *z*-distance between probe and sample. The probe-tip dimension and the sample-to-probe gap can be in the sub-nanometer range, allowing to study single atoms.

current depends on the sample's local density of electron states. As the density of states varies with respect to the atom position in the lattice, single atoms can be imaged.

3.7 Atomic Force Microscopy (AFM)

Following the development of STM, atomic force microscope (AFM) was employed to measure the sample topography [69], [70], see Figure 3.6. Unlike STM, AFM is also suitable for non-conductive samples. To perform AFM measurements, the tip-sample force is measured instead of the tunnel current. In most implementations, the sample-probe gap is kept constant while moving the probe along the sample surface.

The probe-sample force in AFM is often described by the Lennard-Jones potential, which consists of an attractive van-der-Waals term and a repulsive exchange interaction term. The van-der-Waals force of two identical objects in vacuum is always attractive. The van-der-Waals force is based on the observation that even non-polar molecules will still have a fluctuating polarisation.

A second approach to describe van-der-Waals forces was developed by Lifschitz et al. [71]. The approach is an extension of the Casimir effect. Here, the vacuum fluctuation is used to explain the attractive van-der-Waals forces. The vacuum fluctuation consists of virtual particles that are created and annihilated in vacuum. These particles have a certain momentum and therefore exert a force on objects. Within the gap between sample and probe the wavelength of such virtual particles has to be an integer multiple of half the probe-sample distance. The number of virtual particles in the probe-sample gap is thus reduced, thereby also the outward pressure on probe and sample is reduced, resulting in effective attraction.

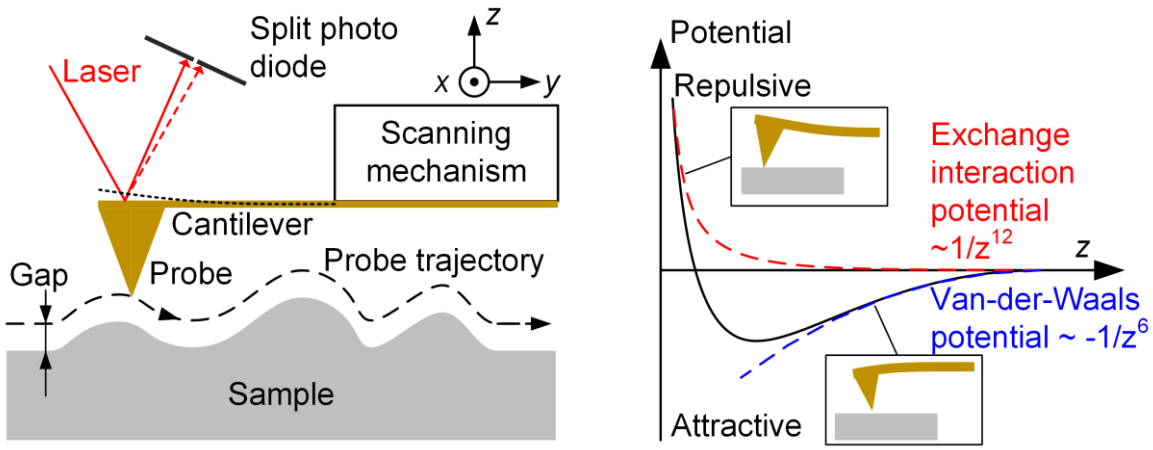

Figure 3.6: Working principle of an atomic force microscope (AFM). **(a)** Common implementation of a scanning probe microscope (SPM). The sample-to-probe force deforms the cantilever. The deformation is indicated by a dotted-line. The cantilever deflection can be measured by a laserbeam (red), reflected at the cantilever and recorded by a split photodiode. The split photodiode consists of two photodiodes. By substracting the signal of both photodiodes, laser spot movement (red dashed line) can be recorded. The cantilever deflection is used as a feed back signal when moving the probe along a probe trajectory parallel to the sample surface. **(b)** A typical sample-probe force curve when changing the sample-to-probe distance. Due to van-der-Waals interaction the probe-sample force is attractive at relatively large distances bending the cantilever towards the sample. Due to exchange interaction the probe-sample force is repulsive at short distances, bending the cantilever away from the sample. While the 6th-order distance dependance of the van-der-Waals potential can be theoretically derived, the 12th-order power dependance is chosen purely empirical.

The repulsive exchange interaction in AFM originates from the fact that an ensemble of two, or more, fermionic particles with the position **r** and the spin *s* have an antisymmetric wavefunction Ψ *i.e.*

$$\Psi(\mathbf{r}_1, s_1; \mathbf{r}_2, s_2) = -\Psi(\mathbf{r}_2, s_2; \mathbf{r}_1, s_1).$$

If the position **r** and the spin *s* of different particles are identical, Ψ has to be zero for an antisymmetric wavefunction, resulting in a probability of zero for such a configuration. This observation is known as the Pauli principle. The Pauli principle results in a strong repulsive force between Fermions at short distances. In the Lenard-Jones [72] potential this repulsive force is modelled as a 12th power dependence of a repulsive potential on the distance. This is, however, only a qualitative description that was chosen empirically.

Both attractive and repulsive force between probe and sample can be measured by the cantilever deformation. The cantilever deformation can be recorded by a laser beam, indicated in red in Figure 3.6, which is deflected at the cantilever and detected by a split photodiode in a certain distance from the cantilever. The split photodiode consists of two photodiodes. If the laser is more deflected towards one of the photodiodes this photodiode will create a larger photocurrent than the other photodiode. By subtracting the signals of both photodiodes, the laser spot movement (red dashed line) can be recorded very precisely. The cantilever deflection is used as a feedback signal for controlling the vertical position of the tip and cantilever with respect to the sample when moving the probe along a probe trajectory parallel to the sample surface.

Most AFM measurements of the static deflection are performed in the repulsive region. Due to physical contact between probe and sample, these so-called contact measurements create strong wear on the probe tip and require regular probe exchange. In practice, it is therefore advantageous to measure in the region with attractive sample-probe force. Here, the cantilever is driven by a piezo actuator and oscillates close to its resonance. The sample-to-probe interaction changes the amplitude and the phase of the oscillating cantilever. Thus, the oscillation amplitude and phase can be used as an indirect means to determine sample-probe distance. In this "dynamic-mode AFM," there is no probe-sample contact and thus very low wear of the probe tip.

AFM has high industrial relevance, as it combines high vertical resolution (z-direction) with high lateral resolution (y, x-direction). It can, for example, be used to measure either photoresist thickness or the depth of etched structures in microfabrication processes. AFM has a significantly higher lateral resolution than optical metrological methods, which is particularly relevant for nano-structured samples. Additionally, some artifacts, present in optical methods such as white-light interferometry, such as optical interference at thin layers do not distort AFM measurements, as it is a purely mechanical method.

3.8 Scanning Near-Field Optical Microscopy (SNOM)

Microscopy methods that rely on far-field imaging have a resolution limit imposed by the radiated light of the object to be imaged. A one-dimensional illustration of the situation is depicted in Figure 3.7(a). The light radiated from this object can be decomposed into plane waves. To optically resolve an object with dimensions of $2\pi/k_x$, the wavelength of plane waves propagating along the x-direction have to be smaller than $2\pi/k_x$. In general, it is possible to have arbitrarily large k_x, and thus infinitively small particles, however, waves with

$$k = \sqrt{k_x^2 + k_z^2} \text{ and } k_x > k'_0$$

must have an imaginary k_z. When inserting such an imaginary k_z into the solution of a plane wave equation, the wave equation describes a field with exponentially decaying intensity, Figure 3.7(b), which is not radiated.

These consideration can be extended to a three-dimensional case. Here, any wave vector with component k_x, k_y, k_z and a magnitude

$$k_0 = \sqrt{k_x^2 + k_y^2 + k_z^2}.$$

and wavevectors

$$k_0^2 < k_x^2 + k_y^2$$

have an imaginary k_z and are not radiated.

To far-field imaging has to rely on capturing radiated modes with an objective lens with an aperture cone α. Considering the one-dimensional case of Figure 3.7 (a), this allows to capture modes with

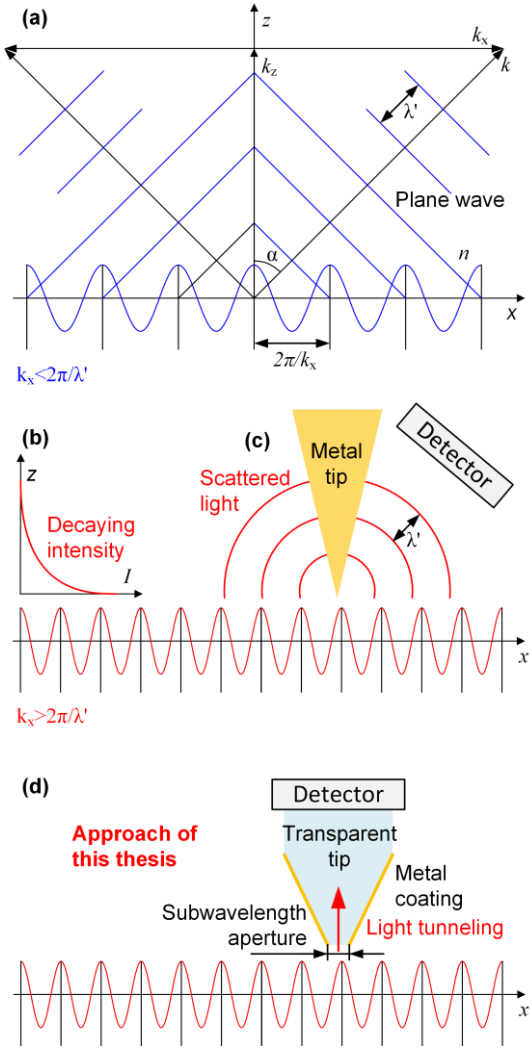

Figure 3.7: Two-dimensional illustration of far- and near field imaging techniques. **(a)** Far-field imaging of plane waves that are radiated from a sample plane at $z = 0$ (blue) in an angle α with a wavlength λ' in an immersion medium with refractive index n. **(b)** Waves with $k_x > k'_0$ (red) are not radiated, as k_z would be imaginary, leading to an exponential decay of light intensity I in z-direction. **(c)** To convert non-radiated waves into radiated waves, a scattering metal tip can be brought into the decaying field. The scattered light can be captured by a detector. For imaging, the tip has to be scaned in x-direction while maintaining its z-position. **(d)** Alternatively to a scattering metal tip, a metal coated, light transparent tip with a subwavelength aperture can be brought into the evanescent field. The light tunnels through the aperture and then propagates along the transparent structure to a detector. The transparent tip is often realized as a pulled or etched fiber. In this work a 3D-printed tip was used.

$$\sin\alpha = \frac{\lambda'}{2\pi/k_x} \Leftrightarrow \mathrm{NA} = \frac{\lambda}{2\pi/k_x},$$

where λ is the vacuum wavelength and λ' is the wavelength in an immersion medium with refractive index n.

To measure objects with dimensions $d_x < \lambda$, spatial frequencies with $1/d_x > 1/\lambda'$ and $k_x > k_0$ are required, which leads to an imaginary k_z. The problem of imaging with sub-wavelength resolution is thus that despite the existence of plane waves with a k-vector that would allow sub-wavelength resolution, these modes are not radiated.

To achieve higher resolution, one has to convert non-radiated modes to radiated modes. To this end, a scattering tip has to be brought into the evanescent field

that converts the exponentially decaying field back into a radiated field, see Figure 3.7(c). This probe can be a small dipole like a scattering metallic nanostructure or a sub-wavelength aperture. The scattered far field can then be captured by a detector in the far field, which is often combined with a microscope objective lens to increase collection efficiency.

Alternatively to the scattering tip in Figure 3.7(c), a sub-wavelength aperture may be used, see Figure 3.7(d) that can be implemented at the end of an optical fiber. Here the near-field tunnels through the sub-wavelength tip and then propagates along the fiber to a detector. In this approach, the collection efficiency can be higher than in the approach using a scattering tip. Additionally, only a far field-illumination is required and no far field collections, as a fiber-coupled detector can be used. Both approaches to convert non-radiated modes into radiated modes allow to image below the diffraction limit. The resolution limits are mostly due to the probe geometry and signal-to-noise limits as an infinitively small aperture or tip only scatters a very small fraction of light.

The first implementation of a SNOM was based on a sub-wavelength aperture [73] and was experimentally realized in the 1980s [74]. In the respective publication, a sub-wavelength aperture was formed by a metal-coated fiber that is scanned along the sample plane. The authors claim resolution in the $\lambda/20$-regime. The technology was later named “scanning near-field optical microscopy” (SNOM) [75] .

However, near-field measurements suffer from high technical complexity. For SNOM with a scattering type of probe, Figure 3.7(c), a distance feedback mechanism must be combined with light focused and collected on and from a microscopic tip. This combination of optical light collection and distance feedback mechanism is difficult to implement, as it is difficult to align the SNOM tip with a focus spot of an objective lens that is required to achieve reasonable collection efficiencies.

In the case of aperture type SNOM the preparation of suitable apertures is challenging. The aperture fabrication requires a pulling or an etching process of an optical fiber. Such fabrication processes are often not reproducible. Moreover, after gold coating, the aperture has to be somehow opened, e.g., by focused ion

beam milling, directive coating or by scratching the probe tip along a sample surface, which are all processes with poor reproducibility.

Due to the manufacturing complexity and the difficult interpretation of SNOM signals, the technique has not achieved widespread use in industrial applications. This work introduces a new paradigm that relies on 3D-printing of mechano-optical systems thus paving the way to more reproducible and straightforward fabrication methods for SPM in general and SNOM in particular, see Section 6 for further details.

Additionally, aperture type SNOMs are prone to artifacts: The goal of most SNOM measurements is to determine the interaction of light with a structure under investigation. One could, for example, aim at observing an optical resonance, a plasmonic field enhancement, or fluorescence with very high spatial resolution. However, as most structures have a certain topography that changes the probe-to-sample distance, most SNOM images show artifacts that are induced by altering the probe-to-sample distance when scanning along the sample topography [76]: As an example, the probe might get in direct contact with the sample at a protrusion originating from fabrication inaccuracies, see Figure 3.8. This leads to enhanced scattering and may be misinterpreted as a local change of the optical sample properties. This effect is also referred to as “topographic artefact” in SNOM experiments.

The true SNOM signal typically has a different resolution than the topography signal, as the aperture is usually much larger than a protrusion at the aperture, and generally is slightly offset. The topography-induced artifact cannot be removed by a lock-in principle, e.g., locking the SNOM signal to the signal that causes the SNOM tip to vibrate. Such topographic artifacts can be, however, avoided by scanning the tip at constant gap width h, which may damage the tip as the height control will not follow the sample geometry and restricts SNOM measurements to very flat sample geometries.

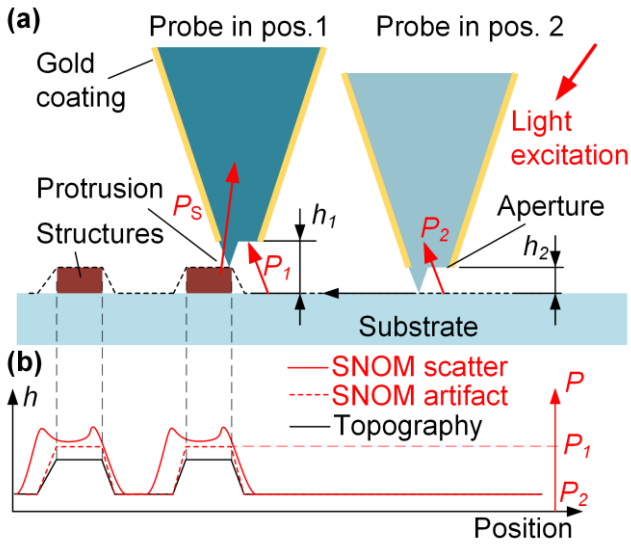

Figure 3.8: Signal formation of scanning near-field optical microscopy (SNOM) when scanning two structures on a substrate. **(a)** Schematic of an aperture-type SNOM. A probe consists of a sub-wavelength aperture formed by a gold-coated transparent tip. A red arrow indicates light excitation. The probe is typically in contact with the substrate at a corrugation that offsets the aperture from the sample by a distance h_2 when scanning along a flat substrate (position 2). When scanning along a structure, the tip is lifted to a distance h_1 from the substrate. The power coupled into the tip P_1 at a distance h_1 and P_2 at a distance h_2 is in general different, in this illustration $P_1 > P_2$. The aperture thus behaves like a distance sensor that indicates distance from the substrate. Additionally, a power P_s is scattered at the structures and coupled into the aperture. This signal contains the actually relevant information, as it stems from interaction of light with the structure under investigation. **(b)** Schematics of the height and power levels measured in (a). The height is depicted on the left axis (black) the power levels on the right (red). When scanning along structures, the measured SNOM signal partially originates from light scattered at a structure and coupled into the probe with a power P_s. Additionally, the measured SNOM signal depends on the distance h of the aperture to the substrate surface. This dependency leads to a coupled power P_1 at a distance h_1 and P_2 at a distance h_2 that is altered by a change of the probe-sample distance and is an artifact that contains no information about light-structure interaction. As the height change is induced by a small protrusion, it may falsely imply very high SNOM resolution.

4 In situ 3D Nano-Printing of Freeform Coupling Elements for Hybrid Photonic Integration

This chapter discusses optical coupling using *in situ* 3D-printed freeform optics. As these elements are fabricated on the facets of optical chips, lasers and fibers, they are inherently well aligned. They allow coupling losses below 1 dB and relax the translational coupling accuracy requirements for device mounting by mode field expansion.

The following chapter is taken from a publication [J3] in Nature Photonics. To fit the structure and layout of this document, it was adapted accordingly. Methods and Supplementary Information associated with the manuscript can be found in Appendix A.

Author contributions

The author of this thesis designed, simulated, fabricated and characterized coupling structures and devices with help from M. Blaicher, I. Reuter, M. Billah, T. Hoose and A. Hofmann, supervised by C. Koos. Device concepts and coupling schemes were jointly conceived by the author of this thesis, M. Billah, R. Dangel, B.Offrein and C. Koos All authors discussed the data. The project was supervised by W. Freude and C. Koos. The manuscript was written by the author of this thesis, W. Freude and C. Koos.

[start of paper [J3]]

Published in Nature Photonics

In situ 3D Nano-Printing of Freeform Coupling Elements for Hybrid Photonic Integration

DOI: doi.org/10.1038/s41566-018-0133-4

P.-I. Dietrich[1,2,3,*], M. Blaicher[1,2], I. Reuter[1,2], M. Billah[1,2], T. Hoose[1,2], A. Hofmann[4], C. Caer[5], R. Dangel[5], B. Offrein[5], U. Troppenz[6], M. Möhrle[6], W. Freude[2], and C. Koos[1,2,3,**]

[1] Inst. Of Microstructure Technology (IMT), Karlsruhe Inst. Of Technology (KIT), Hermann-von-Helmholtz-Platz 1, 76344 Eggenstein-Leopoldshafen, Germany

[2] Inst. Of Photonics and Quantum Electronics (IPQ), Karlsruhe Inst. Of Technology (KIT), Engesserstr. 5, 76131 Karlsruhe, Germany

[3] Vanguard Photonics GmbH, Hermann-von-Helmholtz-Platz 1, 76344 Eggenstein-Leopoldshafen, 76227 Karlsruhe, Germany

[4]Inst. For Applied Computer Science (IAI), Karlsruhe Institute of Technology (KIT), 76131 Karlsruhe, Germany

[5]IBM Research – Zürich, Säumerstrasse 4, 8803 Rüschlikon, Switzerland,

[6]Fraunhofer Inst. For Telecommunications, Heinrich Hertz Inst. (HHI), Einsteinufer 37, 10587 Berlin, Germany

*p-i.dietrich@kit.edu, **christian.koos@kit.edu

Hybrid photonic integration exploits complementary strengths of different material platforms, thereby offering superior performance and design flexibility compared to monolithic approaches. This applies in particular to multi-chip concepts, where components can be individually optimized and tested on separate dies before integration into more complex systems. However, the assembly of such systems still represents a major challenge, requiring complex and expensive processes for high-precision alignment and careful adaptation of optical mode profiles. Here we show that these challenges can be overcome by *in situ* nano-printing of freeform beam-shaping elements to facets of optical components. The approach applies to a wide variety of devices and assembly concepts. It allows adaptation of vastly dissimilar mode profiles while considerably relaxing alignment tolerances to the extent that scalable, cost-effective passive assembly techniques can be used. We experimentally prove the viability of the concept by fabricating and testing a selection of beam-shaping elements at chip and fiber facets, achieving coupling efficiencies of up to 88 % between an InP laser and an optical fiber. We also demonstrate printed freeform mirrors for simultaneously adapting beam shape and propagation direction, and we explore multi-lens systems for beam expansion. The concept paves the way to automated fabrication of photonic multi-chip assemblies with unprecedented performance and versatility.

4.1 Introduction

Single-mode chip-to-chip and fiber-to-chip interfaces have been a fundamental challenge in integrated optics ever since [44]. A wide variety of approaches has been explored to achieve low-loss coupling with assembly processes of manageable technical complexity [57]. The challenge comprises two aspects: First, on-chip waveguides frequently feature small mode field diameters, particularly when high index-contrast silicon-photonic (SiP) or InP-based components are involved. As a consequence, low-loss coupling requires highest positioning accuracy of optical components, and this can only be achieved by slow and expensive [54] active alignment techniques, where the coupling efficiency is continuously monitored while optimizing the position of the devices [57],[77]. Second, fiber-chip interfaces and chip-chip-interfaces of devices realized on different material platforms often have to cope with vastly different mode profiles and emission directions that need to be carefully adapted for efficient coupling. This requires additional elements such as micro-lenses [78], [79], micro-mirrors [5] or waveguide-based spot-size converters [80], which results in bulky systems and increases the number of components that need to be actively aligned.

Various concepts for coupling light to optical chips have been explored to tackle these challenges. These approaches can be broadly subdivided into two basic concepts: Edge coupling to etched or polished waveguide facets and surface coupling using grating structures that are etched into the top surface of high index-contrast waveguide cores [81]–[84]. Edge coupling has become the mainstay for coupling of InP-based lasers or optical amplifiers to single-mode fibers [85] (SMF) and is also widely used for SiP circuits [86]. For efficient coupling, lensed fibers [85], [87], [88] or discrete micro-lenses [78], [89] are used to reduce the generally rather large mode fields of SMF to those found at the chip facet. This usually leads to tight alignment tolerances, which renders active alignment indispensable [90]. In addition, the preparation of edge-emitting waveguide facets requires delicate polishing techniques that complicate fabrication [91]. The same applies to grinding or etching of lensed fiber tips, particularly when elliptical mode fields for coupling to rectangular waveguides are required [88], [92]. In addition, the numerical aperture (NA) of lensed fibers is limited such that mode field diameters of less than 2 µm are generally difficult

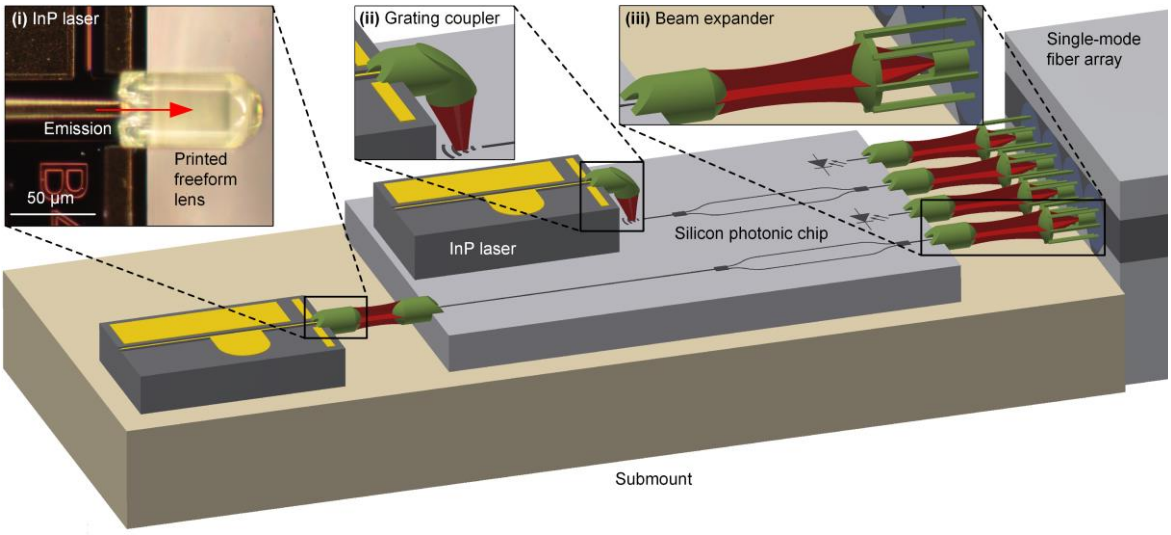

Figure 4.1: Photonic multi-chip assembly combining the distinct advantages of different photonic integration platforms: Optical sources are realized on direct-bandgap InP substrates and connected to a silicon photonic chip which comprises, e.g., Mach-Zehnder modulators and SiGe photodiodes for generation and detection of optical signals. A single-mode fiber (SMF) array is used for connection to the outside world. Freeform beam-shaping optical elements such as micro-lenses or micro-mirrors are used for mode field adaptation (red), thereby enabling low-loss coupling and relaxed alignment tolerances. Inset (i): Microscope image of a freeform lens printed on the facet of an edge-emitting laser. Inset (ii): Schematic of a freeform mirror printed on an edge-emitting laser's facet to enable grating coupling. Inset (iii): Schematic of a pair of beam expanders.

to achieve. For edge coupling to SiP circuits, additional on-chip mode field expanders are required [92], featuring typical lengths of hundreds of micrometers and thus consuming precious on-chip areas. The same applies to adiabatic mode converters [93], which rely on continuous transformation of mode profiles by evanescent coupling to tapered silicon photonic waveguides. Surface coupling can considerably relax the alignment tolerances to values [90] of ± 2.5 µm, but still requires active alignment [54]. In addition, grating couplers are inherently wavelength-dependent with typical bandwidths of less than 30 nm. The resulting assemblies often lead to unfavorable arrangements with fibers mounted typically perpendicularly to the chip surface. Taken together, the manifold challenges and limitations related to chip-chip and fiber-chip coupling represent a major obstacle towards widespread application of hybrid photonic integrated circuits [44], [57].

This paper shows that these limitations can be overcome by *in situ* printing of ultra-compact beam-shaping elements onto facets of optical devices. We exploit direct-write two-photon laser lithography [94]–[96], which has previously been used to realize, e. g., micro-optical elements like lenses, prisms, gratings and axicons [97], [98], phase masks on fiber facets [99], multi-lens objectives for endoscopic imaging [100] as well as collimating optics [101] for light-emitting diodes (LED). We show beam-forming elements with virtually arbitrary three-dimensional geometry, which do not only allow adaptation of vastly different mode profiles but can also relax alignment tolerances to the extent that simple and cost-efficient passive assembly processes can be used. In a first set of experiments, we expand on our earlier work [J6][C3] and demonstrate highly efficient coupling between SMF and edge-emitting semiconductor lasers using beam shaping elements either at the laser or the fiber facet, thereby demonstrating coupling losses down to 0.6 dB (coupling efficiencies η of up to 88 %). In a second set of experiments, we further show that *in situ* printing of curved mirror surfaces for simultaneously defining beam shape and propagation direction opens up vast design freedom for optical assemblies by allowing to flexibly combine surface-emitting and edge-emitting devices in compact arrangements. A third set of experiments is finally dedicated to relaxing alignment tolerances by using beam expanders on both device facets. We demonstrate highly efficient coupling of an edge-emitting laser diode to an SMF with relaxed 1 dB alignment tolerances of more than $\pm$ 5 µm in all directions along with coupling losses of less than 0.8 dB. The same laser is also coupled to a passive chip carrying TriPleX [50] waveguides, thereby achieving alignment tolerances of approximately $\pm$ 4.3 µm and coupling losses of 2.5 dB. Moreover, we demonstrate two types of multi-lens beam expanders with either compact dimensions or very low reflectivity. Our experiments represent the first demonstration of low-loss single-mode coupling to optical chips using *in situ* printing of beam-shaping elements and lead to tolerances that can be met by passive alignment techniques [5], [6]. The concept can be readily applied to a wide variety of optical chips and fibers, does not require any delicate facet preparation or polishing, and renders bulky on-chip mode converters unnecessary. We expect that our approach has the potential to fundamentally change performance and economics of hybrid photonic systems.

4.2 Concept, Design, and Fabrication

The concept of a hybrid photonic multi-chip assembly is illustrated in Figure 4.1. The assembly combines the distinct advantages of different photonic integration platforms: Lasers on direct-bandgap InP substrates are used as optical sources to deliver light to a silicon photonic (SiP) chip. The SiP is connected to the outside world via an array of single-mode fibers. Within the assembly, chip-chip and fiber-chip coupling is accomplished by beam-shaping elements, which are fabricated *in situ* at the facets of the associated optical components using 3D two-photon lithography. Details about simulation and fabrication are to be found in the Methods Section, Appendix A.1. The beam-shaping elements can be fabricated with high reproducibility, leading to coupling efficiency variations of well below 0.1 dB, see Table A.3 of Appendix A. Inset (i) shows a microscope image of a freeform lens printed to the facet of an edge-emitting laser. By exploiting high-resolution machine vision techniques, the beam-shaping elements can be aligned to the respective waveguides with a precision of better than 100 nm. This capability, along with the virtually unlimited design freedom of printed freeform structures, allows to precisely match the vastly different mode field profiles of the various components and hence to achieve low-loss coupling. Printed reflective elements with precisely defined curved mirror surfaces allow to flexibly match the propagation directions of optical beams, thereby interfacing, e.g., edge-emitting lasers to grating couplers on the chip surface, see Inset (ii). In this assembly, alignment tolerances can be greatly relaxed by transforming small mode fields at the device facets into collimated beams with large diameters, Inset (iii). This allows assembly of multi-chip systems with relaxed alignment tolerances of ± 5 µm or above, such that high-throughput passive alignment techniques can be used.

In our experiments, we explore and demonstrate a toolbox of essential beam-shaping elements that can be used as universal building blocks for hybrid multi-chip systems. The elements are illustrated in Figure 2 and in the associated insets. The corresponding scanning electron microscope (SEM) images of printed elements are depicted in Figure 4.2 (a) to (f). The beam shaping elements can be realized as freeform lenses having a single refractive surface, Figure 4.2(A,a) and (C,c), or as reflecting elements exploiting freeform mirror surfaces, Figure

4.2(B,b) and (D,d). In addition, more complex structures are possible, comprising, e.g., combinations of concave and convex lenses for expanding beam diameters, Figure 4.2(E,e), or high-performance multi-lens assemblies, Figure 4.2(F,f). The beam-shaping elements can be designed for operation in air or in a low-index cladding material, which reduces reflection and protects the optical surfaces from environmental influences. Note that the cladding material also reduces the refractive power of an individual optical interface, which must be compensated by using a multitude of cascaded surfaces in a multi-lens assembly, Figure 4.2(F,f), see also Figure A4. Details of the fabrication process can be found in the Methods Section, Appendix A.1. By an appropriate choice of lithography parameters, surfaces with optical quality and a root-mean-square roughness of 37 nm are attained, which can be further decreased using adapted writing strategies, see Figure A.1. In all our experiments, we use the commercially available photoresist IP-Dip. We measured the absorption of the liquid and solid photoresist in a wavelength range from 250 nm to 2500 nm, Figure A5 for details. For a typical device length of 250 µm, we find a negligible absorption loss of 0.13 dB in a wavelength range from 500 nm to 1610 nm. We checked that a printed lens of 60 µm length withstands high powers up to 3 W and maintains constant coupling efficiency over an optical bandwidth of more than 100 nm, see the Methods Section Appendix A.1 for more details.

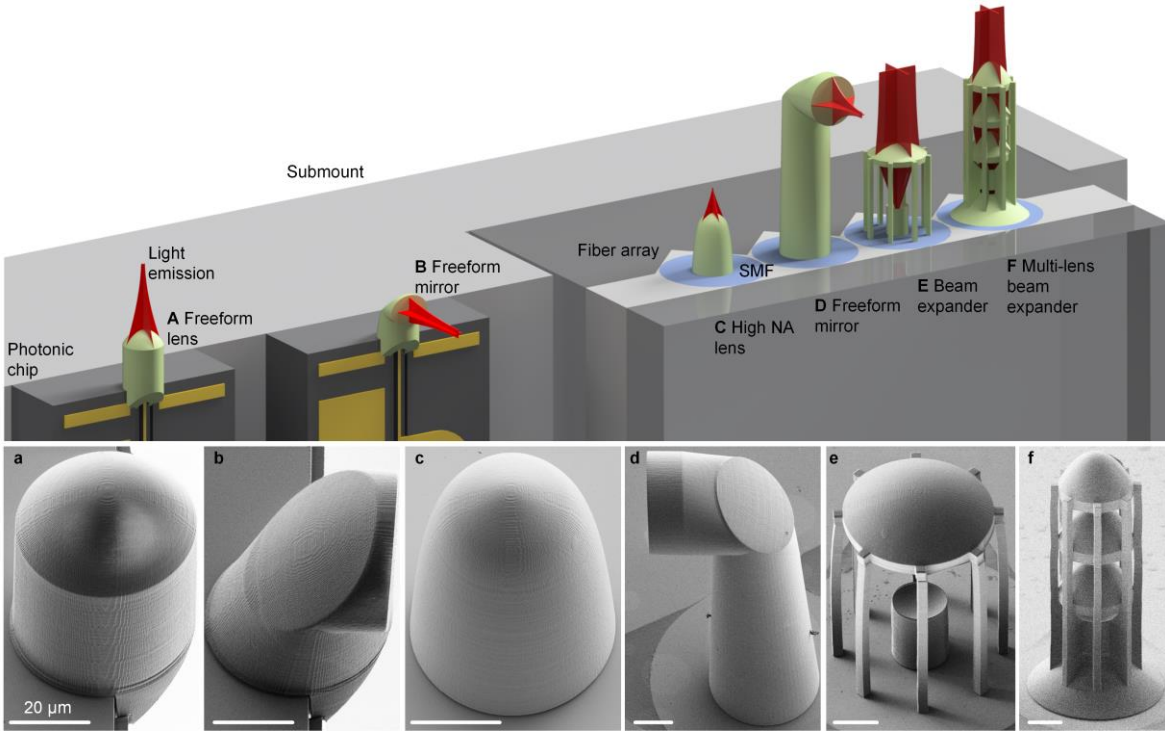

Figure 4.2: Artist's view (A … F) and experimental realizations (subfigures a … f) of various beam-shaping elements that can be used as universal building blocks for hybrid photonic multi-chip systems. **A**,**a**, Freeform lens and **B,b**, total internal reflection mirror printed to the facet of an edge-emitting laser; C,c, Freeform lens with high numerical aperture (NA), **D,d**, total internal reflection mirror for beam deflection, all printed to a the facet of a SMF to couple light from an surface-emitting or edge-emitting lasers. **E,e,** Beam expander, **F,f,** multi-lens optics featuring nine refractive surfaces, all designed for relaxing alignment tolerances of the assembly process.

4.3 Experimental Verification and Discussion

The basic toolbox of beam-shaping elements contains three essential building blocks: Facet-attached lenses for mode field adaption in edge-coupled interfaces, free-form mirrors that allow combining surface and edge-emitting devices in compact arrangements, as well as beam expanders that relax positioning tolerances in the assembly process. In the following, we describe our experimental validation of these structures.

4.3.1 Coupling experiments with facet-attached lenses.

In a first set of experiments, we demonstrate coupling of edge-emitting distributed feedback (DFB) lasers to SMF. For such assemblies, beam-shaping elements can be printed either to the laser or the SMF facet, see Figure 4.3(a,d). In both cases, we determined the coupling efficiency as well as its sensitivity with respect to misalignment. To this end, we moved the SMF in horizontal (x), vertical (y), and axial (z) direction while measuring the fiber-coupled power, see Figure 4.3(b,c) and (e, f). For beam-shaping lenses attached to the laser facet, the coupling loss amounts to 1.0 dB (η = 80 %) for the optimum position of the fiber. This is close to the theoretical optimum of 0.6 dB that can be expected for this configuration; see Appendix A.1 for details of the simulation and the measurement techniques. An SEM image of a printed lens on a laser facet is shown in Figure 4.2(a). Facet-attached beam-shaping lenses are particularly well suited for coupling to ultra-small mode field diameters by exploiting the principle of solid-immersion lenses, which allow the reduction of beam divergence by the higher refractive index of the lens medium. Still, the alignment tolerances are dictated by the rather large mode field diameter (MFD) of the SMF and the associated beam divergence. In our experiment, we find a horizontal and vertical 1 dB positioning tolerance of ± 1.9 µm, little below the simulated tolerance of ± 2.4 µm, indicated by the dashed line in Figure 4.3(b). In axial direction, the 1 dB positioning tolerance amounts to ± 25 µm. This result is on par with lens structures obtained by highly complex laboratory-scale ion beam milling techniques [102], which are not suited for industrial production.

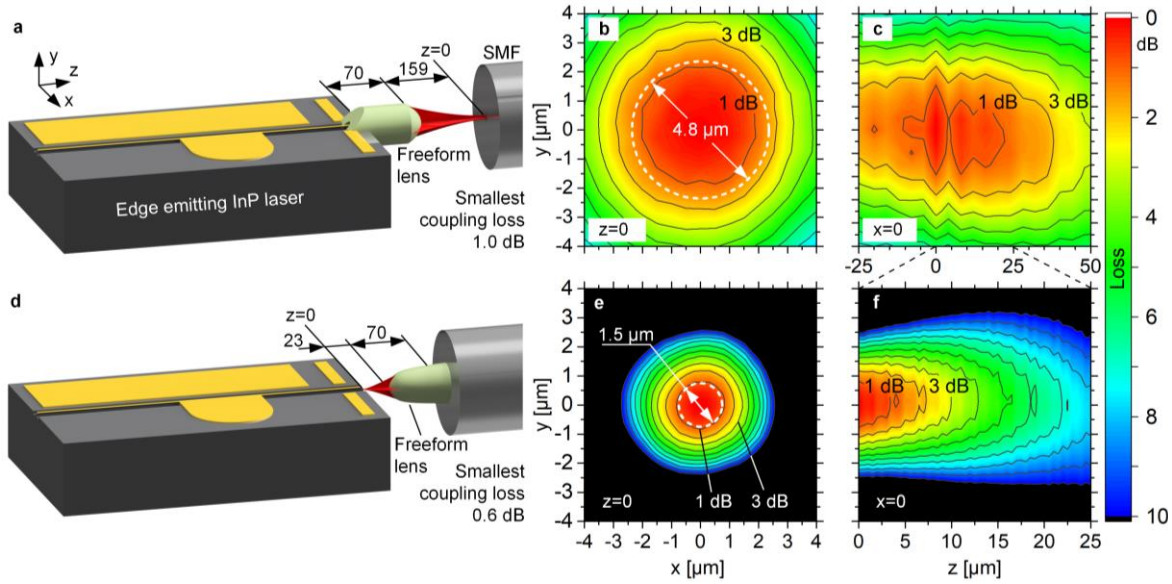

Figure 4.3: Coupling of edge-emitting distributed feedback (DFB) lasers to single-mode fibers (SMF). Beam-shaping lenses are printed either on the laser facet or the SMF. All dimensions are indicated in µm. The 0 dB-level of the contour plots (b), (c), I, (f) correspond to the smallest coupling loss of 1.0 dB or 0.6 dB indicated in the corresponding subfigure (a) and (d). Simulated 1 dB coupling losses are indicated by dashed circles, while the colored contour plots, labeled with the coupling loss, represent measured data. **A,** Freeform lens printed at the facet of a laser. The coordinate system is chosen such that optimum alignment of the fiber corresponds to the position (*x*,*y*,*z*) = (0,0,0), where a minimum coupling loss of 1.0 dB is measured. **B,** Increase of coupling losses relative to optimum alignment for lateral translation in the (x,y)-direction. **C,** Increase of coupling loss relative to optimum alignment for translation in the (y,z)-direction. **D,** Freeform lens printed at the facet of the SMF. The position (*x*,*y*,*z*) = (0,0,0) refers again to the point of best coupling with 0.6 dB loss. **E,** Contour plot of additional coupling loss when moving the fiber in (x,y)-direction. **F,** Contour plot of coupling when moving the fiber in (y,z)-direction.

For beam-shaping lenses attached to the fiber facet, Figure 4.3(d), positioning tolerances are dictated by the smaller MFD of the beam emerging from the laser facet. The minimum coupling losses amount to 0.6 dB (η = 88 %) for optimum alignment, which is in fair agreement to the theoretical optimum of 0.2 dB dictated by Fresnel reflections, see Methods for details. In agreement with simulations, we find a 1-dB-tolerance of ± 0.7 µm for movements in x- or y-direction, indicated by the dashed line in Figure 4.3€. In z-direction, the 1 dB tolerance amounts to 5.8 µm and was only measured in the direction of increasing distance between the fiber and chip to avoid the risk of damaging the laser facet.

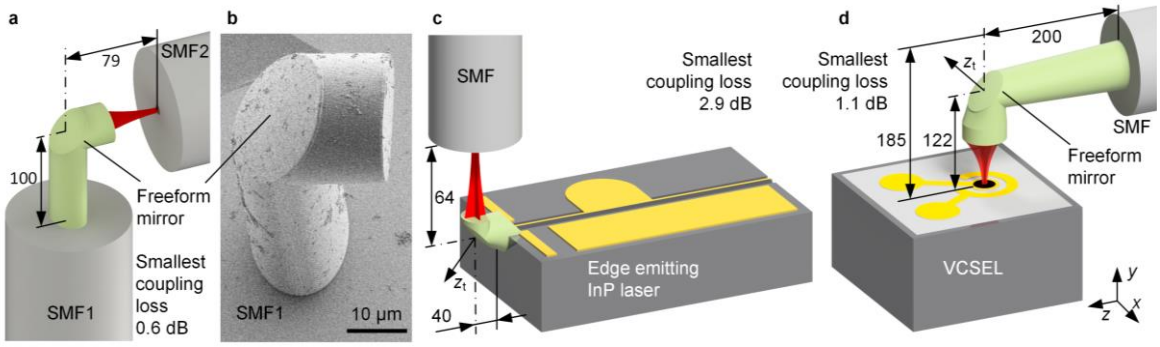

Figure 4.4: Coupling experiments of optical components equipped with freeform mirrors. All indicated coupling losses represent measured data. **A** Model system combining a freeform mirror on the facet of a single-mode fiber (SMF) designed for coupling couple into a second SMF. Coupling losses as low as 0.6 dB are achieved. **B** Electron-microscopy image corresponding printed beam-shaping element. **C** Freeform mirror on the device facet of an edge-emitting laser designed to couple in a single-mode fiber (SMF), see Figure 3.2(b,B) for the corresponding realizations of the beam-shaping element. In the experiment, we measure coupling losses of 2.9 dB; see Methods in Appendix A.1 for details. **D** Coupling from a vertical-cavity surface-emitting laser (VCSEL) to an SMF with a freeform mirror fabricated on the SMF-facet, Figure 3.2(d,D). This approach allows to considerably reduce the assembly height to less than 200 µm.

The demonstrated coupling efficiency is better than the 80 % efficiency achieved with best-in-class lensed fibers [85]. Unlike conventional lensed fibers realized by melting or grinding [85], [88], our approach is also applicable to a wide range of fiber-optic assemblies, including also fiber arrays. An SEM image of a printed high-NA lens on an SMF facet is shown in Figure 4.2(e).

4.3.2 Compact Assemblies with Facet-Attached Freeform Mirrors

A second set of experiments is dedicated to facet-attached freeform mirrors with curved surfaces that simultaneously adapt the mode profile and the propagation direction of light. This allows to flexibly combine edge-coupled and surface-coupled devices without incurring large form factors of the overall assembly. Examples comprise, e.g., coupling of vertical-cavity surface-emitting lasers (VCSEL) to optical fibers that are mounted with their axis parallel to the chip surface, or combinations of edge-emitting III-V lasers with surface-emitting grating couplers of SiP circuits, Figure 4.1(ii). Printed beam-shaping mirrors

may be attached to laser facets, see Figure 4.2(B,b), or to fiber end faces, see Figure 4.2(D,d). We use 3D-printed total internal reflection (TIR) freeform mirrors designed to simultaneously focus and redirect the edge-emitted light into the desired direction. The viability of TIR mirrors is first tested by coupling of two SMF over an angle of 90°, see Figure 4.4(a). In this experiment, we measure losses as low as 0.6 dB (η = 87 %). An SEM image of the TIR mirror element is shown in Figure 4.4(b). This approach was then transferred to fiber-chip coupling, Figure 4.4(c) and (d). For freeform mirror elements printed to the laser facet, Figure 4.4(c), we demonstrate coupling losses of 2.9 dB (η =51 %) compared to the total power emitted by the laser before attaching the beam-shaping element. This loss is mainly caused by the large divergence of the beam emerging from the laser facet, which leads to incomplete TIR at the mirror surface; see Methods in Appendix B for details. This can be overcome by optimized single TIR surfaces, possibly in combination with refractive surfaces for beam shaping, by cascaded TIR surfaces, by photoresist materials with higher refractive index, or by reflective coatings. Nevertheless, the demonstrated coupling losses are already now significantly lower than those obtained for similar structures such as horizontal-cavity surface-emitting lasers [103] (HCSEL) that may be complemented by monolithically integrated lenses [104] to reduce laser-to-fiber coupling losses to 4.9 dB. Alternatively, mirror elements can be attached to the facet of an SMF, e.g., for coupling of light to and from a VCSEL, see Figure 4.4(d) for the concept and Figure 4.2(d) for a fabricated device. With this approach, we could achieve coupling losses of 1.1 dB (η = 78 %). This is better than typical coupling losses of packaged VCSEL [105], for which values of 3 dB have been reported. In addition, our approach allows to interface low-cost surface-coupled lasers or photodetectors to SMF arrays while maintaining compact and flat form factors. The concept can be transferred to grating-coupler interfaces of SiP circuits and should be able to outperform angle-polished fiber arrays [83], for which coupling efficiencies of 4.5 dB have been demonstrated. Moreover, facet-attached freeform mirrors lend themselves to connecting edge-emitting lasers to grating couplers [5], thereby replacing rather complex micro-optical bench (MOB) assemblies of ball lenses and micro-prisms that are currently used in commercial silicon photonic products [106].

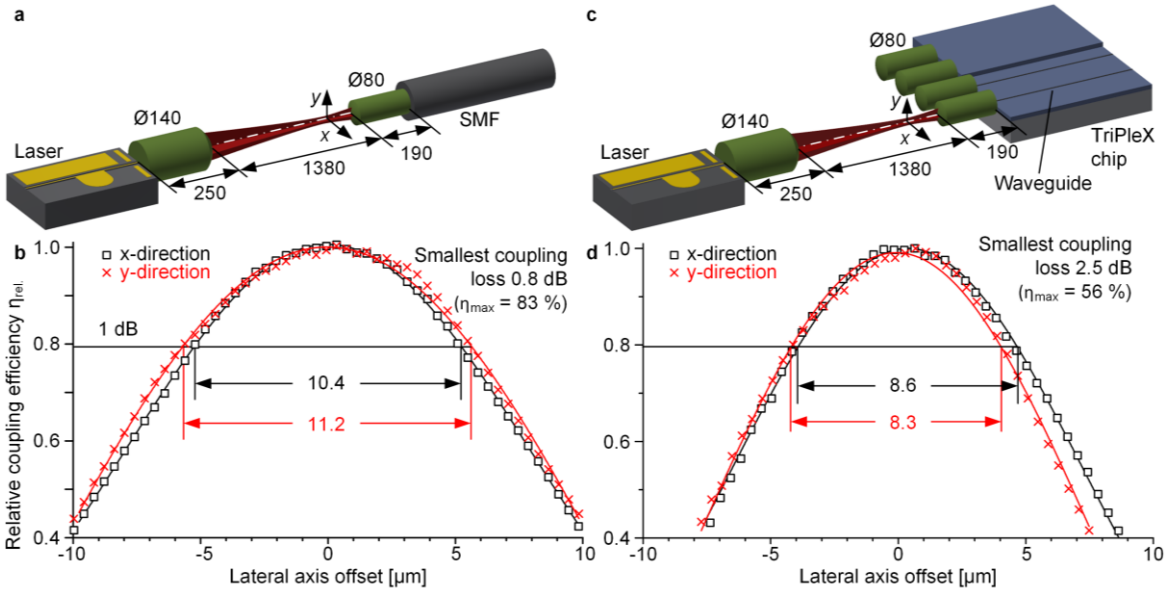

Figure 4.5: Coupling experiments using beam expanders on lasers and waveguides. All geometrical dimensions are measured in µm. The relative coupling efficiency η_{rel} is referred to the maximum efficiency η_{max} (smallest coupling loss) for perfect position and tilt alignment. Measured data and fitted Gaussians (solid lines) are for a lateral offset of the beam axes in x-direction (black, zero y-offset) and y-direction (red, zero x-offset), respectively. **A**, Setup for coupling a laser to a single-mode fiber (SMF). **B**, Decrease of coupling efficiency relative to optimum alignment for a lateral axis offset in (x,y)-direction. The maximum efficiency is η = 83 % (smallest coupling loss 0.8 dB). The measured 1 dB lateral alignment tolerance amounts to ± 5.2 µm (± 5.6 µm) in the x-direction (y-direction), which is in good agreement with a 1 dB offset tolerance of ± 6.0 µm. These tolerances can be met with high-throughput passive alignment techniques. **C**, Setup for coupling a laser to a single-mode waveguide on a TriPleX chip. **D**, Decrease of coupling efficiency relative to optimum alignment for an axial offset in (x,y)-direction. Maximum efficiency is η = 56 % (smallest coupling loss 2.5 dB). The measured 1 dB lateral alignment tolerances are slightly reduced and amount to ± 4.3 µm (± 4.2 µm) in the x-direction (y-direction), which is still amenable to passive alignment.

4.3.3 Coupling Experiments with Facet-Attached Optical Beam-Expanders

The first two sets of experiments relied on single beam-shaping elements. In these cases, the alignment tolerance is inherently dictated by the MFD of the component, which is not equipped with a beam-shaping element. To relax tolerances to a level suitable for passive alignment, beam shaping elements on both

device facets can be used to expand and refocus the beam. This is demonstrated in a third set of experiments by fabricating lenses on the facets of edge-emitting lasers, single-mode fibers (SMF), and so-called TriPleX waveguides, which exploit a combination of silicon nitride and silicon oxide [50], see Figure 4.5. The beam expansion allows trading transverse alignment tolerances in *x*, *y*, and *z*-direction for tilt tolerances of the optical axes, which are generally easier to meet [59]. We perform an experiment both for laser-to-SMF coupling and for laser-to-TriPleX chip coupling, see Figure 4.5. For the laser, the native MFD amounts to 3 µm, measured at the device facet, and a 250 µm-long lens is used to expand the mode field to a Gaussian waist with an MFD of 25 µm in a distance of 1.3 mm from the apex of the lens. For the TriPleX chip (SMF), the native MFD is specified to 11 µm (10 µm), and 190 µm-long lenses are used to generate 25 µm Gaussian beam waists. For the laser-to-SMF interface, the simulated 1 dB lateral alignment tolerance of the beam axes in the plane of the 25 µm mode field diameter amounts to ± 6.0 µm. This is confirmed by the experiments, leading to tolerances of ± 5.2 µm in *x*-direction (black) and of ± 5.6 µm in *y*-direction (red), see Figure 4.5(a). Details on the experiment can be found in Appendix A.1. For perfect position and tilt alignment, we demonstrate a coupling efficiency of $\eta = 83$ % (coupling loss 0.8 dB). To the best of our knowledge, our results represent the highest positioning tolerance so far obtained for a fiber-chip interface with a sub-1 dB insertion loss. The tolerance is within the limits of passive alignment [5], [6] and has the potential to revolutionize high-throughput assembly of fiber-chip interfaces. For the laser-to-TriPleX chip coupling, we measure a coupling efficiency of $\eta = 56$ % (coupling loss 2.5 dB) for perfect alignment, and the measured 1 dB axis alignment tolerances amount to ± 4.3 µm in *x*-direction (black) and to ± 4.2 µm in *y*-direction (red), see Figure 4.5(d). The relatively high residual loss of the coupling interface is attributed to a deviation of the mode field of the TriPleX chip from its specified value of 11 µm. This is supported by an experiment where we butt-coupled an SMF to ten nominally identical TriPleX waveguides on the same chip, all designed to produce a circular MFD with a diameter of 11 µm at the device facet. The best total loss amounts to approximately 2 dB per interface, which is likely caused by rough device facets; see Appendix A.7 for details. We expect that better facet preparation can reduce the coupling losses to less than

1 dB and increase the alignment tolerances to more than ± 5 µm, as expected from simulations. Based on the mode field diameter of 25 µm, we estimate 1 dB axis tilt alignment tolerances of ± 1°. These requirements are well compatible with passive alignment techniques [5], [6], [59].

The beam expanders shown in Figure 4.6 consists of one lens directly attached to laser and fiber. In this case, the length of the lens is dictated by the beam divergence within the fiber and by the fact that the beam diameter at the refracting lens surface must be larger than the targeted MFD in the beam waist. This leads to relatively large lenses with typical lengths of 150 µm to 250 µm; see Appendix A.1 for details. To fabricate shorter beam expanders, we combine a concave diverging lens with a plano-convex focusing lens see Figure 4.6(E,e) for the concept. As a demonstrator, we couple a pair of SMF, see Figure 4.6(a). We achieve coupling losses of 1.9 dB for perfect position and tilt alignment of the fibers; see Appendix A.1 for details on the measurement technique. The 1 dB transverse alignment tolerances amount to ± 5.5 µm in the transverse and ± 220 µm in the axial direction, see Figure 4.6(b,c), in agreement with simulations, white dashed circle. Fresnel reflection at the six air-polymer interfaces accounts for 1.3 dB loss. The remaining 0.6 dB are attributed to imperfect fabrication and surface roughness, which may be mitigated by refined writing strategies.

The demonstrated optical systems all rely on high index contrast optics operated in air, causing Fresnel reflections that lead to optical loss and may cause optical feedback in active components such as lasers. In general, reflection at a single dielectric interface can be reduced by using a smaller refractive index contrast. This, however, also reduces the refractive power and needs to be compensated by cascading a multitude of interfaces. Multi-lens assemblies with low index contrast can be used to overcome the problem of reflection losses: In Appendix A.5, we show that, for a given refractive power of the overall lens system, the total Fresnel losses can be reduced by increasing the number of lens surfaces while decreasing the index contrast at each surface. We refer to such assemblies as “low index-contrast micro-optical systems” (LIMOS). An implementation of the LIMOS concept is shown in Figure 4.6(d), where a pair of multi-lens beam expanders of refractive index $n = 1.52$ is embedded into a cladding with a

refractive index of n0 = 1.47. An SEM image of a LIMOS beam expander is shown in Figure 4.6(f).

For experimental verification, the structure is embedded into an index-matching liquid that emulates the cladding. The simulated fiber-to-fiber coupling loss of the LIMOS-expander amounts to 0.1 dB (η = 98 %), including reflection. In the experiment, this loss increases to 1.0 dB (η = 80 %); see Appendix A for details about the measurement. The difference of calculated and measured losses is attributed to fabrication inaccuracy. In particular, a tilt of 0.5° of the expander axis with respect to the fiber axis causes an additional loss of about 0.6 dB. In the future, this can be mitigated by improved tilt detection and correction. Nevertheless, the experimentally demonstrated coupling loss of the 18-surface LIMOS expander is smaller than the 1.3 dB that can be theoretically achieved by a comparable six-surface structure in air. The LIMOS approach addresses one of the most stringent challenges of printed micro-optics: Since optical surfaces in advanced printed 3D assemblies are not directly accessible, anti-reflection coating, e.g., by gas-phase deposition, is not possible. Sub-wavelength surface structures are effective in reducing reflection [107] but produce scattering loss. The LIMOS concept overcomes these

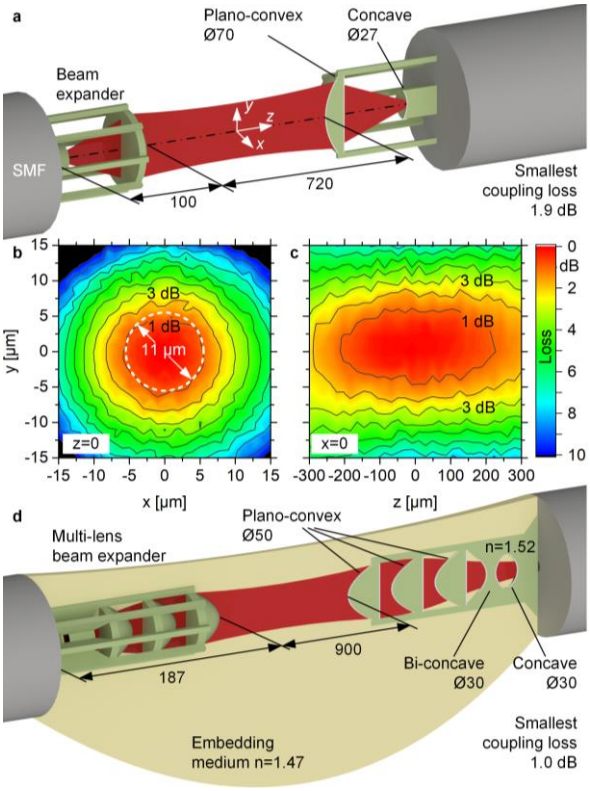

Figure 4.6: Coupling experiments using expanders for relaxing alignment tolerances. As a well-defined model system, we use single-mode fibers (SMF). All geometrical dimensions are measured in µm. **a**, Concept for the coupling experiment using a pair of two-lens beam expanders in air. **B**, Increase of coupling losses relative to optimum alignment for translation in the (x,y)-direction. A dashed circle shows simulated 1dB coupling tolerances. **C**, Increase of coupling losses relative to optimum alignment for translation in the in (y,z)-direction. **D**, Coupling experiment demonstrating a low index-contrast micro-optical system (LIMOS) that allows to significantly reduce reflection losses in printed multi-lens assemblies.

challenges and we expect that this approach is applicable to a wide range of printed micro-lenses for both imaging and beam-shaping applications. As a side effect, the low-index cladding acts as a protective layer against environmental influences.

4.3.4 Summary and Outlook

We have demonstrated that 3D freeform-optical elements printed to device facets can be used for highly efficient and position-tolerant coupling. We explore and demonstrate a toolbox of essential beam-shaping elements required to build hybrid optical assemblies: Freeform lenses, freeform mirrors and multi-lens beam expanders that reduced tolerances such that passive alignment can be used. In a first set of experiments, we demonstrate single freeform lenses printed either to laser or to fiber facets, leading to coupling losses of down to 0.6 dB. A second set of experiments is dedicated to freeform total-internal reflection (TIR) mirrors that allow combining surface- and edge-emitting optical components in compact assemblies. We demonstrate the viability of the approach by coupling vertical-cavity surface-emitting lasers (VCSEL) to single-mode fibers (SMF) using printed freeform mirrors on either the laser or the SMF end face. This leads to coupling losses of down to 1.1 dB. A third set of experiments demonstrates that beam expanders on both facets of a coupling interface allow to considerably relax transverse positioning tolerances. In particular, we show coupling of edge-emitting lasers to SMF coupling and so passive TriPleX chips, with coupling losses of 0.8 dB and 2.5 dB respectively with 1 dB position tolerances of approximately ± 5 µm, amenable to passive alignment [5], [6] Using a pair of SMF as a well-defined model system, we demonstrate coupling losses of 1.9 dB, for a compact two-lens beam expander mainly limited by Fresnel reflection. The lateral 1 dB alignment tolerances amount to ± 5.5 µm. We also demonstrate that facet-attached beam-shaping elements can be fabricated with high reproducibility, leading to coupling efficiency variations of less than ± 0.1 dB, see Table A.3. The approach can be transferred to a wide variety of edge-emitting and surface-emitting devices and could pave the path towards large-scale passive alignment of optical components. For reducing the Fresnel reflection in multi-lens systems, we introduce the concept of low index-contrast micro-optical systems (LIMOS). The viability of the approach is shown by

coupling a pair of SMF via a pair of LIMOS beam expanders that comprise a total of 18 lens surfaces. This significantly reduced coupling loss to 1.0 dB, which is even below the minimum losses that can be theoretically achieved by lenses operated in air. We expect that the LIMOS technology enables new types of printed multi-lens systems with almost no reflection loss.

[end of paper [J3]*]*

5 Printed Freeform Lens Arrays on Multi-Core Fibers for Highly Efficient Coupling in Astrophotonic Systems

Terrestrial telescopes require advanced adaptive optics to compensate for atmospheric turbulence. This is traditionally done using a wave front sensor that requires extracting light from the signal that is to be analysed. This chapter introduces an approach of a wave front sensor that is integrated on a fiber facet and does not reduce the coupling efficiency of a not distorted signal.

The following chapter is taken from a publication [J4] in Optics Express. To fit the structure and layout, it was adapted accordingly. A description of the author's contribution is provided in the list of journal publications.

Author contributions

The author of this thesis has developed the concept of wave front sensing using 3D-printed micro-lenses together with Robert Harris. The author of this thesis and R. J. Harris did equally contribute to this publication. The author of this thesis simulated, developed processes, fabricated and characterized micro-lenses on multi-core fibers with the help of R. J. Harris, M. Blaicher, M. K. Corrigan, T. M. Morris. The author of this thesis wrote the manuscript, including data evaluation and figures together with R. J. Harris, W. Freude, A. Quirrenbach and C. Koos.

[start of paper [J4]]

Printed freeform lens arrays on multi-core fibers for highly efficient coupling in astrophotonic systems

DOI: https://doi.org/10.1364/OE.25.018288

Philipp-Immanuel Dietrich,[1,2,3,†] Robert J. Harris,[4,†] Matthias Blaicher,[1,2] Mark K. Corrigan,[5] Tim M. Morris,[5] Wolfgang Freude,[2] Andreas Quirrenbach,[4] and Christian Koos[1,2,3*]

[1] Institute of Microstructure Technology (IMT), Karlsruhe Institute of Technology (KIT), Hermann-von-Helmholtz-Platz 1,76344 Eggenstein-Leopoldshafen, Germany

[2] Institute of Photonics and Quantum Electronics (IPQ), Karlsruhe Institute of Technology (KIT), Engesserstr. 5, 76131 Karlsruhe

[3] Vanguard Photonics GmbH, Hermann-von-Helmholtz-Platz 1,76344 Eggenstein-Leopoldshafen, 76227 Karlsruhe

[4] Zentrum für Astronomie der Universität Heidelberg, Landessternwarte Königstuhl, Königstuhl 12, 69117 Heidelberg

B Durham University, Centre for Advanced Instrumentation, Department of Physics, South Road, Durham, UK, DH1 3LE

* christian.koos@kit.edu

† P.-I. D. and R. J. H. contributed equally.

Abstract: Coupling of light into multi-core fibers (MCF) for spatially resolved spectroscopy is of great importance to astronomical instrumentation. To achieve high coupling efficiency along with fill-fraction close to unity, micro-optical elements are required to concentrate the incoming light to the individual cores of the MCF. In this paper, we demonstrate facet-attached lens arrays (LA) fabricated by two-photon polymerization. The LA provides close to 100 % fill-fraction along with efficiencies of up to 73 % (down to 1.4 dB loss) for coupling of light from free-space into an MCF core. We show the viability of the concept for astrophotonic applications by integrating an MCF-LA assembly in an adaptive-optics test bed and by assessing its performance as a tip/tilt sensor.

5.1 Introduction

Optimizing free-space coupling efficiency of light into fibers for spectroscopy is highly important in astro-photonics due to the low light levels involved. To achieve the required alignment accuracy, the system needs to be very stable. However, this is challenging, as large telescopes are constantly exposed to changing temperatures and gravity vectors. Conventionally, larger multimode fibers are used, relaxing these constraints somewhat. However, with spectrographs aiming for greater precision than ever before, instruments using smaller single-mode fibers (SMF) have been proposed [66], [108]. This allows the spectrographs to be reduced in size and make use of single-mode devices such as

fiber Bragg gratings (FBG) for suppression of hydroxyl emission lines [67], [109]. Further, an SMF mitigates the problem of modal noise [65], [66].

Due to diffraction effects from the telescope aperture, approximately 80 % of the light can be coupled into an SMF [110]. However, coupling to an SMF is particularly susceptible to the effect of optical turbulence in the atmosphere, which degrades the beam quality and reduces the coupling efficiency to unacceptable levels. To improve this coupling into the fiber, adaptive optics (AO) systems [111] can be used. Further increases in coupling can be achieved using techniques such as point spread function (PSF) apodization, jitter control [112], linear quadratic Gaussian control (LQG) and feed-forward systems [111].

Together, all of these techniques show that coupling into SM fibers could be viable in future instrumentation. Experiments using turbulence simulators reach 65 %[112] coupling, and on-sky experiments show (10…25) % [2]. However, this is still below the optimal coupling due to remaining residual aberrations and structural vibrations, mainly in the form of tip/tilt [113].

Ideally, any system would sense tip/tilt at the coupling point where the fiber feeds the spectrograph and would not consume any light that could be fed to the spectrograph. This demand can be realized by highly integrated integral field unit (IFU) devices. An IFU has many spatial pixels (spaxels) sampling the focal plane of the telescope. When connected to a spectrograph, both spatial position and wavelength can be resolved. To use an IFU as a tip/tilt sensor, light from a central spaxel is coupled into the science spectrograph, while adjacent spaxels are used to monitor the position of the beam. Fiber-based IFUs stand out due to their compactness and flexibility. They can be realized with fiber bundles [114], hexabundles [115], or multi-core fibers. The achievable performance, however, is inherently limited by a trade-off of fill-fraction *versus* cross-talk between the fibers.

In this paper, we show that the aforementioned challenges can be overcome by lens arrays (LA) that are directly attached to the facet of an MCF. The LA are fabricated *in situ* by direct-write two-photon lithography with sub-µm precision. We demonstrate fill-fraction of close to 100 % along with efficiencies of up to 73 % (1.4 dB loss) for coupling of light from free-space into a single-mode

MCF core. We show that this IFU-style device can be used as a tip/tilt sensor for measuring the beam displacement at the facet of a single-mode MCF. The surrounding fiber cores supply a feedback signal for the correction of residual tip/tilt movement in the system. We demonstrate the viability of our MCF-LA in an adaptive optics simulator. To the best of our knowledge, this is the first demonstration of MCFs with lenses attached to individual fiber cores.

5.2 Concept, Design, and Fabrication

The concept of the facet-attached LA is illustrated in Figure 5.1(a). It comprises seven 3D freeform lenses fabricated with sub-µm precision on the facet of a seven-core single-mode MCF. The assembly aims at maximizing coupling efficiency of the main signal into the center core, whereas the surrounding cores are used to capture error signals for tip/tilt control. For better illustration of the main path and error signal, the lens array and part of the fiber are cut away. The Inset shows the simulated coupling efficiency to the center core and one adjacent core as a function of radial offset from the center, assuming a Gaussian beam with a waist of 26 µm in diameter on the top surface of the lenses. Figure 5.1(b) shows the 3D topography of the lens array measured with a white-light interferometer. An electron microscope image of a fabricated LA is shown in Figure 5.1(c). The concept builds upon earlier experiments where we used direct-write two-photon lithography to realize facet-attached lenses for improved fiber-chip coupling [C3].

5.2.1 Simulation and Design

The tip/tilt sensor was simulated with the physical-optics module of the commercially available software Zemax [116]. We used a commercially available seven-core fiber [117] with a 1/e²-intensity mode field diameter (MFD) of $2w_0 = 6.1\mu\text{m}$. The datasheet specified a numerical aperture of 0.22 at a wavelength of 1550 nm. Using a Gaussian field approximation for the SMF field, this would correspond to a $(1/10)^2$-intensity width. The numerical aperture for a Gaussian beam at the $1/\text{e}^2$-intensity level would be $A_{N0} = 2\lambda/(2\pi w_0) = 0.16$. The core spacing is 35 µm, and the fiber diameter is 125 µm, see Figure 5.1(a).

This means that cross-coupling between the cores can be neglected. The lens surfaces were described by even polynomials with coefficients up to the sixth order. We optimized the coefficients of the polynomials for maximum coupling of a beam with a 26 µm Gaussian waist at the surface of a single freeform lens into the fiber core. The diameter of the simulated lens was chosen to be 40 µm such that there is a 5 µm overlap between adjacent lenses to achieve a 100 % fill-fraction. The height of the lenses was designed to be 115 µm. The highest simulated coupling efficiency excluding reflection was 98.5 %. We found that 1 % loss can be attributed to clipping of the beam, while 0.5 % loss is due to a residual mode field mismatch. We simulated the coupling efficiency of a single lens with respect to a transverse misalignment of the Gaussian waist, see inset Figure 5.1(a). The 1 dB (79 %) tolerance is ± 7.2 µm, assuming a freeform lens with a 35 µm diameter. We additionally simulate the light coupled into an adjacent fiber core. This signal can be considered a feedback signal that is fed into an adaptive optics system. With a 1 dB position tolerance (79 %) of the center core, the error signal is found to be at 1.6 % of the maximum coupling efficiency.

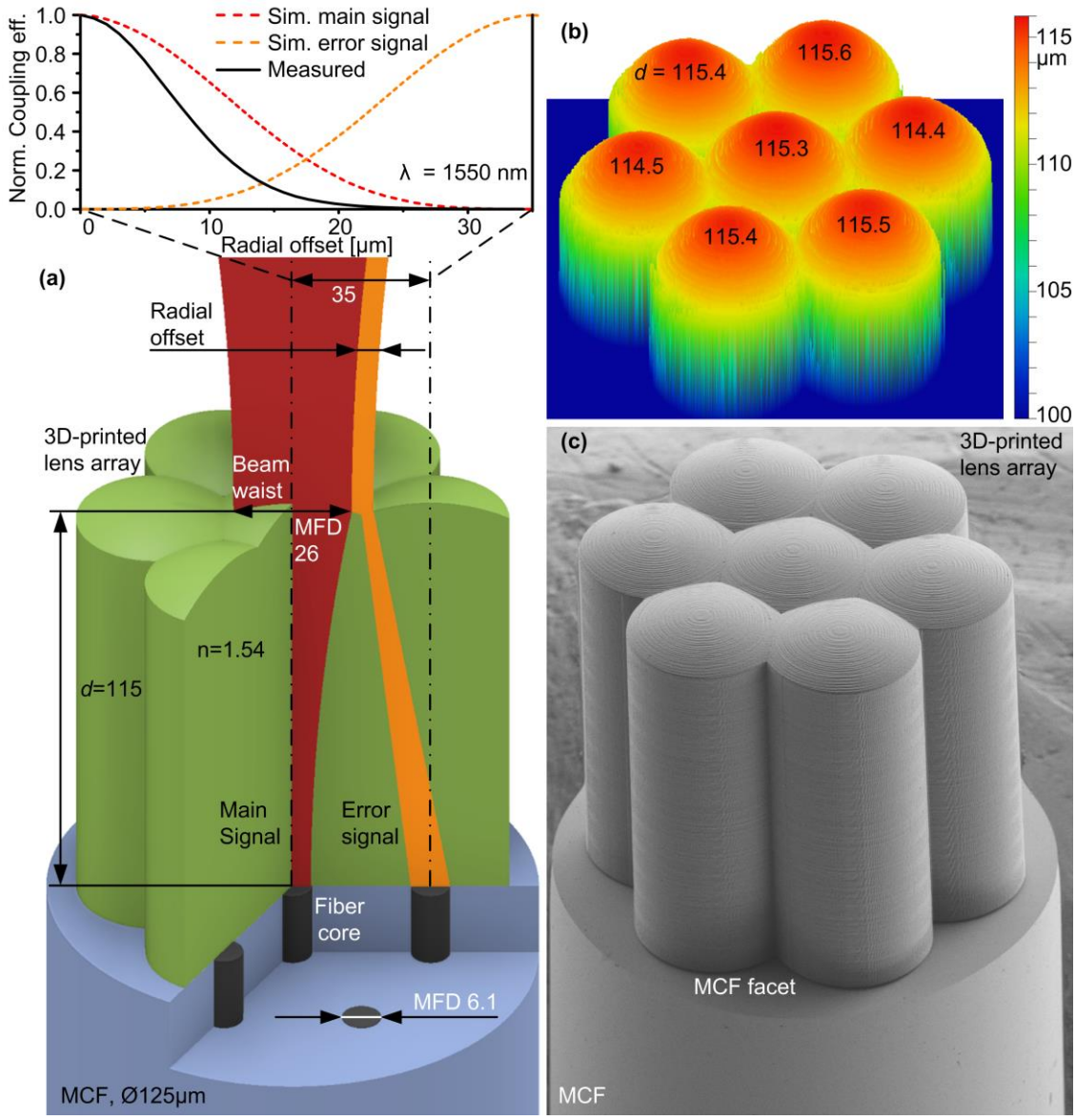

Figure 5.1. 3D freeform lens array fabricated on the facet of a multi-core fiber (MCF). The center core is used to capture the main signal for spectral analysis, whereas the adjacent cores are used to measure error signals for tip/tilt correction. Mechanical dimensions and mode field diameters (MFDs) are indicated in µm. **(a)** 3D model of the MCF and the fabricated lens array. For better illustration of beam path (red) and error signal (orange), the lens array and part of the fiber are cut away. **Inset:** Simulated and measured coupling efficiency of the main signal and of the error signal. Note that due to the available lenses and for avoiding an iris, the MFD of the measured signal was only 21 µm instead of the optimum 26 µm; this explains the discrepancy between simulation and measurement. **(b)** 3D topography of the lens array measured with a white-light interferometer. The maximum distance *d* of the lens surfaces from the MCF facet is indicated. **(c)** Electron microscopy image at a 45° angle of the lens array *in situ* printed on the MCF facet. The fiber has a diameter of 125 µm.

5.2.2 Fabrication by 3D-printing

We used two-photon polymerization of the commercial photoresist IP-Dip [118] for *in situ* printing of the freeform lenses on the facet of a cleaved MCF. We used a commercial device (Nanoscribe Photonic Professional*GT*) with proprietary software for high-precision alignment and writing with high shape fidelity. The 3D-printer was equipped with a scanning mirror and a piezo actuator. We exposed the structure by line-scanning a femtosecond laser with a 100 nm spacing of adjacent exposure lines. The lens array shown in Figure 5.1(a) was fabricated in a single block. Alignment of the individual lenses with respect to the cores was done using machine vision and confocal scanning. A scanning electron microscopy image (SEM) of a fabricated lens array is shown in Figure 5.1(b). A vertically-scanned white-light interferometry image (VSI) is shown in Figure 5.1(c). The height of the lenses was measured from the facet of the SMF. All lenses are within ±500 nm of the designed height of 115 µm, well within acceptable tolerances.

5.3 Characterization and Measurement of Coupling Efficiency

To evaluate the performance of the MCF-LA, the coupling efficiency from a free-space Gaussian beam to the central core was measured. The measurement was performed using a fiber-attached beam expander (Thorlabs TC25FC-1550, MFD = 4.65 mm) with a diffraction-limited lens (Thorlabs AL2550H, f = 50 mm) to produce a Gaussian waist diameter of 21 µm. This is smaller than the MFD the lenses were designed for. However, we avoid using an iris which would result in a mode field with Airy-function intensity distribution and its associated loss. As a reference, we coupled the test focal field into an integrating sphere – the same device that is subsequently used to measure the power coupled captured by the MCF cores. The extra Fresnel reflection loss of 0.16 dB from the plane MCF end was taken into account. The coupling efficiency of the test focal field into the fiber amounted to 73 % (1.4 dB loss). The coupling loss can be partly attributed to Fresnel reflection at the freeform lens (4 %, 0.2 dB) and partly to the mode field mismatch of the test focus with 21 µm instead of

the 26 µm used for the design (2 %, 0.1 dB). The residual coupling loss of (21 %, 1.1 dB) can be attributed to the imperfectly cleaved facet that leads to a slightly angled fabrication of the freeform-lens array. Simulation indicates that a tilt of 3° of the MCF facet normal with respect to the optical axis of the MCF leads to a coupling loss of 1 dB, which approximately corresponds to the measured loss. This can easily be avoided by a better cleaving procedure or by polished fiber facets as in fiber arrays or physical-contact (PC) fiber connectors. To confirm the simulation of the position dependency of the signal coupled into the MCF, see Section 1.1. We show the position-resolved coupling efficiency in the inset of Figure 5.1(a). To avoid coupling of light into several fiber cores, we couple light into one of the outer cores and show the signal decay when moving the test focus away from the center core. We find fair agreement to the simulated data. Note that due to the available lenses and for avoiding an iris, the MFD of the measured signal was only 21 µm instead of the optimum 26 µm; this explains the discrepancy between simulation and measurement.

5.4 Demonstration as a Tip/Tilt Sensor

5.4.1 Adaptive Optics Testbed

In order to assess the potential of the MCF-LA as a tip/tilt sensor, the sensitivity to beam displacement was tested. This was performed using an adaptive optics testbed configured in a similar way to that described in [119], see Figure 5.2. The system is fed by two fibers. The first is a multimode fiber coupled to a 633 nm laser for wave front sensing by a Shack-Hartmann sensor. The second beam is emitted by a single-mode fiber (SMF) which carries light from a 1550 nm laser and is used to simulate the light of an AO system. Both fiber outputs are collimated and pass through an iris located at the pupil plane. To allow the deformable mirror (DM) to have the correct spacing from the iris, the beam is re-collimated by two lenses with longer focal lengths. The light is reflected from a beamsplitter onto the DM. This allows controlling tip, tilt and other low-order aberrations. At a dichroic mirror, the 663 nm light is reflected to a Shack-Hartman sensor to monitor the shape of the DM. We thereby obtain a feedback signal that allows us to control the DM. The 1550 nm light is

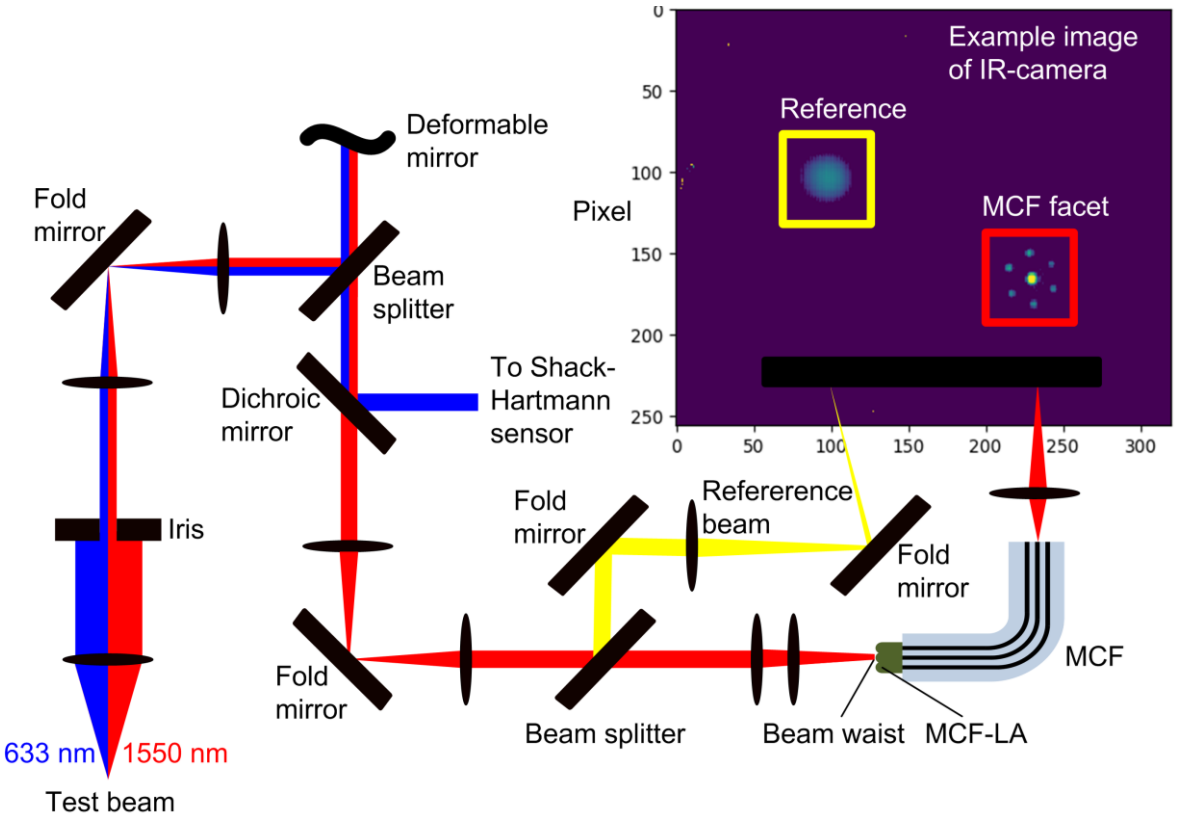

Figure 5.2. Schematic of the beam path used for testing the lens array attached to the multi-core fiber (MCF). The common input beam is shown in red (1550 nm from a single-mode fiber, SMF) and blue (633 nm from a multimode fiber, MMF). The 633nm beam is used for feedback control while the 1550nm beam is focused onto the MCF lens array (MCF-LA). The beam position is scanned using the deformable mirror that is operated with optical feedback from the Shack-Hartmann sensor. The amount of light coupled into individual fiber cores of the MCF can be obtained by observing the rear facet of the MCF with an infrared (IR) camera. To monitor the beam quality, a reference beam (yellow) is split off from the main beam (red).

transmitted to the test section, where a beam splitter and a lens direct 10 % of the light onto an infrared (IR) camera (Xenics-Xeva 1.7 320 InGaAs) while 90 % of the light is focused on the surface of the 3D-printed lenses.

5.4.2 Use as a Tip/Tilt Sensor

The MCF-LA was placed in the adaptive optics testbed, see Section 3.1. A simulated-annealing algorithm was performed [120] to initially adjust the DM for optimum coupling, and the DM was then used to scan the beam waist (see Figure 5.2) across the 3D-printed lenses in order to ascertain the response. To this

end, we imaged the end facet of the fiber with the infrared (IR) camera and calculated the optical power in each individual core. This power output is shown in Figure 4.3 as a function of the test focus position. The position of the individual plots corresponds to the measured fiber core at the output facet. All plots are normalized to the maximum coupling of the central core. The color-coded intensities show that, as expected, the coupling is maximum when the beam waist is positioned at the center of the corresponding micro-lens. For example, the coupling for the central fiber is best when the beam waist is centered on this fiber.

All the lenses show similar responses, with only minor deviations for the outer ones, which we attribute due to loss of image quality as the position of the test beam is scanned away from the axis of the center lens and to inaccuracies in the positioning of the deformable mirror. For application as a tip/tilt sensor, the center fiber can be connected to a spectrometer, while the other lenses generate a beam displacement-dependent error signal that can be used to compensate for residual tip/tilt of the beam.

We find that both the signal of the center core and the error signal are less sensitive to movement than simulated and indicated by lab-based measurements with a test focus, see Figure 5.1(a). This can be attributed to a beam waist, which was larger than the MFD of 26 µm the MCF-LA was designed for. This problem can be mitigated by improved annealing algorithms of the deformable mirror.

Measurements show a displacement of 10 µm corresponds to a decrease of the main signal coupling efficiency to the center core of less than 1 dB. Tilt can hence be detected before there is a significant decay of light coupled into the center core. The relatively large sensed area (red circle) over which light is coupled to the MCF allows for detection of displacements of up to 65 µm from the center core, significantly simplifying the alignment of the MCF.

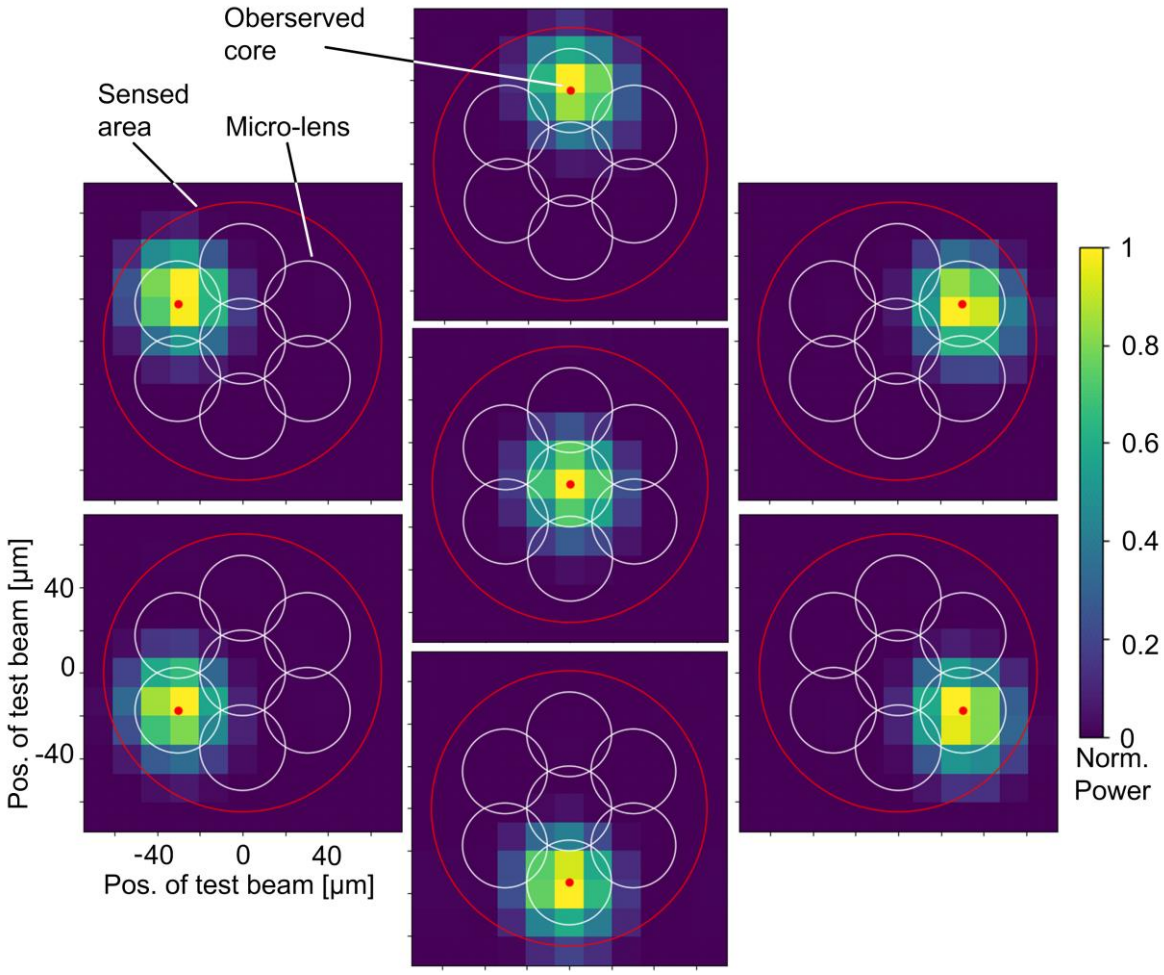

Figure 5.3 Seven plots showing the relative power coupled into of each of the seven single-mode fiber cores as a function of test beam position on the lens array (LA) at the input facet. All plots are on the same scale and normalized to the central core. Yellow corresponds to a maximum coupling to the given core. The red dots represent the positions of the observed core, and the white circles show the position of the micro-lenses. The red circle has a diameter of 130 µm, beyond this circle the light is not coupled into the fiber cores.

5.4.3 Summary and Outlook

We simulated, fabricated and characterized a micro-lens array attached to the facet of a multicore fiber. Our MCF-LA allows highly efficient coupling of a single Gaussian beam to individual single-mode fibers (SMFs) and provides an error signal that can be used as feedback for an adaptive optics system. We show

that small beam displacements create an easily detectable error signal. The maximum coupling efficiency was 73 % (1.4 dB loss). Residual loss was due to an imperfect cleaving of the fiber, which can be corrected in future implementations. Compared to other sensing mechanisms, our approach has the advantage that it allows for highly efficient coupling and sensing of the beam displacement relative to the micro-lens array without external components such as beam splitters. The tip/tilt sensor is hence located at the position of the coupling device itself, and non-common path aberrations or vibrations between sensing and coupling device can be avoided. Our MCF-LA can sense a beam displacement of up to 65 µm. By connecting our MCF to a commercially available MCF-to-SMF fan-out [12], high-speed detectors with SMF pigtails can be used.

Our demonstration also paves the path to innovative multichannel optical devices such as a new generation of integral field units (IFUs) with 100 % fill-fraction and high coupling efficiency. Facet-attached lens arrays are not limited to coupling to single-mode devices. Using a suitable multimode multicore fiber, the concept could be used for devices similar to hexabundles [115]. Our next effort will concentrate on improvements of coupling efficiency, flexibility and ruggedness of the system in order to allow deployment as part of an astronomical instrument. To achieve this, we print lens arrays on standard commercial mountings, e.g., on a fiber coupling ferrule. This increases the flexibility and ruggedness of the system and allows easy integration in an astronomical instrument. In addition, fabrication on a standard polished ferrule will automatically resolve issues with imperfectly cleaved fiber facets.

[end of paper [J4]*]*

6 3D-printed Scanning Probe Microscopes with Integrated Optical Actuation and Read-Out

The following chapter is dedicated to 3D-printing of optomechanical microsystems for SPM. Within this work, the concept of 3D-printed tips and mechanical structures on AFM cantilever was developed and published [J5]. The concept was then expanded to fully functional 3D-printed and optically read-out freeform structures, which are shown in the following chapter. The content is taken from a publication [J2] in *Small*. To fit the structure and layout of this document, it was adapted accordingly. Methods and Supplementary Information associated with the manuscript can be found in Appendix B.

Author contributions

The author of this thesis proposed the concept and discussed with all Co-Authors of SPM measurement with 3D-printed, optically actuated read-out engines for application including AFM and SNOM. The author of this thesis designed, developed processes fabrication and validation of optical engines with the help of M. Trappen, G. Göring and M. Blaicher. The author of this thesis did AFM and SNOM measurements jointly with G. Göring and M. Trappen. The project was supervised by T. Schimmel, H. Hölscher and C. Koos. The author of this thesis supervised M. Trappen. M. Trappen contributed in part to data evaluation, such as evaluating resonance frequency and shape accuracy and thermo-optical simulation. The author of this thesis has written the manuscript's initial version. Discussion and further modification of the manuscript were done together with all co-authors and in particular with H. Hölscher and C. Koos.

[start of paper [J2]]

3D-printed Scanning Probe Microscopes with Integrated Optical Actuation and Read-Out

DOI: https://doi.org/10.1002/smll.201904695

Philipp-Immanuel Dietrich,[*1,2,3†] Gerald Göring,[4,5†] Mareike Trappen,[1,2,†] Matthias Blaicher,[1,2] Wolfgang Freude,[2] Thomas Schimmel,[4,5] Hendrik Hölscher,[1] Christian Koos,[1,2,3]

[2] Institute of Photonics and Quantum Electronics (IPQ), Karlsruhe Institute of Technology (KIT), Engesserstraße 5, 76131 Karlsruhe, Germany.

[3] Vanguard Photonics GmbH, Gablonzer Straße 10, 76185 Karlsruhe, Germany.

[4] Institute of Applied Physics (APH), Karlsruhe Institute of Technology (KIT), Wolfgang-Gaede-Straße 1, 76131 Karlsruhe, Germany.

[5] Institute of Nanotechnology (INT), Karlsruhe Institute of Technology (KIT), Hermann-von-Helmholtz-Platz 1, 76344 Eggenstein-Leopoldshafen, Germany.

[*] Correspondence to: P.-I. Dietrich, p-i.dietrich@kit.edu; C. Koos, christian.koos@kit.edu,.

[†] These authors contributed equally to this work.

Scanning probe microscopy (SPM) is the method of choice for high-resolution imaging of surfaces in science and industry. However, SPM systems are still considered as rather complex and costly scientific instruments, realized by delicate combinations of microscopic cantilevers, nanoscopic tips, and macroscopic read-out units that require high-precision alignment prior to use. Here we demonstrate a concept of ultra-compact SPM engines that combine cantilevers, tips, and a wide variety of actuator and read-out elements into one single monolithic structure. The devices are operated by optical actuation and read-out without manual alignment of individual components. Our approach is based on two-photon laser lithography as a particularly flexible and accurate additive nanofabrication technique. We demonstrate the viability of the concept in a series of experiments that range from atomic force microscopy (AFM) engines offering atomic step resolution to operation of such engines underwater and to 3D-printed scanning near-field optical microscope (SNOM) structures. The technique is amenable to wafer-scale mass fabrication of SPM arrays and may unlock a wide range of novel application fields that are inaccessible to current SPM concepts.

Scanning probe microscopy (SPM)[121] is a widely used tool to analyse and manipulate objects on the nanometer scale, enabling, e.g., surface characterization [122], [123] and nanofabrication [124] with atomic resolution, high-density data storage [125], [126], or imaging of biological processes [127]–[129]. At its heart, SPM relies on interactions of a sample surface with a mechanical probe, commonly realized as a sharp tip with a nanometer-size apex attached to a micrometer-scale cantilever. In current SPM systems, tip and cantilever are usually structured in a dedicated microfabrication process before being manually mounted and aligned to a macroscopic optomechanical system for piezoelectric actuation and optical detection of sub-nanometer movements. This concept leads to rather bulky implementations and requires laborious operation, given that the tip is a wear part that has to be regularly exchanged and re-aligned to the read-out system. In addition, tip-cantilever geometries are currently restricted by the underlying fabrication techniques, relying on two-dimensional lithographic patterning and subsequent anisotropic etching. These techniques usually result in pyramidal tips with rather low aspect ratios, and the dimensions of the cantilever are often subject to fabrication tolerances that lead to variations of the resonance frequency of 30 % or more [130]. Moreover, current SPM systems are often limited in scanning speed, which inhibits high-throughput characterization of large sample areas. This may be overcome by arrays of SPM cantilevers for parallel scanning [131], [132], but the scalability and integration density of current SPM schemes is limited by the fact that each cantilever must still be individually addressed by a dedicated actuator and sensor element of macroscopic dimension. Chip-level integration of individually addressable cantilevers has been demonstrated in the context of nano-mechanical data storage, also known as “millipede memory”[125], [126]. These experiments resulted in an impressive number of more than 4000 cantilevers realized on a single substrate, but the functionality of each individual cantilever was restricted to creating and detecting indentations in polymer surfaces, corresponding to single-bit writing or reading, rather than allowing for characterization of general topographies. In many applications, it is further desirable to complement SPM by additional imaging modes. One of the most prominent examples is scanning near-field optical microscopy (SNOM)[74], [75], which is used to measure optical properties with sub-wavelength resolution, e.g., in life sciences [133], [134] and

material research [135]–[137], or for characterization of integrated optical devices [138], [139]. SNOM crucially relies on coupling of light to and from a metal nano-scale probe tip and hence requires additional macroscopic optical elements such as microscope objectives or mirrors that need to be precisely aligned. Alternatively, the probe can be realized as metal-coated tip of a tapered optical fiber with a nano-scale aperture at the apex. This concept allows to use the fiber to couple light to and from the probe tip but relies on elaborate fabrication processes, which often involve manual pulling or etching of the fiber tip, followed by delicate coating processes [140].

In this paper, we demonstrate that direct-write 3D laser lithography opens new perspectives for fabrication of particularly compact and robust SPM systems that overcome most of the aforementioned limitations. Our approach relies on two-photon polymerization and allows fabricating monolithic 3D freeform structures that combine cantilevers and tips with additional elements to fully functional SPM engines which are optically actuated and probed. The SPM engines are printed with high precision directly on facets of optical devices, thus rendering further alignment obsolete. The concept offers vast geometrical design freedom along with highly reproducible fabrication and lends itself to 3D-printing of large-scale SPM arrays with individual actuator and sensor elements. Moreover, additional imaging modes such as SNOM may be implemented by monolithic co-integration of the SPM engines with printed micro-optical freeform components such as lenses and mirrors. We demonstrate the viability of our approach by fabricating SPM engines directly on the facets of optical fiber arrays, which deliver and collect light for remote actuation and probing. These SPM engines offer atomic step-height resolution and are suited for operation both in air and in liquids. We further expand the concept to monolithically integrated SNOM engines, and which enable imaging of optical nanostructures with sub-wavelength resolution. To demonstrate that our approach is also suited for wafer-scale mass fabrication, we print more than 60 nominally identical devices and confirm their reproducibility. We believe that our experiments pave the route towards additive 3D nano-fabrication of a wide variety of highly integrated SPM systems.

6.1 Device Concept, Fabrication, and Characterization

The concept of a 3D-nanoimprinted SPM engine is illustrated in Figure 6.1. The structure is fabricated on the facet of a single-mode fiber (SMF) array through which light is guided to and collected from the device. A cut-open 3D model of the printed structure is shown in Figure 6.1(a), along with the various light paths (red). For actuation of the depicted structure, light is supplied through SMF1 and redirected by two total-internal reflection (TIR) mirrors to locally heat the metal-coated top surface of the cantilever, thereby inducing thermal expansion. By sinusoidal modulation of the optical power, we excite the cantilever close to its resonance frequency. The position of the cantilever is detected interferometrically through SMF2. To this end, light is emitted from the fiber facet towards a concave freeform mirror M_I at the bottom surface of the cantilever, designed for focusing a portion of the light back into the fiber core. Depending on the position of the cantilever, this portion of light interferes constructively or destructively with the Fresnel reflection at the inner fiber facet. By appropriate design of the freeform mirror, the optical amplitude of the back-coupled light can be matched to the Fresnel reflection from the fiber facet, thus ensuring complete extinction of the two partial waves for a relative phase shift of π, see Appendix A.3 for more details. The cantilever is equipped with a printed probe tip, which can be tailored to the specific application. Fibers SMF3 and SMF4 are used for complementing the SPM engine by SNOM functionality. To this end, the sample area around the probe tip is locally illuminated through SMF4 and a combination of a freeform metal mirror and a freeform lens, which are both printed along with the cantilever and the tip to ensure perfect alignment. For SNOM detection, the tip is equipped with a sub-wavelength metal aperture through which light is coupled to SMF3 and routed to a photodetector.

A scanning electron microscope (SEM) image of a fabricated SPM engine is shown in Figure 6.1(b). The cantilever and the optics of the SPM engine were 3D-printed to the SMF array by two-photon laser lithography; see Appendix B for more details. Two-photon lithography has previously been used for fabrication of a wide variety of functional structures, comprising, e.g., optical freeform elements at the facets of optical fibers [100] [J3] and optical single-mode

waveguides [62], [63] as well as AFM tips [40] and cantilevers [141] or read-out optics for scanning-tunneling microscope tips [142]. After 3D-printing the main structure, the top surface is covered by a metal coating of 5 nm chromium (Cr) followed by 100 nm gold (Au), the former acting as an absorber for the 785 nm actuation light supplied through SMF1. Dedicated shielding structures prevent unwanted metal coating of mirror and lens surfaces. For SNOM operation, a sub-wavelength aperture is opened at the apex of the tip by scanning across a corrugated metal surface. Details of the design and the fabrication of the SPM and SNOM engines can be found in Appendix B.1.

To calibrate the position sensor connected to SMF2, we move the fiber array with the SPM engine towards the surface of the sample using a high-precision piezoelectric translation stage while measuring the displacement of the position detector mirror M_I (Figure 6.1(c)). The vertical position at which the tip touches down on the sample surface defines the zero point of the *z*-axis; negative values of *z* correspond to a movement towards the surface leading to a deformation of the cantilever and a movement Δz_M of mirror M_I, whereas positive distances lead to a detachment of the tip from the sample surface. If the sample surface is stiff, Δz_M shows a linear *z*-dependence for $z < 0$ and the measured slope $|\Delta z|/|\Delta z_M| = 13.4$ corresponds to the ratio between the z-displacement $|\Delta z|$ of the probe tip and the *z*-displacement $|\Delta z_M|$ of the interferometer mirror M_I (Figure B4). The measured displacement ratio is in good agreement with its simulated value of 13.6; see Appendix B.2 and B.3 for details of the position sensor readout and the simulation technique. We also estimate the force acting on the tip during the experiment by multiplying the tip displacement with the simulated spring constant of $c_{AFM} = 64\,\mathrm{N/m}$, see Appendix B.2 for details.

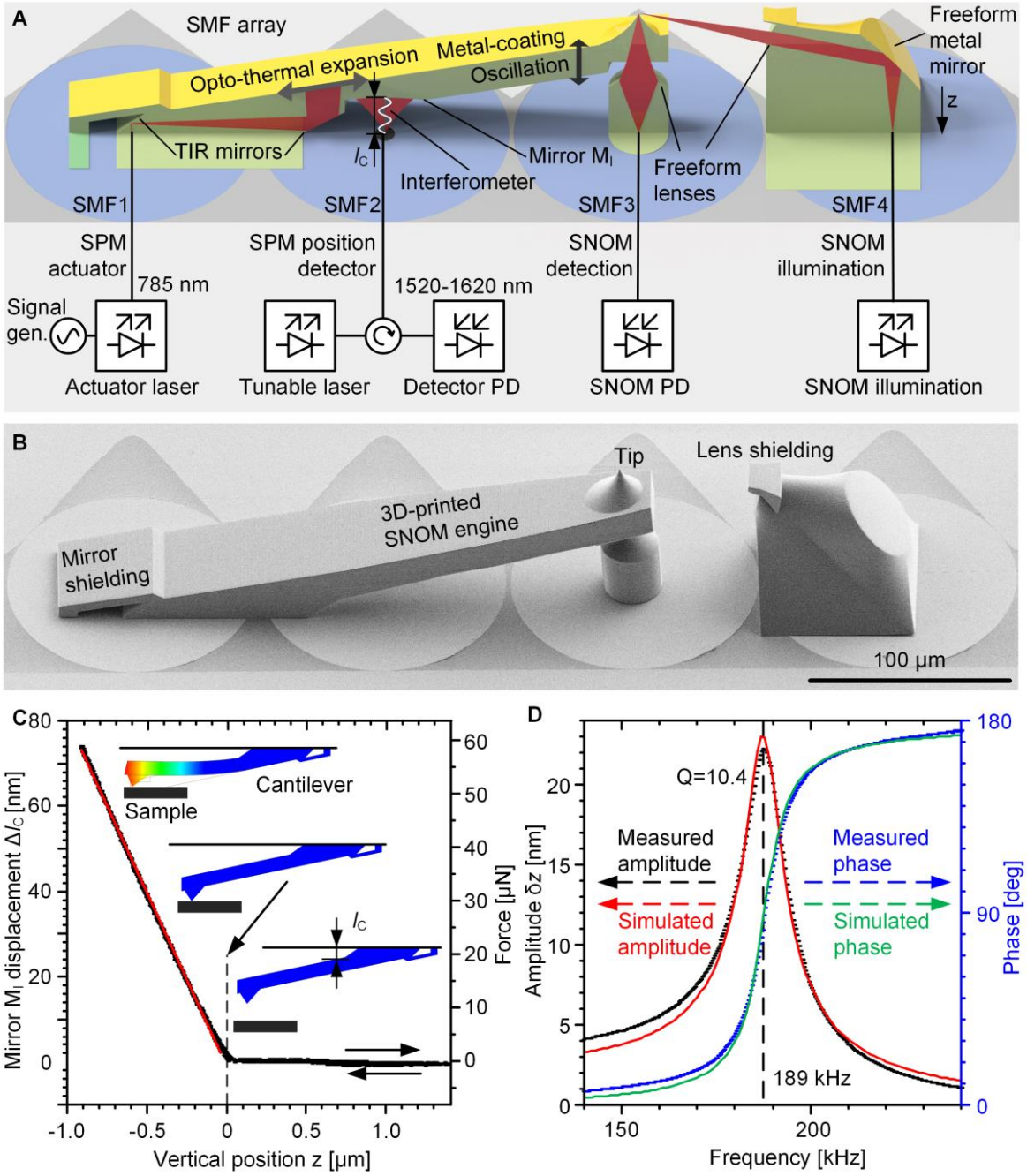

Figure 6.1. Concept of 3D-nanoprinted SPM engines. 3D-printing allows realizing a large variety of designs for ultra-compact SPM engines. The illustrated device is attached to the facet of a single-mode fiber array and combines atomic force microscopy (AFM) and scanning near-field microscopy (SNOM) functionality. Micro-optical elements used for SNOM illumination and light collection are printed along with the cantilever and the tip to ensure perfect alignment. **A,** Schematic drawing of the SPM engine (green) including metal coatings (yellow) and light propagation paths (red). The cantilever is actuated by light supplied through SMF1, which is redirected by two total-internal reflection (TIR) mirrors to locally heat the metal-coated top

surface. The position of the cantilever is detected through SMF2 by exploiting the interference of light reflected from a freeform mirror M_I with the Fresnel reflection at the inner surface of the plane fiber facet. SMF4 is used to locally illuminate the sample for SNOM excitation. For detection, the tip is equipped with a sub-wavelength metal aperture through which light is coupled to SMF3. **B,** Scanning electron microscope (SEM) image of the SPM engine. Shielding structures prevent unwanted metal coating of lens surfaces. **C,** Characterization of the AFM position sensor: The AFM engine is moved along the vertical direction (z-direction) towards the sample surface by a high-precision piezoelectric positioner while monitoring the displacement Δz_M of the mirror M_I. Negative values of z correspond to a movement towards the surface leading to a bending of the cantilever, whereas positive distances lead to a detachment of the tip from the surface. Due to a rather high spring constant of $c_{AFM} = 64\,\mathrm{N/m}$, the cantilever does not exhibit any jump-to-contact behavior. **D,** Characterization of the mechanical cantilever resonance: Measured (black) and simulated (red) oscillation amplitude δz and measured (blue) and simulated (green) phase of the tip as a function of the power modulation frequency. The phase and the amplitude characteristics exhibit a distinct resonance at a frequency of 189 kHz with a quality factor of $Q \approx 10.4$. Such quality factors are typical for polymer cantilevers and allow for fast scanning [143].

To characterize the dynamic behaviour of the cantilever, we sweep the power modulation frequency of the optical actuation signal and continuously measure the oscillation amplitude of the cantilever using the position detector (Figure 6.1(d)). This measurement was done with a commercially available AFM controller that comprises a signal generator for modulating the actuation power and a lock-in amplifier for read-out of the position detector. The measured phase (blue) and amplitude (black) show good agreement with simulations (green and red); see Appendix B.4 for more details. From these measurements, we extract a resonance frequency of 189 kHz and a quality factor of $Q \approx 10.4$. Such rather low quality factors are typical for cantilevers made from polymers and allow for fast scanning [143]. When exciting the cantilever at its resonance frequency with an optical signal at a wavelength of 785 nm and an optical power modulation amplitude of approximately 10 mW, we find a tip oscillation amplitude of 24 nm, which is sufficient for most applications. Details of the measurement technique can be found in Appendix B.2 and B.3. The oscillation amplitude can be controlled by appropriate choice of the power modulation amplitudes or by adapting the mechanical design to provide softer or stiffer cantilevers.

6.2 Atomic Step-Height Resolution

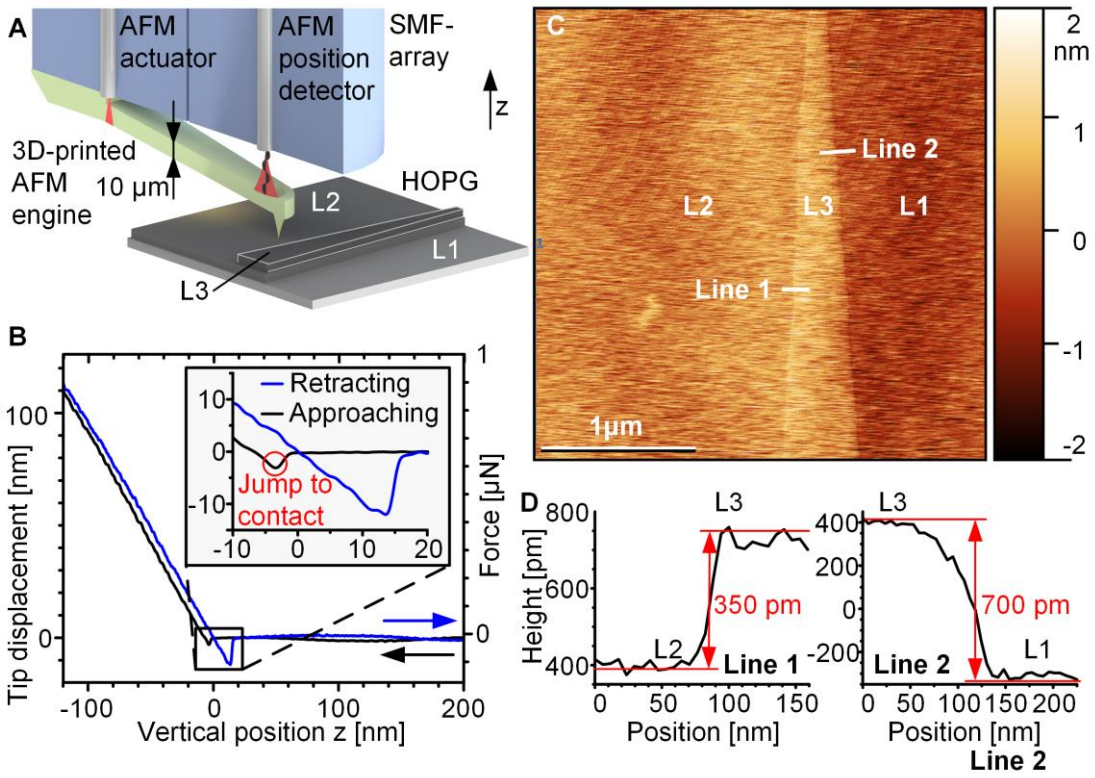

Figure 6.2. Demonstration of 3D-printed AFM engines that offer an atomic step-height resolution. **A,** Schematic of the structure and the associated experiment, in which we sample the surface of freshly cleaved highly oriented pyrolytic graphite (HOPG). **B,** Characterization of the AFM position sensor. The force axis was obtained from multiplying the tip displacement with the simulated spring constant of $c_{\mathrm{AFM}} = 12\,\mathrm{N/m}$. Inset: Typical jump-to-contact behavior. **C,** Measured surface topography of the HOPG sample. Three different atomic layers L1, L2 and L3 are visible. **D,** Line-scans along Line 1 and Line 2 for a one-layer (L2-L3) step and a two-layer (L3-L1) step, as indicated in c. The measured step heights amount to 350 pm for a single atomic layer and to 700 pm for two atomic layers – in agreement with literature values [144].

To demonstrate the viability of the concept shown in Figure 6.1, we test its ability to measure atomic steps. We fabricate a simple AFM engine without SNOM functionality (Figure 6.2(a)), which features a reduced cantilever thickness of 10 µm and a reduced spring constant of $c_{\mathrm{AFM}} = 12$ N/m, see Appendix B.2. In addition, we place the AFM position detector right below the tip to directly

extract the tip movement (displacement ratio $|\Delta z|/|\Delta z_M| \approx 1$). To demonstrate the sensitivity of the interferometric AFM position detector, we again bring the tip in contact with and detach it from a glass substrate (Figure 6.2(b)), now observing a typical jump-to-contact behavior due to the reduced spring constant. The vertical resolution of the AFM engine is demonstrated by sampling the surface topography of a freshly cleaved highly oriented pyrolytic graphite (HOPG) sample (Figure 6.2(c)) using dynamic operation mode of the AFM engine, see Appendix B. From the measured topography, we extracted line scans across steps of one and two atomic layers (Figure 6.2(d)), exhibiting step heights of approximately 350 pm and 700 pm. These results are in good agreement with literature values of 335 pm per layer [144]. While this resolution is already sufficient for many applications, the sensitivity of the AFM position readout can be further increased by using low-noise laser sources and a Fabry-Pérot cavity with high optical Q-factor [145] rather than a simple interferometer. This requires highly reflective mirrors on the fiber facet and on the cantilever; see Appendix B.5 for details.

6.3 Measurements in Liquids

In a second experiment, we show the unique capability of our AFM engines to switch between measurements in air and in liquids, which is needed, e.g., for imaging of biological samples [127]–[129] and process monitoring in chemical reactors, or integration of AFM engines into microfluidic systems [146]. The associated structure (Figure 6.3(a)) is again printed onto the facets of an SMF array, which enables remote operation over extended distances without any mechanical alignment of the AFM components. The cantilever is now designed as a massive structure with a thickness of 21 µm, leading to a dynamic behavior that is rather insensitive to the surrounding medium. Note that immersion into an ambient liquid decreases the reflection both at the SMF facet and at the curved mirror of the position detector, making the position detection more sensitive with respect to spurious light reflected from the sample surface. To avoid unwanted interference, we therefore modify the position detector by adding a metal mirror that deflects excess light away from the optical axis of the interferometer (Inset of Figure 6.3(a)). To demonstrate the performance of the

system, we measure the mechanical resonance curve both in air and in water (Figure 6.3(b)). It is interesting to note that our approach allows to locally excite the cantilever at a well-defined spot and that the resonance spectrum does not exhibit additional peaks as frequently observed when operating conventional AFM in liquids [147]. The ability of our AFM engines to work both in a liquid and in a gaseous environment without any realignment is demonstrated by sampling the same area of an optical grating with a nominal structure height of approximately 60 nm, first in air (Figure 6.3(c)) and then in water (Figure 6.3(d)). Between the two measurements, we only adjusted the feedback control parameters for dynamic-mode operation and the position detector read-out wavelength to maintain an operating point of maximum sensitivity after immersing the cavity in water. The two topography measurements show a slight lateral offset of approximately 1.1 µm, which we attribute to thermal drift of the macroscopic scan stages while immersing the sample. We observed that the measurement in air indicates a smaller height difference between the grating grooves and ribs than the measurement in water. We attribute this to a variation of the mechanical Q-factors of the cantilever when scanning in grooves compared to scanning on top of ribs. This effect is known to lead to deviations in measured step heights [148], [149]. Still, the capability of sampling nanoscopic objects in various environments without mechanical realignment of the AFM engine is a unique feature of our concept. Operation of conventional AFM assemblies in liquids requires mechanical realignment of the laser beam to compensate for optical refraction at the liquid surface. Offering compact footprint, robustness, simple alignment, and remote operation through optical waveguides, we expect that 3D-printed SPM engines will open new perspectives for *in-vitro* and *in-vivo* imaging [127]–[129] for applications in lab-on-chip or microfluidic devices [146], or for endoscopic AFM systems.

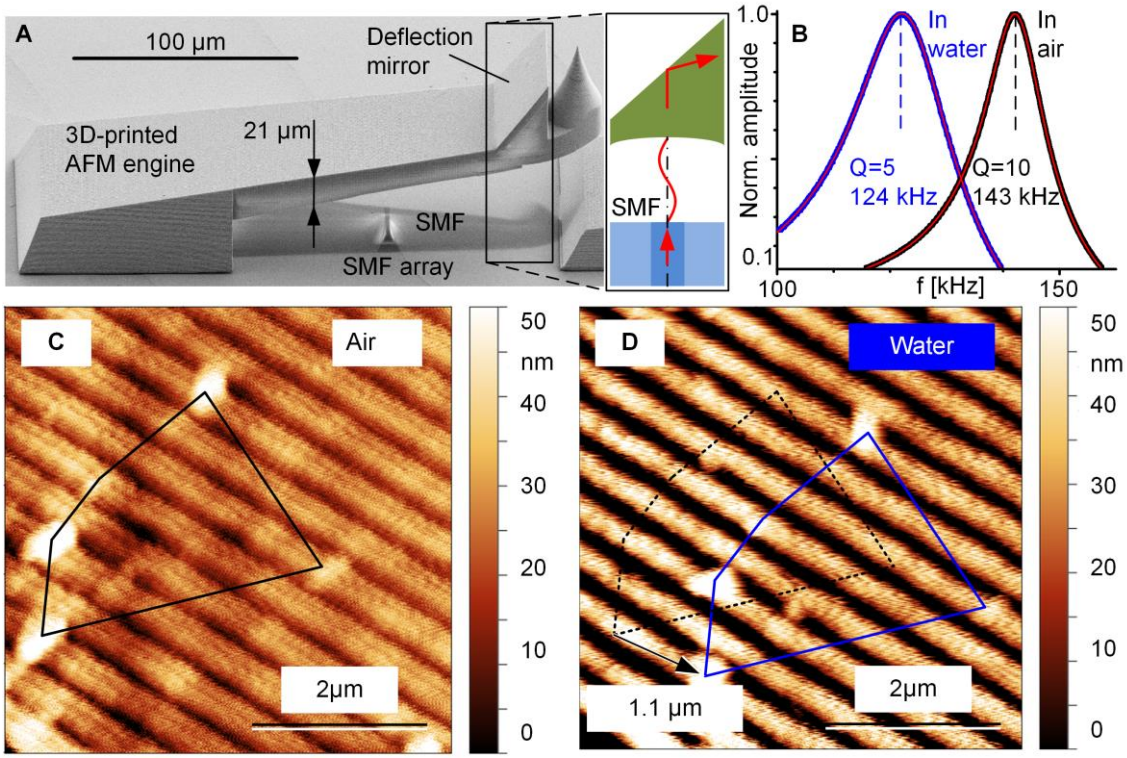

Figure 6.3. Demonstration of 3D-printed AFM engines that allow for measurements in air and in liquids. **A**, SEM image of the 3D-printed structure. The rather thick cantilever leads to a dynamic behavior that is rather insensitive to the surrounding medium. Inset: To minimize the impact of spurious reflections from the sample surface, the structure is equipped with a metal deflection mirror that redirects excess light away from the optical axis of the interferometer. **B**, Mechanical resonance spectrum measured in air (black) and water (blue). The resonance frequency and the mechanical Q-factor were determined by fitting a Lorentz-type model function (red) to the measured data, see Appendix B.4. **c,d,** Surface topography of a grating structure measured in air c, and water d, without intermediate mechanical realignment of the AFM engine. The positions of surface features in air and water are indicated by black and blue lines, respectively. The two measurements show good agreement except for a minor lateral offset of approximately 1.1 µm, which we attribute to thermal drift of the macroscopic scan stages. The measurement in air indicates a slightly smaller height difference between the grooves and the ribs of the grating than the measurement in water immersion, which we attribute to the different mechanical Q-factors of the cantilevers in both environments [148], [149].

6.4 3D-printed SNOM Engines

For standard SPM systems, co-integration with other analytical tools for multi-modal sensing such as SNOM [74], [75] is technically complex, often involving manual micro-assembly of discrete components such as metal-coated optical fibers, tuning forks, and additional optical elements for illumination or light collection. These challenges can be overcome by 3D-nanoprinting of SNOM engines as monolithic structures that comprise all relevant elements. For demonstration, we perform a first set of experiments that is dedicated to high-resolution sampling of optical fields on fiber and laser facets. To this end, we use a SNOM engine similar to the one depicted in Figure 6.1(a), but without the tip illumination, which is not needed for characterization of active components. Details on the device and on the experimental results can be found in Appendix B.6. Building upon these results, we then demonstrate simultaneous SNOM and AFM characterization of photonic nanostructures. For these experiments, the light collection functionality is complemented by localized illumination, offered by a 3D-printed mirror-lens combination (Figure 6.1. and Figure 4.4(a). Details of the structure can be found in Appendix B.1. To demonstrate the functionality of the SNOM engine, we measure an array of gold (Au) nano-antennae on a Si-surface (Figure 6.4(a,b,c). For illumination of the SNOM tip, we use a super-continuum light source featuring a fiber-coupled power of approximately 5 mW and a spectrum ranging from 1180 nm to 2400 nm with a peak around 1500 nm, see Appendix B and Appendix B.6. An SEM image of a single nano-antenna is shown in the Inset of Figure 6.4(a). Figure 6.4(b) and C show the measured AFM topography and the corresponding SNOM image of a subsection of the antenna array. Both images were recorded simultaneously. The overview image of Figure 6.4(b) is distorted by the limited resolution of the large-area scanning stage that was used in this experiment. This problem disappears when scanning an individual antenna with a smaller range, see Inset of Figure 6.4(b) and Figure 6.4(c). The SNOM images in Figure 6.4(c) and in the corresponding Inset 3 show topographical artifacts, *i.e.*, topography-induced features in the measured SNOM signal that originate from vertical movement of the aperture while scanning over the surface topography. Such topographical artifacts are typical for true SNOM images [76] and can be avoided by measuring in so-

called constant-height modus, where the tip does not follow the surface topography [76]. From the data shown in Figure 6.4(c), we estimate a SNOM resolution of approximately 300 nm by fitting a Gaussian model function with a constant offset to one of the peaks and by determining the full-width at half maximum (FWHM) of the Gaussian. For an illumination wavelength of $\lambda = 1550$ nm, this corresponds to a resolution of roughly $\lambda/5$, without accounting for the finite extension of the test structure itself, which would improve the measured resolution slightly. Note that these experiments represent a first proof-of-concept demonstration of compact and highly scalable 3D-printed SNOM engines and that the performance of the structures has not yet been optimized. As an example, the resolution of the SNOM imaging can be improved by using, e.g., scattering-mode tips that do not feature an aperture and/or by using 3D-printed parabolic mirrors for highly efficient high-NA excitation or read-out [142]. We believe that further optimization of the design and fabrication techniques will finally enable performance parameters that are on par with highly optimized conventional SNOM systems, for which resolutions down to $\lambda/20$ were reported [74].

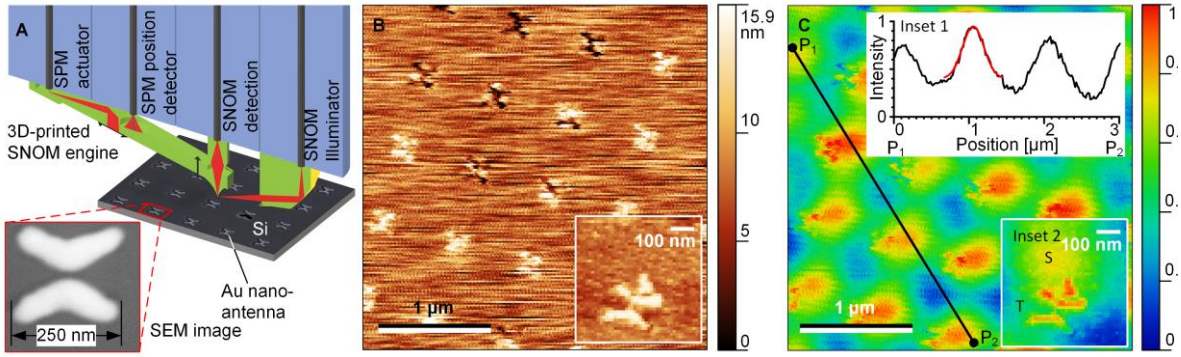

Figure 6.4. Simultaneous AFM and SNOM imaging of passive optical nanostructures. **A**, The measurement relies on a printed AFM engine with a dedicated mirror-lens combination for local illumination of the SNOM tip (Figure 6.1(a) and (b). The sample consists of metallic gold (Au) nanoantennae on a dielectric (Si) substrate. Inset: SEM image of an individual nanoantenna. **B**, Sample topography determined from the AFM signal. The distortions originate from the limited resolution of the large-area scanning stage (800 µm travel range) that was used in this experiment. Inset: Surface topography of an individual antenna taken with a different scanning stage. **C**, SNOM signal obtained when using a fiber-coupled super-continuum light source having a spectral peak at approximately 1500 nm for illumination. The SNOM detector signal is normalized to the maximum value that was found in the image. Inset 1: Normalized intensity of the SNOM signal along the line from P_1 to P_2. The resolution of the SNOM image amounts to approximately 300 nm as indicated by the full-width at half maximum (FWHM) of a Gaussian fit (red). The performance can be greatly improved by optimizing the design and the fabrication processes. Inset 2: SNOM signal S of an individual antenna, indicating a clear topographic artifact T, which is typical for true SNOM images [76] and can be avoided by performing a dedicated SNOM measurement in the so-called constant-height modus.

6.5 Wafer-Level Fabrication of SPM Arrays

3D-printed SPM engines lend themselves to wafer-level mass fabrication and thus open a path towards massively parallel scanning of large sample surfaces. Figure 6.5(a) illustrates a vision of a SNOM array printed onto a photonic integrated circuit (PIC) that allows for processing of optical actuation and read-out signals. This approach allows exploiting the scalability as well as the wealth of functionalities offered by advanced photonic integration platforms such as silicon photonics [150], [151], III/V semiconductors [152], or low-loss material systems such as silicon nitride [153]. Low-loss coupling between on-chip waveguides and functional part of the SPM engines can be accomplished by free-form optical coupling elements that combine, e.g., single-mode waveguides

with micro-lenses [154] (Inset of Figure 6.5(a)). 3D-printing of advanced SPM arrays crucially relies on the reproducibility of the structures, both with respect to dimensional fidelity and to functional parameters such as spring constant and resonance frequency of the cantilever. To investigate these aspects, we have fabricated and characterized arrays of nominally identical SPM cantilevers on plain fused silica substrates (Figure 6.5(b). Results for the SNOM-type cantilever (Figure 6.1) are given in Figure 6.5(c) and (d), whereas results for the AFM-engines (Figure 6.2) and details on fabrication can be found in Appendix 0. The reproducibility of the cantilever height above the substrate is a crucial parameter when sampling extended surfaces by a large-scale array of SPM engines. To measure the height variation, we use a vertical-scanning white-light interferometer (VSI), see Appendix 0. A histogram of the measured height of 66 SNOM cantilevers is shown in Figure 6.5(c), indicating a standard deviation of $\sigma_\mathrm{h} \approx 690\,\mathrm{nm}$ and an average height of 69 µm, *i.e.*, a relative deviation of approximately 1 %. The height of individual cantilevers may be controlled by using additional optical actuators for individual fine-tuning, see Appendix 0. In addition, the reproducibility of the cantilever resonance frequency is crucial, as identical resonance frequencies allow to use a collective excitation signal for a multitude of SPM engines. The variance of the resonance frequency is measured by mechanically exciting the 66 SNOM cantilevers using a piezo actuator below the substrate and by measuring the individual oscillation amplitudes using a deflection laser. The histogram of the measured resonance frequencies is depicted in Figure 6.5(d), indicating a standard deviation of $\sigma_\mathrm{f} = 3.98\mathrm{kHz}$ for an average resonance frequency of $188.2\,\mathrm{kHz}$. This corresponds to a relative one-sigma uncertainty of $2.1\,\%$, which is far below the uncertainties of $30\,\%$ that are commonly observed for state-of-the-art silicon or silicon-nitride cantilevers [130]. Note that the96hermoance frequency of printed SPM cantilevers can be thermally tuned by varying the average optical excitation power and hence adjusting its stiffness, see Appendix 0.

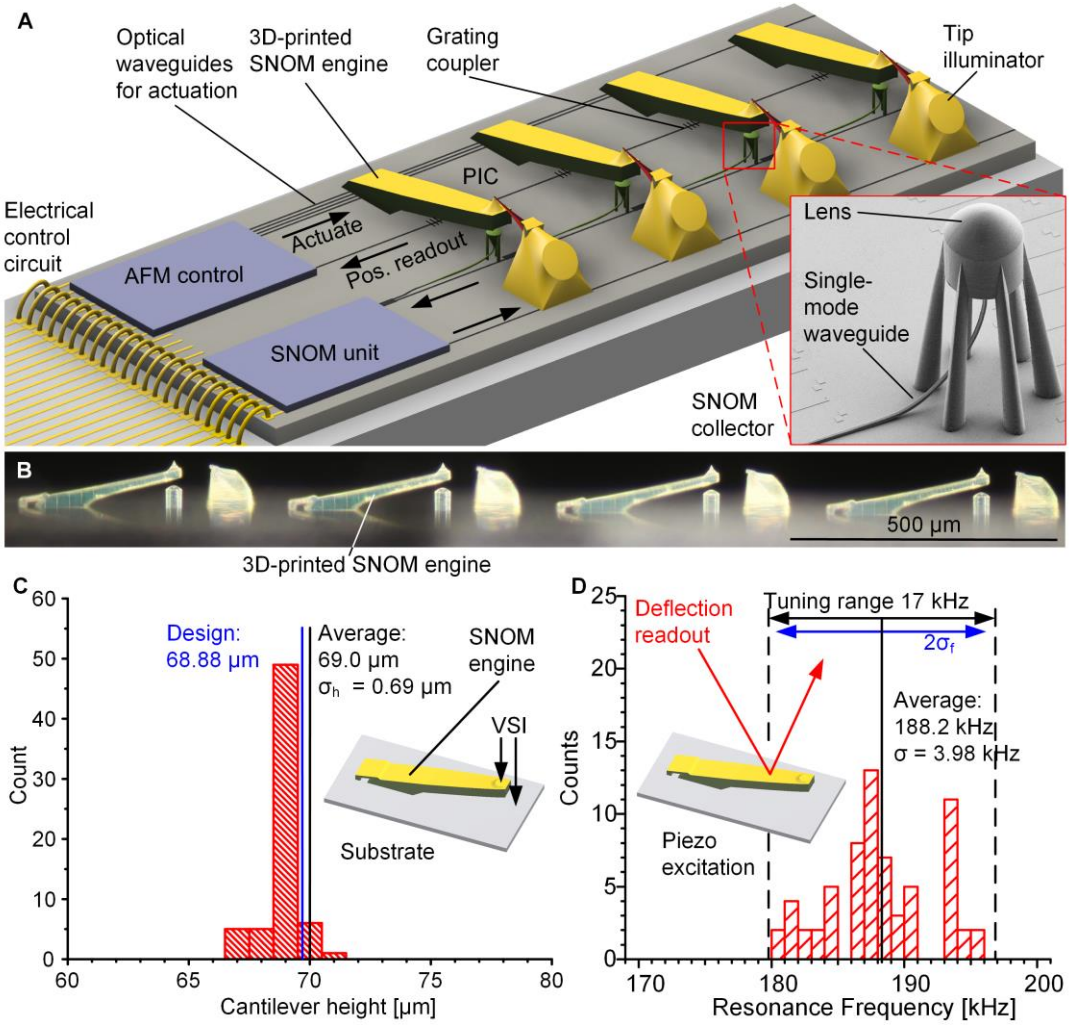

Figure 6.5. Wafer-level fabrication and reproducibility of SPM engines. **A**, Vision of SPM arrays, printed onto a photonic integrated circuit (PIC) that allows for processing of optical actuation and read-out signals. Parallelization of 3D-printed SPM engines could open a path towards efficient scanning of large sample surfaces. Inset: Coupling of light between SPM engines and planar lightwave circuits can either rely on grating structures [81], as indicated for the position readout, or on free-form optical coupling elements that combine single-mode waveguides with micro-lenses [154]. **B**, Light-microscope image of four cantilevers printed on a quartz substrate. **C**, Histogram showing the height variation of 66 SNOM engines printed onto a plane quartz substrate. The heights exhibit a standard deviation of $\sigma_h \approx 690$ nm. Residual height variations may be compensated using dedicated optical actuators for individual fine-tuning of the cantilever positions. **D**, Histogram displaying the resonance frequency of the 66 cantilevers. A piezo actuator was used to mechanically excite the cantilevers with a frequency sweep, and the readout was performed by measuring the deflection of a laser using a split photodiode. The standard deviation amounts to $\sigma_f = 3.98$ kHz for an average resonance frequency of 188.2 kHz.

6.6 Summary and Outlook

We have introduced a novel approach for fabricating highly compact scanning probe microscopy (SPM) systems with unprecedented versatility and functional design freedom. Our approach exploits high-resolution two-photon laser lithography for *in situ* printing of SPM engines onto the facets of optical devices, which provide optical actuation and read-out signals. Enabling high-precision monolithic co-integration of SPM engines with printed micro-optical components such as lenses and mirrors, the concept is ideally suited for incorporating additional imaging modes such as scanning near-field optical microscopy (SNOM). We demonstrate the viability of the approach in a series of experiments that range from atomic force microscopy (AFM) engines with atomic step height resolution to operation of AFM engines underwater and to SNOM implementations that allow for characterizing both active and passive photonic components. We further confirm that the technique is amenable to wafer-level fabrication of massively parallel SPM arrays. Our concept may pave the path towards advanced SPM systems may unlock a wide range of scientific and industrial applications that are inaccessible to current SPM concepts.

[end of paper [J2]*]*

7 Thesis Summary and Outlook

7.1 Summary

This work demonstrates micro-optical structures enabled by 3D laser lithography, a versatile method to fabricate micro-optical systems for applications ranging from optical communications and astro-photonics to scanning probe microscopy. In particular, this work demonstrates that 3D freeform optical elements printed to device facets can be used for highly efficient and position-tolerant coupling of photonic components. This work explores and demonstrates a toolbox of essential beam-shaping elements required to build hybrid optical assemblies: Freeform lenses, freeform mirrors and multi-lens beam expanders that relaxed transverse alignment tolerances. As an inevitable consequence of relaxing transverse alignment accuracies by mode-field expansion, the requirements on angular alignment accuracies were increased. As angular alignment can simpler achieved than transverse alignment accuracies, the proposed approach simplifies the alignment challenge to a degree that passive alignment can be used.

In a first set of experiments, Chapter 4.3.1, this work demonstrates single freeform lenses printed either to laser or fiber facets, leading to coupling losses of 0.6 dB from a laser to a single-mode fiber (SMF) after active alignment. A second set of experiments, Chapter 4.3.2, is dedicated to freeform total-internal reflection (TIR) mirrors that combine surface- and edge-emitting optical components in compact assemblies. We further demonstrate the viability of the approach by coupling vertical-cavity surface-emitting lasers (VCSEL) to single-mode fibers (SMF) using printed freeform mirrors on either the laser or the SMF end face. The coupling losses amount to 1.1 dB after active alignment. A third set of experiments, Chapter 4.3.3, demonstrates that beam expanders on both facets of a coupling interface allows relaxing of positioning tolerances. Using an SMF pair as a well-defined model system, we achieve coupling losses of 1.9 dB for a compact two-lens beam expander upon active alignment. The loss is mainly limited by Fresnel reflection. The lateral 1 dB alignment tolerances amount to ± 5.5 µm. Moreover, this work shows coupling of edge-emitting lasers to SMF and to passive TriPleX chips, with coupling losses of 0.8 dB and

2.5 dB, respectively, upon active alignment of the devices. The transverse1 dB position tolerances amount to approximately ± 5 µm. These transverse alignment tolerances are sufficient for passive alignment, as shown in follow-up experiments.

This work also demonstrates that facet-attached beam-shaping elements can be fabricated with high reproducibility, leading to coupling efficiency variations of less than ± 0.1 dB, see Appendix A.8. The approach can be transferred to various edge-emitting and surface-emitting devices and could pave the path towards large-scale passive alignment of optical components. For reducing the Fresnel reflection in multi-lens systems, this work introduces the concept of low index-contrast micro-optical systems (LIMOS). Here, 3D-printed micro optics is immersed into an index matching material to reduce reflection loss. The viability of the approach is shown by coupling a pair of SMF via a pair of LIMOS beam expanders comprising a total of 18 lens surfaces. The LIMOS approach significantly reduces coupling loss to 1.0 dB, which is below the minimum losses that can be theoretically achieved by lenses operated in air.

For applications in astro-photonics, freeform lenses were fabricated on the facet of multi-core fibers (MCF). Coupling of light into MCF for spatially resolved spectroscopy is of great importance to astronomical instrumentation. To achieve high coupling efficiency and a fill-fraction close to unity, micro-optical elements are required to concentrate the incoming light to the individual cores of the MCF. In this work, facet-attached lens arrays (LA) were fabricated by two-photon polymerization. The LA provides a fill-fraction close 100 % and efficiencies of up to 73 % (1.4 dB) for coupling of light from free space into an MCF core. The viability of the concept for astrophotonic applications was shown by integrating an MCF-LA assembly in an adaptive-optics testbed and assessing its performance as a tip/tilt sensor.

For scanning probe microscopy (SPM) measurements, this work introduced a novel approach for fabricating highly compact SPM systems with unprecedented versatility and design freedom. The approach again exploits high-resolution two-photon laser lithography for *in situ* printing of SPM engines onto the facets of optical devices, which provide optical actuation and read-out signals, enabling high-precision monolithic co-integration of SPM engines with printed

micro-optical components such as lenses and mirrors. This work demonstrates the viability of 3D-printed SPMs in a series of experiments that range from atomic force microscopy (AFM) engines with atomic step height resolution to operation of AFM engines under immersion in a liquid and to SNOM implementations that allow for characterizing both active and passive photonic components. It was further confirmed that the technique is amenable to wafer-level fabrication of massively parallel SPM arrays. The concept paves the path towards advanced SPM systems unlocks a wide range of scientific and industrial applications that are inaccessible to current SPM concepts.

7.2 Outlook and Future Work

In this work proof-of-concept experiments of *in situ* micro-fabrication for various applications in the field of micro-optics have been demonstrated. Future work focuses on advancing industrial maturity of the technology. The industrial applicability requires reliability demonstration and increased fabrication speed which is both described in this section.

Reliability Demonstration

For commercial applications, reliability tests have to be demonstrated in future work. So-called "Telcordia tests" [155] are *de-facto* industry standards for many reliability demonstrations. The test protocols are application-specific. For optical communications, "GR-468 Generic Reliability Assurance Requirements for Optoelectronic Devices Used in Telecommunications Equipment" and "GR-1221 Generic Reliability Assurance Requirements for Passive Optical Components" are most relevant. Telcordia tests include vibration tests, mechanical shock tests and thermal cycling from -40°C° to 85°C°. Due to cost advantages, non-hermetic optical assemblies [53] are very attractive. Without hermetic packaging, lenses must withstand damp-heat tests, particularly over more than 2000 h at ambient temperatures of 85°C and 85% relative humidity. For some applications, reliability tests must be conducted while operating the relevant optical system.

These demonstrations must be performed on a representative test system that allows easily accessible confirmation of a possible failure. Additionally, there are also some highly relevant aspects that are not fully covered by Telcordia tests. These include the assembly of multi-chip modules, which often requires elevated temperatures. While ultrasonic electrical wire bonding requires temperatures between 25°C and 150°C, lead-free Sn/Au soldering [156] requires 250 °C and thermo-compression bonding requires 300°C and beyond [157]. The soldering process is based on specific temperature profiles. Typically, the maximal temperature is held for up to 60 s. Lenses must be compatible with such procedures to ensure compatibility with standard assembly processes. Moreover, emerging applications such as quantum computing [158], [159] and operation in space [160] make compatibility to cryogenic temperatures and vacuum as well as low outgassing necessary [161].

The material used for 3D-printing plays a key role concerning reliability, as most failure modes are material related. This work relies on the photoresist IP-Dip [118]. While this material was suitable for initial demonstration of 3D-printed freeform lenses, it shows numerous disadvantages: The material generally shrinks in the range of 1 … 5 % upon development. Moreover, heating after 3D-printing or extended storage time results in detachment, most likely caused by incomplete conversion of monomers [162][163]. As a result, the structures presented within this work degraded rapidly during stress tests. Therefore, research to develop more appropriate and reliable resist materials is required for a successful commercialization.

Alternatively to improved acrylic photoresists, a hybrid Zr-based photoresist [25] like ZR2080 is a possible option. Here, a sol-gel reaction prior to 3D-printing avoids shrinkage during 3D-printing as the material is already solid. The resulting structures show both low shrinkage upon polymerization and chemical development. This material was not used for this work because a solidification step prior to 3D-printing is not compatible with the fabrication mode shown in Figure 2.3. Therefore, to make use of a hybrid material, extensive adaptation in the fabrication processes would have been necessary.

As these commercially available material options appear not to be suitable for applications targeted within this thesis, follow-up work focuses on the

development of liquid material that allows high-resolution fabrication while at the same time showing high degree of conversion. As a result, 3D-printed structures show close to zero shrinkage upon fabrication, development and reliability tests. This structural integrity ensures long-term stability and can therefore also used for industrial applications.

Fabrication Speed

For these proof-of-concept experiments, the fabrication speed was not a relevant parameter, and fabrication took per structure – highly depending on the structure – in the range of few minutes to one hour. For industrial applications, the technology will be only applicable if sufficiently low cycle times of lens fabrication in the sub-minute regime, ideally 10 s or less, can be achieved. The fabrication speed limitation comes from various influence factors:

Before lens fabrication, a localization of photonic components is required. This localization may, in some cases, take longer than the lens fabrication itself. Therefore, faster interface detection for the lens alignment using more intelligent searching algorithms and high-speed cameras or other metrological methods and highly dynamic translation stages are required.

For faster fabrication, lasers with considerably higher power are needed. Laser power is limited mainly by the available lasers, the damage threshold of the lithography tool's optical components such as mirrors and lenses, and the photoresist's damage threshold. The photoresist's damage threshold can be increased by choosing suitable, non-absorbing monomer material and suitable photoinitiators.

Alternatively to higher laser powers, lasers with wavelengths that are more suitable for commercially available photoinitiators may be used, e.g., with a wavelength of 520 nm, generated, e.g. by frequency-doubled Yttrium doped fiber lasers. The lithography performance with such 520 nm lasers is potentially superior to 780 nm, as there are more photoinitiators available with high sensitivity in the range of 260 nm than 390 nm.

Additionally, many initiators for two-photon polymerization typically have a higher two-photon cross-section at a lower wavelength, potentially allowing faster structuring due to an increased sensitivity. Additionally, a wavelength of 520 nm is in the middle of the visible spectrum, for which objective lenses are exceptionally well optimized, allowing better focusing and thus more efficient polymerization. Also, the lower wavelength will give some advantage due to the smaller diffraction-limited beam.

Also initiators that have been specifically synthesiszed for fs-lasers may be used. Most photoresists used today for two-photon polymerization are originally designed for UV-lithography or curing. Emerging, application-tailored photoinitiators show higher two-photon cross-sections and polymerization efficiencies. However, such photoinitiators have to be carefully tailored for other desirable properties in two-photon polymerization, such as high resolution and high conversion efficiency. A further, promising approach, aims at using a photoinitiator that is excited via a non-virtual intermediate excitation energy level [30].

A similar effect as with application-tailored photoinitiators could be achieved by combining an initiator with a sensitizer or co-initiator. Here, one component absorbs light and transfers energy to a second initiator that is not sensitive at the wavelength used. A co-initiator's advantage is that the two-photon cross-section, as a primary criterion for high efficiency, is de-coupled from other photoinitiators' properties such as diffusion rate, conversion efficiency or radical reactivity.

The most substantial limitation of fabrication speed in this work was the finite temporal resolution of galvanometer scanners. The control commands are on a 10 µs time grid, which at a required accuracy of 100 nm limits scanning speed to 10 mm/s. Therefore, higher digital bandwidth is an important requirement for faster fabrication. Additionally, galvanometer scanners and power modulation with high bandwidth are needed. The power modulation must also be well synchronized to the galvanometer scanner.

Alternatively to higher bandwidth of the scanner system, adaptive fabrication strategies may be used, e.g., by scanning at higher speed within the structure

and lowering the scanning speed, where high precision is required, e.g., at the lens surface, Figure 2.2.

Finally, there is a large speed-up potential in creating photonic systems that feature both discrete, micro-lenses and 3D-printed lenses [7]. In this approach, lenses with a relatively large size and low shape and positioning accuracies could be realized as discrete, spherical micro-lenses. Additionally, 3D-printed lenses could be fabricated on facets of photonic components, where high alignment accuracies are needed. The aspherical 3D-printed lenses could also correct spherical aberration of the discrete micro-lenses and thereby provide high coupling efficiency.

Further application based on in situ 3D-printing

This work's demonstrations are a starting point for 3D-printing of facet-attached functional microsystems. A wealth of new applications in various fields are based on developments of this work.

In the field of optical coupling, lenses as shown in Figure 4.3(a) have enabled a mass-manufacturable microscopic device optical coherence tomography [J6]. Furthermore, an approach was demonstrated that combines 3D-printed structures, similar to those in Figure 4.5(a), with discrete micro-lenses, for bio-sensing in the visible range and for pluggable photonic systems in the near-infrared [7]. The technology developed in this work also helped to produce a structure for low-loss coupling from SOI chips to SMF [154] by combining photonic wirebonds (PWB) with 3D-printed freeform lenses. Moreover, based on feasibility demonstration of this thesis, passive placement [8] of photonic components equipped with 3D-printed lenses were demonstrated.

Moreover, based on technological developments of this work, advanced beam shapers for LiDAR [10] were developed as well as coupling structures for cryogenic temperatures [9] that will help to create detectors for quantum computing. Furthermore, 3D-printed mirror-lens combination for wafer-level testing [12] were developed that are based on micro-optics similar to those shown in Figure 4.4(d). Moreover, processes to create tools for moulding lenses [P5] were developed based on this work, which opens new routes for mass

manufacturing of 3D-printed freeform lenses by replication, e.g., using injection moulding.

In the field of astro-photonics lens arrays on multi-core fibers for spectroscopy [14] were developed based on this work as well as advanced tip-tilt sensors [13] similar to those shown in Figure 5.1.

Also in the area of scanning probe microscopes (SPM), 3D-printed atomic-force microscope (AFM) tips [J5] on cantilevers that can optionally be carbonized [41] were demonstrated based on this work. Additionally, endoscopic instruments fabricated on the facet of a multi-core fiber (MCF), relying on the same operation principle as in this work, were successfully used [11]. Moreover, SNOM-systems with improved resolution and efficiency were investigated as well as SPMs with the capability to do wafer-level sidewall scanning.

Besides these demonstration in an academic context, the company Vanguard Automation GmbH [164] is providing machines and processes for mass-fabrication of photonic interconnection technology based on additive manufacturing that is partially based on this work. Moreover, the company Vanguard Photonics GmbH [165] offers 3D-printing on various photonic components using processes that are based on this work.

Appendix

A. 3D-printed Lenses and Mirrors for Optical Coupling

The following Appendices A.1 – A.8 are taken from Methods and Supplementary Information of the publication [J3] to *Nature Photonics*. In order to fit the structure and layout of this document, it was adapted accordingly.

P.-I. Dietrich, M. Blaicher, I. Reuter, M. Billah, T. Hoose, A. Hofmann, C. Caer, R. Dangel, B. Offrein, U. Troppenz, M. Möhrle, W. Freude, and C. Koos

[start of Methods and Supplementary Information of publication [J3]*]*

Author contributions

P.-I.D. designed, simulated, fabricated and characterized coupling structures and devices with help from M.Bl., I.R., M.Bi., T.H. and A.H., supervised by C.K. M.Bl. supplied advanced tools and techniques for 3D-printing. M.Bi. and T.H. supported fabrication and measurement of test structures. C.C., R.D. and B.O. contributed to fabrication of test chip elements. U.T. and M.M. contributed InP-based components. Device concepts and coupling schemes were jointly conceived by P.-I.D., M.Bl., R.D., B.O. and C.K. All authors discussed the data. The project was supervised by W.F. and C.K. The manuscript was written by P.-I.D., W.F. and C.K.

A.1 Methods

Simulation: We optimize optical freeform components by simulation with the physical-optics module of the commercial design software ZEMAX [116]. As an input for the various components' simulation, we assume mode fields with rotationally symmetric Gaussian intensity distributions. All mode field diameters (MFD) in the manuscript refer to the $1/e^2$-width of the intensity distribution at a wavelength of 1550 nm. The MFD of the SMF was 10 µm, while the MFD of the edge-emitting laser and the VCSEL were 3.0 µm and 7.5 µm, respectively. For optimization of the lenses, we represent the freeform shape of the

lens surface by a rotationally symmetric polynomial with a height z as a function of the radius

$$r = \sqrt{x^2 + x^2}$$

of the form

$$z(r) = a_0 + a_2 r^2 + a_4 r^4 + a_6 r^6 + a_8 r^8,$$

see Figure 4.3(a) for the definition of the coordinate system. For optimization of the lens surface, we neglect Fresnel reflection as it does not significantly alter the optimal shape while slowing down simulation. The surface is optimized by varying the parameters $a_0 \ldots a_8$ to achieve maximum coupling efficiency for the various configurations.

The surfaces of the reflective elements are defined in a rectangular coordinate system $x_\mathrm{t}, y_\mathrm{t}, z_\mathrm{t}$, where the z_t -axis is tilted by an angle of $45°$ with respect to the optical -axis, see Figure 4.4(c) and (d). The surface of each total internal reflection (TIR) mirror is then represented by a polynomial

$$z_\mathrm{t}(x_\mathrm{t}, y_\mathrm{t}) = \sum_{i=0}^{4} \left(a_{2i} x_\mathrm{t}^{2i} + b_{2i} y_\mathrm{t}^{2i} \right).$$

For simplicity, perfect reflection was assumed for optimization, *i.e.*, the surface was treated as an ideal specular reflector irrespective of the angle of incidence. The surface is again optimized by varying the parameters $a_0 \ldots a_8$ and $b_0 \ldots b_8$ to achieve maximum coupling efficiency for the various configurations.

Fabrication: We print all structures by using the commercial 3D two-photon lithography system Nanoscribe Photonic ProfessionalGT, equipped with a 40x objective lens (numerical aperture 1.4) as well as galvanometer mirrors for rapid beam movement in the lateral directions. The writing distance between subsequent lines and between subsequent layers, often referred to as “slicing and hatching distance,” are both set to 100 nm. The writing speed is adjusted to 10 mm/s. The system is operated with dedicated software, optimized for high shape fidelity of the printed beam-shaping elements and for a high-precision automated alignment with respect to the device facets. In our current experiments, we use standard writing techniques without taking any measures for process acceleration, leading to fabrication times typically 3 … 7 min per lens. By

using the full capacity of current high-speed galvanometer scanners (5000 lines/min for a line length of 40 µm) and by a coarser hatching of the cylindrical parts of the lens, fabrication times of less than 20 s are possible in the future. In addition, operating multiple laser spots simultaneously within the same write field could be an option for parallelizing the fabrication process. In the lithography process, the liquid photoresist (Nanoscribe IP-Dip [118], refractive index n = 1.52) simultaneously acts as an immersion medium for the objective lens. IP-Dip behaves similarly to the published two-photon photoresist IP-L, which contains 7-Diethylamino-3-thenoylcoumarin (DETC) as photoinitiator featuring a two-photon absorption cross-section of approximately [166] 90 GM (non-SI unit "Göppert-Mayer"). For fabrication of our structures, we use an fs-laser with a pulse length of 90 fs (FemtoFiber pro NIR, Toptica) and a repetition rate of 80 MHz. The average power in the rear plane of the objective lens is 12 mW. Glass components and an acousto-optic modulator contribute dispersion so that the pulse is broadened to 150 fs. This leads to a peak power estimate of 12 mW / (80 MHz × 150 fs) = 1 kW. With a half-power beam diameter of 600 nm, the peak intensity in the focus of the beam amounts to 350 GW/cm2.

Coupling experiments with facet-attached lenses: To determine the coupling efficiency from an edge-emitting InP laser (1590 nm, 10.8 mW at 50 mA) to an SMF, we first measure the emission power of the bare laser with an integrating sphere. Where applicable, this measurement was repeated after writing the freeform lens to the laser facet. The laser was equipped with a tapered waveguide and an anti-reflection coating at the facet. The fiber-coupled power was measured using the same integrating sphere as for the measurement of the laser power. The coupling efficiency was determined from the ratio of the two values taking into account the loss of 0.16 dB due to extra Fresnel reflection loss at the plane SMF end facet pointing into the integrating sphere. Alignment tolerance measurements were performed by moving the SMF by steps of 0.5 µm in the horizontal (x) and vertical (y) direction. In axial direction (z), a step size of 4 µm was chosen.

The measured efficiencies were benchmarked to simulations of the respective coupling interface performed by the ZEMAX physical-optics module

software [116]. For beam-shaping lenses attached to the laser facet, a loss contribution of 0.1 dB is caused by residual mode field mismatch, whereas Fresnel reflection at the SMF-air interface contributes an additional 0.2 dB. Moreover, the laser power decreased by 0.4 dB after fabrication of the lens, which can be attributed to reflections at the laser-lens and the lens-air interfaces; see Appendix A.4 for a more detailed discussion. Assuming an ideal lens shape, the best achievable coupling losses for the current devices should hence amount to 0.6 dB. For beam-shaping lenses attached to the fiber facet, the lowest theoretically achievable coupling losses amount to 0.2 dB as dictated by Fresnel reflection at the lens-air facet. Note that the refractive indices of the SMF and the lens are nearly equal such that this interface does not contribute any additional losses. Material absorption within the lenses can be safely neglected – the interaction length within the beam-shaping elements amounts to typically a few tens of micrometers, which is two orders of magnitude below the absorption length of IP-Dip of typically 4.2 cm at a wavelength of 1550 nm, see Figure A5.

Coupling experiments with facet-attached freeform mirrors: For coupling experiments with facet-attached mirrors, we use the same integrating sphere again to measure the free-space and fiber-coupled power levels. Coupling efficiencies are then obtained from the respective power levels by taking into account the extra Fresnel loss of 0.16 dB occurring at the plane SMF end facet pointing into the integrating sphere. The edge-emitting InP laser is again operated at a wavelength of 1590 nm and a free-space output power of 10.8 mW (pump current 50 mA). For the 1550 nm VCSEL, the total output power amounts to 1.0 mW (pump current 17.6 mA).

For the solidified photoresist, we assume the refractive index of n = 1.52 that is specified for the liquid material. This leads to a critical angle of TIR of approximately 41°, measured with respect to the surface normal. For the coupling experiment using a TIR element attached to the edge-emitting InP laser, the large beam divergence may lead to configurations where a certain portion of the emitted light hits the mirror surface at an angle below the critical angle for TIR. This is observed experimentally by measuring the power emitted in the direction of the laser cavity. Incomplete TIR is the main source of loss for such assemblies. This can be overcome by optimized single TIR surfaces, possibly in

combination with refractive surfaces for beam shaping, by cascaded TIR surfaces, by photoresist materials with higher refractive index, or by reflective coatings.

Coupling experiments with facet-attached optical beam expanders: To determine the coupling efficiency from an edge-emitting InP laser to an SMF and a TriPleX chip, we first measure the emission power of the laser-equipped with a lens using an integrating sphere. For coupling from the laser to the SMF, see Figure 4.5(a) and (b), the coupled power was measured by the same integrating sphere as for the measurement of the laser power. The coupling efficiency was determined from the ratio of the two values taking into account the loss of 0.16 dB due to extra Fresnel reflection loss at the plane SMF end facet pointing into the integrating sphere. For coupling from the laser to a TriPleX chip, see Figure 4.5(c) and (d), we measured the power coupled into the triPleX chip using a multimode fiber (MMF) positioned in close proximity at the end of the waveguide that was not equipped with a lens. We checked that light emitted by an SMF is coupled almost perfectly into the MMF. In addition, we accounted for reflection losses occurring at the end of the triplex waveguide and at both ends of the MMF. Alignment tolerance measurements were performed by moving the laser by steps of 0.4 µm in the horizontal (x) and vertical (y) direction. The beam expanders shown in Figure 4.5 consists of one lens directly attached to laser and fiber. The numerical aperture A_{N}/n of the fiber (measured in a medium with refractive index n) is small. As a consequence, the refracting lens surface must be positioned far away from the lens at a distance of at least $L \approx (\mathrm{MFD}/2)/(\mathrm{A_N}/n) = 12.5\mu\mathrm{m}/(0.1/1.5) = 188\mu\mathrm{m}$. This can be overcome by two-lens beam expanders. To determine the coupling efficiency of these interfaces, we use two-lens beam expanders on SMF facets in air. We first perform a back-to-back measurement using a fiber connector and then replace this direct connection by two fibers equipped with identical beam expanders. The coupling loss is measured after optimizing the position of the two SMF. Note that this technique may lead to a slight overestimation of the fiber-to-fiber coupling losses since the coupling experiment features one additional fiber connector compared to the back-to-back reference. The alignment tolerance was measured by moving one fiber on a pre-defined grid by steps of 0.5 µm (4 µm) in the lateral (axial) direction. The MFD between the two expanders operated in air

was designed to an MFD of 23 µm, leading to a theoretically predicted 1-dB coupling tolerance of ±5.5 µm, which is confirmed by experiments.

The coupling experiment was repeated with the expanders designed for operation in an embedding medium. We drop-casted index matching oil with a refractive index $n_0 = 1.47$ onto the coupling interface. Since the oil meniscus between the two SMF was unstable, it was not possible to perform reliable measurements of coupling tolerance, which require time scales up to one hour. The MFD between the expanders operated in an embedding medium was designed to an MFD of 22 µm, slightly smaller than that of the expanders operated in air.

Surface roughness and optical performance: The root-mean-square (RMS) surface roughness of a typical lens is investigated by atomic force microscopy (AFM). To this end, we used a lens printed on a laser facet, see Figure 4.2(A,a). Within a 25×25 µm² area, we measure an RMS surface roughness of 37 nm, see Figure A.1(a). Coupling experiments at a wavelength of 1550 nm indicate that the measured lens roughness does not degrade the coupling efficiency to any significant amount, see Appendix A.3. Root-mean-square (RMS) roughness of the order of 3 nm can be reached by using optimized writing strategies or photoresist with smaller spatial resolution, see Appendix A.2.

High-power damage level measurement: To determine the damage level of beam-shaping elements for high optical powers, we use a lens on an SMF facet, see Figure A2. The fiber is connected to an external-cavity laser operated at 1550 nm, followed by an erbium-doped fiber amplifier (EDFA) that has a maximum output power of 36 dBm. The amplifier is protected by an isolator. Another bare SMF is used to collect the light emitted from the lens, and the coupling efficiency was monitored while increasing the output power in the range (20…36) dBm in steps of approximately 1 dB. At each level, the power was kept constant for at least one minute. At a power of 35.6 dBm (3.6 W), the coupling efficiency degraded abruptly, and the lens disintegrated in a flash of visible light.

A.2 Determination of Surface Roughness by Atomic Force Microscopy (AFM)

Surface roughness is a critical parameter in all printed optical elements. Figure A.1(a) shows the topography of a lens surface measured by atomic force microscopy (AFM). To avoid artifacts, the scan-direction of the AFM was chosen at a 45° angle with respect to the movement of the lithography laser spot during fabrication. The root-mean-square (RMS) roughness of the flattened topography amounts to 37 nm. Smaller RMS roughness of 3 nm can be reached for flat surfaces (Figure A.1(b)). By using optimized writing strategies with smaller slicing distances in the vertical (z) direction also lens surfaces can be fabricated with extremely low roughness.

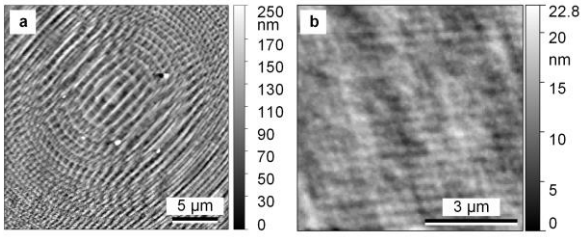

Figure A.1: Atomic force microscopy (AFM) images. A, Surface of a typical lens printed on a laser as in Figure 4.2(b). To flatten the surface, a polynomial was fitted to the measured surface and subtracted from the respective surface. The root-mean-square roughness of the flattened topography amounts to 37 nm. The curvature of the lens was removed from the data by subtracting a sixth-order polynomial surface that was fitted to the measurement data. **B,** Surface fabricated with similar printing parameters. The root-mean-square roughness of the flattened topography amounts to 3 nm.

A.3 Coupling Experiments with Facet-Attached Lenses

Figure A.2 shows the coupling efficiency of two single-mode fibers (SMF) for wavelengths between 1510 nm and 1610 nm, limited by the tuning range of our external-cavity laser. We printed a freeform lens on the facet of SMF1. After optimizing the relative position of the two SMF at a wavelength of 1550 nm, we measure a coupling loss of 0.5 dB (efficiency η = 0.90). The coupling efficiency remains almost constant over the entire wavelength range. Assuming Fresnel-reflection at both the lens-air interface and the air-SMF interface, a residual loss of 0.1 dB could be determined, corresponding to an efficiency η=97.8 %. This value gives an upper boundary for the maximum loss that might be caused by other mechanisms than Fresnel reflection, such as scattering from the lens surface, material absorption, or mode field mismatch.

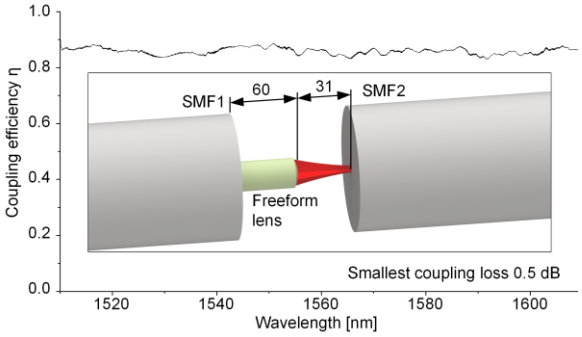

Figure A.2: Measured coupling efficiency between two SMF for wavelengths between 1510 nm and 1610 nm. **Inset:** Schematic of a freeform lens on the facet of SMF1, designed to couple into SMF2. Distances are given in µm.

A.4 Power-Current Curves for Lasers With and Without Lenses

Fabrication of beam-shaping elements to facets of distributed feedback (DFB) lasers does not impact laser performance to a significant degree. This is confirmed by measuring the power-current (P-I-)characteristics before and after lens fabrication, see Figure A.3. The two curves are essentially identical, and we conclude that the lithography beam does not damage the laser facet. The laser facet is anti-reflection (AR) coated with respect to air. The P-I-curve of the laser without lens has a slightly bigger slope than that of the laser with lens, which can be attributed to additional reflections at the laser-lens and the lens-air interface. Moreover, a linear fit indicates a small decrease of lasing threshold after fabrication of the lens. This may be attributed to stronger feedback caused by the reflections at the laser-lens interface. For optimized laser designs, the AR coating should be chosen to minimize reflections at the semiconductor-lens interface. Reflections at the lens-air interfaces can be mitigated by embedding the beam-shaping elements into a cladding medium, thus decreasing the refractive index contrast, see next Section.

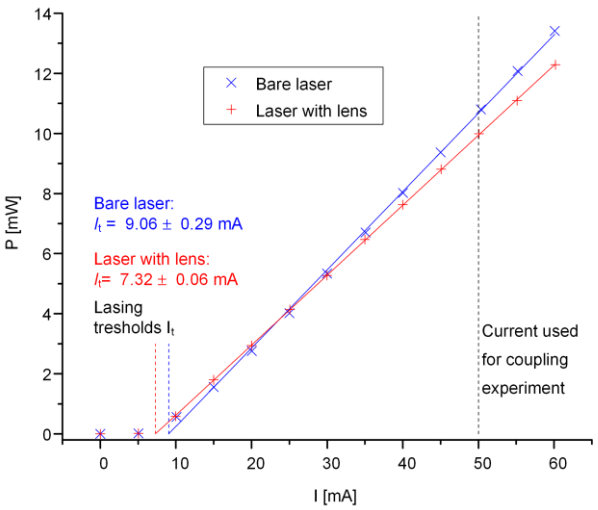

Figure A.3: Power-current measurement for a laser with and without lens. Lines indicate a linear fit of the measured values above the threshold. Printing of the lens to the laser facet leads to a slight decrease of the lasing threshold current I_t, while the power emitted by the laser with and without lens is almost identical at low currents. The slope efficiency of the laser with lens is slightly lower than that of the bare laser.

A.5 Fresnel Reflection in Low-Index Contrast Micro-Optical Systems (LIMOS)

To reduce reflection losses and to protect lenses from environmental influences, the concept of "low-index contrast micro-optical systems" (LIMOS) is introduced. The concept relies on the fact that replacing a single high-index contrast optical interface with a series of cascaded low index-contrast optical interfaces of the same refractive power leads to lower reflection losses. This can be shown by a simplified mathematical analysis. To this end, we neglect the angle-dependence of Fresnel reflection and simply take the power reflection coefficient for perpendicular incidence to a plane surface. We further use paraxial approximation and assume thin lenses along with low index contrast and identical curvature radii of all lenses. For quantifying the loss, we sum up the Fresnel reflections at all interfaces, *i.e.*, our model does not account for interference effects between lens surfaces. We derive simple analytic formulae that indicate the relation between the refractive index of an embedding medium, the required number of optical interfaces for a certain refractive power, and the associated reflection losses.

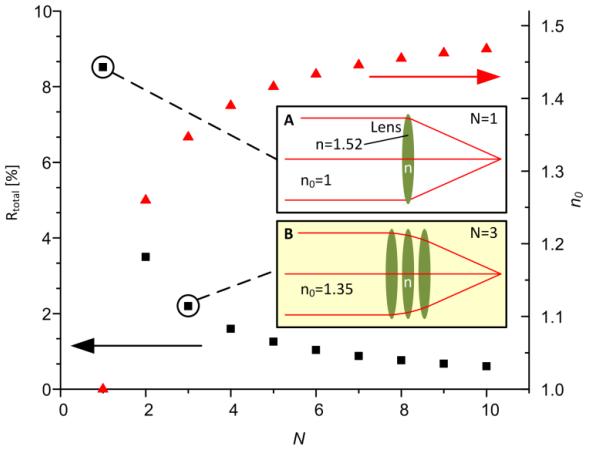

Figure A4: Calculated total Fresnel reflection losses R_{total} and associated refractive index n_0 of cladding medium for cascades of one to ten lenses that achieve the same refractive power as a single lens operated in air. The analysis refers to a lens material with a refractive index of n = 1.52. Insets: Schematic drawing of a lens operated in air (A) and of the equivalent three-lens cascade in a low-index cladding (B).

The Fresnel power reflectivity R for perpendicular incidence at an optical interface with refractive index n embedded in a homogenous medium with refractive index n_0 is given as

$$R = \frac{(n - n_0)^2}{(n + n_0)^2}. \qquad \text{(A.1)}$$

Assuming spherical lenses with curvature radius r, the focal length f can be written as

$$f = r\frac{n}{n - n_0} \tag{A.2}$$

when light comes from a region with n_0. For a cascade of N low index-contrast lenses, with two optical interfaces each, the reflectivities can be added so that the total reflection loss is approximately given by

$$R_{\text{total}} = 2NR\,. \tag{A.3}$$

Assuming thin lenses, the total focal length f_{total} of a cascade of lenses is given as the reciprocal sum of the individual focal lengths. If these focal lengths are equal, $f_i = f$, the total focal length f_{total} of the lens assembly is given by

$$f_{\text{total}} = \left(\sum_{i=1}^{N}\frac{1}{f_i}\right)^{-1} = \frac{f}{N}\,. \tag{A.4}$$

For comparing equivalent lens assemblies, we stipulate that the focal length f_{Total} of a single lens in air is identical to that of a cascade of N identical lenses in an embedding medium with refractive index n_0. Inserting Eq. (A.2) into Eq. (A.4) allows calculating the refractive index n_0 of the embedding medium that is required to achieve this,

$$n_0 = n - \frac{1}{N}(n-1). \tag{A.5}$$

The result in Eq. (A.5) is identical when assuming biconvex lenses in Eq. (A.2) or when assuming that light comes from a region with a refractive index n. The total Fresnel reflectivity of the lens cascade can be estimated by inserting Eqs. (A.1) and (A.5) into Eq. (A.3),

$$R_{\text{total}} = 2N\frac{\left(\frac{n-1}{N}\right)^2}{\left(2n - \frac{n-1}{N}\right)^2}. \tag{A.6}$$

Assuming n=1.52, we can plot the total Fresnel loss R_{Total} vs. the number of lenses N, see Figure A.4. The refractive index of the embedding medium n_0 is adjusted accordingly to Eq. (A.5) and is shown in red. We find that for a given refractive power of the overall lens system, the total Fresnel losses can be reduced by increasing the number of lens surfaces while decreasing the index contrast at each surface. The insets in Figure A4 show a comparison of a lens operated in air and three lenses operated in an embedding medium with n_0 = 1.35. In this case, losses would reduce from 9 % for the lens in air to 2 % for the three-lens cascade operated in an embedding medium.

A.6 Absorption Measurement of Photoresist

To estimate material absorption of the liquid and solid photoresist IP Dip, we performed an absorption measurement in a UV-transparent plastic cuvette (Brand GmbH & Co KG, "UV-cuvette semi micro") with a geometrical path length of 4 mm inside the cuvette. As a light source, we used a deuterium lamp (250 nm – 319 nm) or a tungsten-halogen source (319 nm – 2500 nm), filtered by a monochromator (PerkinElmer, LAMBDA 950 UV/Vis Spectrophotometer) with a spectral resolution of 1.25 nm in the UV/VIS region from 250 nm to 861 nm, and of 5 nm in the IR region from 861 nm to 2500 nm. The cuvette is mounted in an integrating sphere at an angle with respect to the direction of the incident light beam to avoid specular reflection out of the integrating sphere. Photodetectors inside the integrating sphere measure the total light power in the sphere. As a reference, we measure the absorption spectrum for an air-filled cuvette. For solidifying the

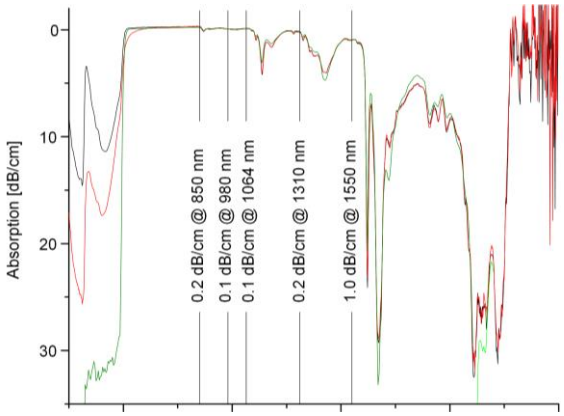

Figure A5: Measured absorption of the photoresist IP-Dip. Measurements were performed with a plastic cuvette in an integrating sphere for liquid (——, black) and cured (——, red) material, and in transmission with a quartz cuvette filled with liquid photoresist (——, green). The absorption at five technically important wavelengths is specified. All three measurement series coincide at these wavelengths. The loss in the telecommunication C-band around 1550 nm is below 1.0 dB/cm.

photoresist, we use a UV-source at 365 nm (Dymax RediCure) in a nitrogen atmosphere with a dose that suffices to cure the material. The measured absorption data are depicted in Figure A5 (black and red curves). As we expect high fluorescence for wavelengths below 500 nm, we complemented the absorption measurement in the integrating sphere by a transmission measurement of the liquid photoresist in a fused-silica cuvette placed outside the integrating sphere Figure A5 (green curve). The geometrical path length inside the cuvette is 9 mm. Again we reference our measurement to an air-filled cuvette and compute the resulting absorption. Different power reflection factors due to reflection at the sidewalls of the empty quartz cuvette in the reference measurement are accounted for numerically. Apart from the wavelengths below 500 nm, the transmission (quartz cuvette) and absorption measurement (plastic cuvette and integrating sphere) coincide. Figure A5 also gives specific absorption loss values at the five technically relevant wavelengths of 850 nm, 980 nm, 1064 nm, 1310 nm, and 1550 nm – in all these, the absorption is below 1 dB/cm, leading to negligible absorption losses of less than 0.025 dB for a 250 µm-long device. Note that even the highest measured absorption of around 32 dB/cm in the full wavelength range from 250 nm to 2500 nm would lead to absorption below 0.8 dB for a typical device length of 250 µm.

A.7 Coupling to TriPleX Chips

Figure A.6 shows scanning electron microscopy (SEM) images of 3D-printed lenses on the facets of TriPleX chips. The TriPleX chips used on our coupling experiments feature diced unpolished facets which exhibit significant roughness, see Inset of Figure A.6(a). The rough waveguide facets lead to optical distortions of the emitted mode fields and hence to reduced coupling both for the case with and without facet-attached lenses. We also tried to measure the mode field at the facet of the TriPleX waveguide using an IR camera with a high-NA lens (100X, NA=0.8), see Figure A.6(b). A Gaussian fit to the measurement data reveals a mode field diameter of 8.0 µm in x-direction, Figure A.6(c), and 6.8 µm in y-direction, significantly deviating from the specified mode field diameter (MFD) of approximately 11 µm. We believe that these deviations are part of the origin of the excess losses 2.5 dB observed in the laser-to-TriPleX chip coupling experiment for perfect position and tilt alignment. We expect that better facet preparation can reduce the coupling losses to less than 1 dB and increase the alignment tolerances to more than ± 5 µm.

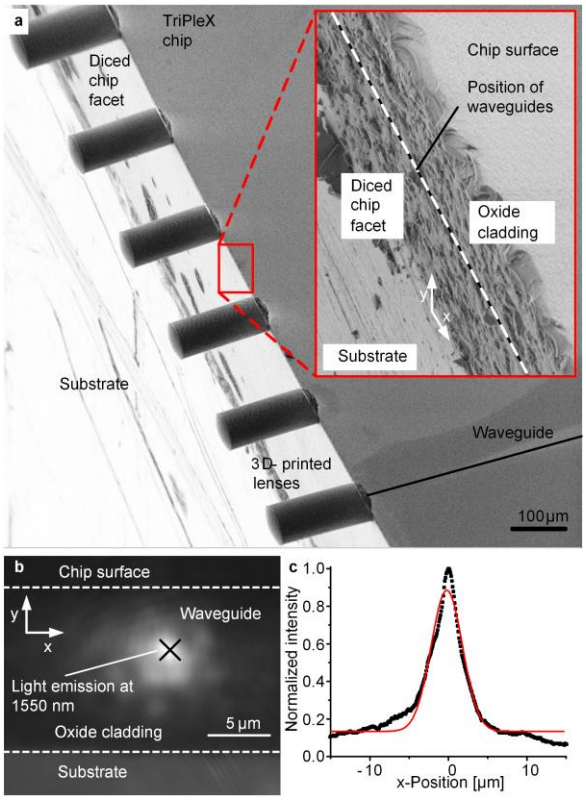

Figure A.6: Beam shaping elements at the facet of a TriPleX-chip. **A**, Electron-microscopy image of lenses fabricated on the chip facet. Inset: The chip facet is not polished and shows surface roughness. **B**, Mode field of light emitted from the TriPleX waveguide facet, measured by an infrared (IR) microscope. **C**, A Gaussian fit to the highly distorted mode field reveals a mode field diameter of 8.0 µm in x-direction (depicted) and of 6.8 µm in y-direction (not depicted).

A.8 Reproducibility and Accuracy

To demonstrate the reproducibility of our printing method, we fabricate eight nominally identical lenses, which are written on two SMF arrays with four fibers each. In these experiments, we deliberately chose SMF arrays as well-defined and particularly reproducible test vehicles that allowed us to investigate only the impact of shape variations of the facet-attached lenses and to exclude additional effects caused by non-perfect facets or waveguides. All lenses have a length of 190 µm and a diameter of 80 µm and are designed to expand the SMF MFD of 10 µm at a wavelength of 1550 nm to a beam waist with an MFD of 25 µm at a distance of 100 µm from the lens apex. We perform 16 coupling experiments, measuring all possible lens combinations by individually optimizing the relative position and tilt of each pair of lenses. The resulting coupling losses are indicated in Tab. A.1.

Table A.3 Coupling losses in dB of lenses four lenses denoted as a ... d on a first fiber array to four lenses denoted as 1 ... 4 on a second fiber array. Underlined values indicate measured losses when iteratively optimizing the coupling efficiency of lens pairs a,1 and d,4. All other values are obtained after individually optimizing the relative position and tilt of each lens pair.

Lens	1	2	3	4
a	0.56/0.51	0.55	0.51	0.56
b	0.53	0.56/0.54	0.54	0.56
c	0.51	0.51	0.50/0.51	0.55
d	0.56	0.51	0.52	0.63/0.55

We find an average coupling efficiency of 88 % (coupling loss 0.55 dB) with a standard deviation of ± 0.4 % (coupling uncertainty ± 0.02 dB). Subtracting the Fresnel losses of the two lens-air interfaces, we achieve an average coupling efficiency of 97 % (coupling loss 0.13 dB). This residual loss is attributed to an additional FC/APC connector that was introduced in the beam path for the coupling experiment but was not used for the reference measurement. We further perform a second experiment in which we align the two outer lens pairs of the array for optimum coupling efficiency. To this end, we iteratively optimize the coupling efficiency of the lens pairs a,1 and d,4 using all translational and rotational degrees of freedom. We find negligible penalties when optimizing the coupling efficiency of both lens pairs simultaneously in comparison to

individually optimized efficiencies, see Table A.1. We then measure the coupling loss for the remaining lens pairs b,2 and c,3 without further optimization. The results are indicated as underlined numbers in Tab. S1. We achieve coupling losses between 0.5 dB and 0.6 dB, demonstrating the precision of the lens pitch and of the emission direction.

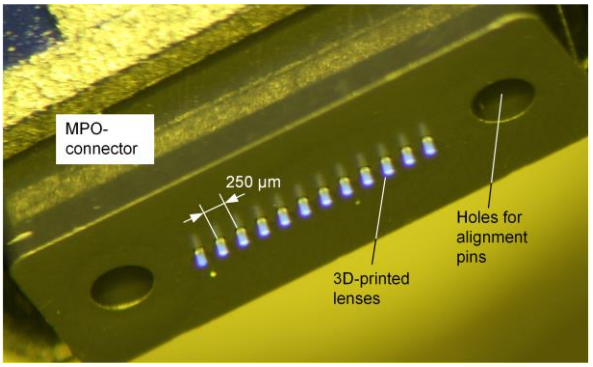

Figure A.7: Microscope image of twelve lenses printed on the facets of a multipath push-on (MPO) connector.

To demonstrate the versatility and reproducibility of the concept, we additionally fabricate 24 lenses on two multipath push-on plugs (MPO) connectors, see Figure A.7. The lens design is the same as the one of the previous experiment. We again align the two outer lenses of the first array for optimum coupling to those of the second arrays and then measure the coupling efficiency of all lens pairs without individually optimizing the relative positions. We find an average coupling efficiency $\eta = 84$ % (coupling loss of 0.75 dB) and a standard deviation of $\sigma_\eta = 2$ % (coupling uncertainty ± 0.09 dB). This loss includes two additional MPO connectors and one FC/APC connector that was not present in the reference measurement. We believe that the biggest part of the coupling uncertainty and a fraction of 0.4 dB of the measured coupling loss can be attributed to these connectors. These results indicate that the envisaged facet-attached microlenses can be fabricated in large quantities and with high reproducibility, as required for large-scale fabrication of hybrid photonic systems.

[end of Methods and Supplementary Information of publication [J3]*]*

B. 3D-printed Functional Microsystems

The content of the following Appendices B.1 to B.8 are taken from Methods and Supplementary Information of the publication [J2] to *Small*. In order to fit the structure and layout of this document, it was adapted accordingly.

Philipp-Immanuel Dietrich, Gerald Göring, Mareike Trappen, Matthias Blaicher, Wolfgang Freude, Thomas Schimmel, Hendrik Hölscher, Christian Koos

[start of Methods and Supplementary Information of publication [J2]*]*

B.1 Architecture and Optical Design of the Printed SPM Engine

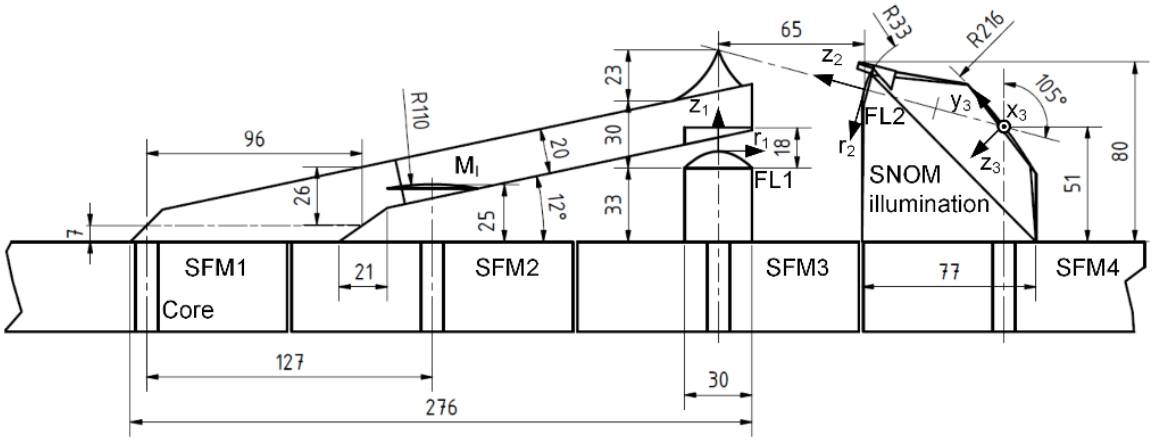

Figure B.1: Cross-section of the SPM engine in Figure 6.1. Dashed lines indicate optical axes of the various optical beams. For simplicity, we indicate radii of curvature of aspherical surfaces; they represent approximations of polynomial freeform surfaces. Dimensions are indicated in µm.

A cross-section of the scanning probe microscopy (SPM) engine in Figure 6.1(a) is depicted in Figure B.1, giving details of the geometrical dimension. The SPM engine is printed onto the facets of an array of four single-mode fibers (SMF). We omit the mirror shielding for clarity (Figure 6.1(b)). Light is emitted from the fiber facet of SMF2 towards a concave freeform mirror M_I at the bottom surface of the cantilever, designed for focusing a portion of the light back into the fiber core. We design mirror MI with spherical shape and adjust the

radius of curvature such that the optical amplitude of the light coupled back into the fiber core is matched to the Fresnel reflection at the inside of the planar fiber facet. For SNOM operation, light must be collected from the SPM tip. To this end, we use a first freeform lens (FL1) on SMF3. We modeled the shape of this lens by a parabola of the form $z_1(r_1) = ar_1^2$, see Figure B1 for the definition of the coordinate system, where r_1 is the radial distance from the optical axis z_1. The surface is optimized by varying the parameters a to achieve maximum coupling efficiency to SMF3 when assuming a Gaussian beam with an axis z_1 having a waist with a 4 µm diameter at the AFM tip. This value was chosen as a compromise between collection efficiency and tolerances with respect to fabrication inaccuracies. The shape of the second freeform lens (FL2) and of the freeform mirror of the SNOM-illumination on SMF4 were designed by optimizing the coupling efficiency to a Gaussian waist with a 10 µm mode field diameter and a phase front perpendicular to the axis z_2, again located at the AFM tip. Also here, the mode field of 10 µm was chosen as a compromise between illumination intensity and tolerances with respect to fabrication inaccuracies. To this end, we varied the parameter b of the parabola $z_2(r_2) = br_2^2$, describing the lens surface, as well as c and d_1, d_2 of the polynomial describing the mirror surface $z_3(x_3, y_3) = cx_3^2 + d_1y_3^2 + d_2y_3^4$. For the simulation, we used a commercial simulation package (OpticsStudio, Physical Optics Propagation Module, Zemax LLC, USA). All optimizations were performed for a wavelength of 1550 nm; see Appendix 6.1 for a complete description of the operation principle.

B.2 Simulation and Measurement of Cantilever Deformation

When operated at resonance, the dynamic deformation of the cantilever slightly differs from the bending that is induced by a static force acting at the tip [167]. Therefore, a static calibration, as depicted in Figure 6.1(c), cannot be directly used to quantify the tip movement at resonance if the readout position is not at the tip position. To account for this deviation between static and dynamic behavior, we simulate the deformation of the cantilever both in the static case and at resonance using the finite-element (FEM) software COMSOL Multiphysics. For simplicity, we omit the optics above SMF2 and SMF3 and model the cantilever with a smooth bottom surface. In the simulation, we assume a density of $\rho = 1.02$ g/cm³ and a Poisson ratio of 0.45, as specified for cross-linked IP-Dip [168]. The Young's Modulus amounted to $E = 3.3$ Gpa and was determined by the measurement of the resonance frequency (Figure 6.1(d)) of the cantilever followed by a simulation. This procedure is required, as literature values for the Young's Modulus of IP-Dip differ significantly depending on fabrication parameters and exposure doses. To further characterize static and dynamic movements of the cantilever, we defined the displacement ratio (DR) that relates the displacement Δz_M of mirror M_I above SMF2 to the tip displacement Δz. From our simulation of the cantilever movement, we find a static DR of $DR_{stat,sim} = 13.6$, which is in good agreement with the measured static displacement ratio $DR_{stat,meas}$ of 13.4, see

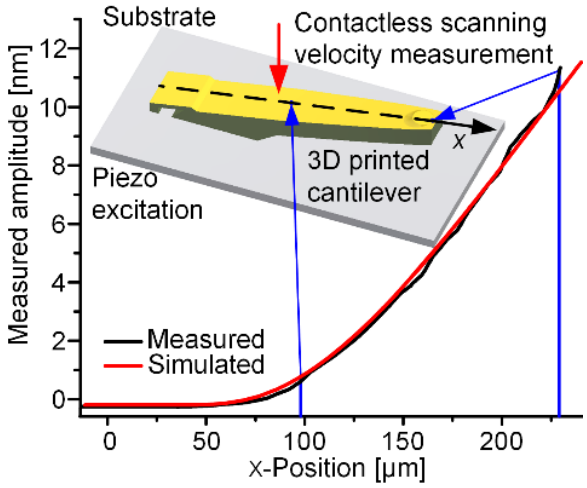

Figure B.2: Dynamic bending profile of the cantilever at maximum amplitude when excited with a piezoelectric actuator, measured with a scanning vibrometer. The red curve indicates a simulation of the cantilever bending, and the black curve represents data that was extracted from the vibrometer measurement. Inset: Model of the cantilever. The laser is indicated by a red arrow. To scan the laser along the cantilever surface, the substrate is moved with respect to the laser.

Appendix B.3. We checked by simulation that the induced bending of the cantilever and the associated tilt of the surface of mirror M_I has no significant influence on the reflectivity, *i.e.*, the power reflection back into the fiber SMF core changes by less than 1 %.

We additionally simulate the dynamic displacement ratio $|\delta z|/|\delta l_C|$ at resonance, which we find to be $DR_{dyn,sim} = 11.8$. To verify this simulation, we measure the cantilever oscillation by means of a high-speed scanning vibrometer (MSA-050 Micro System Analyzer, Polytec GmbH, Germany). In this experiment, we use a simplified cantilever structure without a tip that we print onto a planar substrate; see Appendix 0 for details on design and fabrication. The substrate is then mounted onto a piezo mechanic actuator for excitation of oscillations close to the resonance frequency of 191 kHz. The vibrometer allows measuring amplitude and phase of the cantilever oscillation on a 5 µm lateral grid. Figure B.2 shows the space-dependent oscillation amplitude measured along the centerline of the cantilever along with the results of a COMSOL simulation.

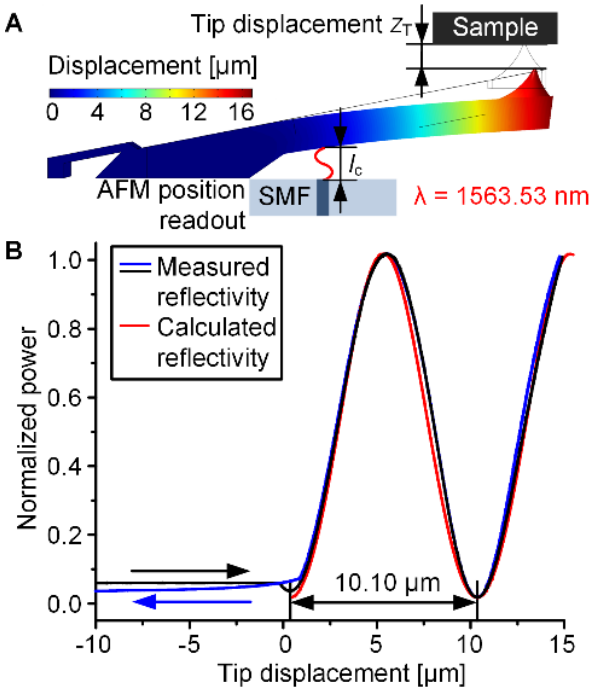

Figure B.4: Calibration of the interferometric AFM position detector. A, Simulated deformation of the cantilever caused by a static displacement of the tip The static displacement ratio of $DR_{stat,sim}$ amounts to 13.6. **b,** Measured power reflection of the interferometric position sensor as a function of tip displacement. The tip displacement was varied by adjusting the distance between the SPM engine and the sample surface using a closed-loop piezo positioner. The period of the observed reflection pattern can be used to deduce the associated movement of mirror M_I. we find a measured displacement ratio of $DR_{stat,meas} = 13.4$, close to its simulated counter-

The simulated displacement ratios in the dynamic ($DR_{dyn,sim}$) and the static case ($DR_{stat,sim}$) can be used to calculate the tip movement at resonance (Figure 6.1(d)). To this end, we assume that the dynamic oscillation patterns at resonance do not depend on the excitation and that hence the dynamic oscillation

amplitude for optical excitation is also by a factor of $DR_{stat,sim}/DR_{dyn,sim}=13.6/11.8=1.15$ larger than the static calibration (Figure 6.1(C)) would indicate. Base on this, we estimate a tip oscillation amplitude of 24 nm for the case of optical excitation (Figure 6.1). Moreover, we performed a simulation to evaluate the spring constant of the AFM- and SNOM type cantilever. To this end, we perform a simulation where the cantilever is deformed by applying a force of 1 µN acting in *z*-direction onto the tip (Figure 6.1 and Figure 6.2). The associated displacement of the tip was simulated using a commercially available finite-element package (Autodesk Inventor, Autodesk Inc., USA). For the AFM-cantilever (Figure 6.2), we found a spring constant of c_{AFM} = 12 N/m, whereas the thick SNOM-cantilever exhibits a value of c_{SNOM} = 64 N/m.

B.3 Characterization of the AFM Position Detector

To characterize the position sensor connected to SMF2 (Figure 6.1), we use a tunable external-cavity laser and an optical spectrum analyser (AQ6317B, Ando Electric Co., Ltd, Japan) acting as a power meter with a synchronously swept optical filter to measure the wavelength-dependent back-reflection of the interferometric position detector in a wavelength range between 1520 nm and 1620 nm (Figure B.3). As a reference, we first measure the reflection of an Au-coated fiber reflector, which is then replaced by SMF2 and the associated position detector. To estimate the absolute value of the reflection factor, we assume that the Au-coated reference fiber facet has perfect reflection. As both the SMF-air interface and cantilever-air interface have a low reflectivity of 3.6 % and 4.4 %, respectively, we may consider the position sensor as a two-wave interference and neglect multiple reflections. The measured wavelength-dependent power reflection factor can hence be fitted by a model function of the form $R(\beta, l_c) = 4R_0 \sin^2(\beta l_c)$, where $\beta = 2\pi / \lambda$ is the free-space propagation constant of the emitted light and where lc is the geometrical distance between the SMF facet and the surface of mirror MI (Figure 6.1). The quantity R0 denotes the power reflection factor of the SMF facet, which is assumed to be identical to the effective power reflection factor from mirror MI into the SMF core. From this fit, we estimate a distance of

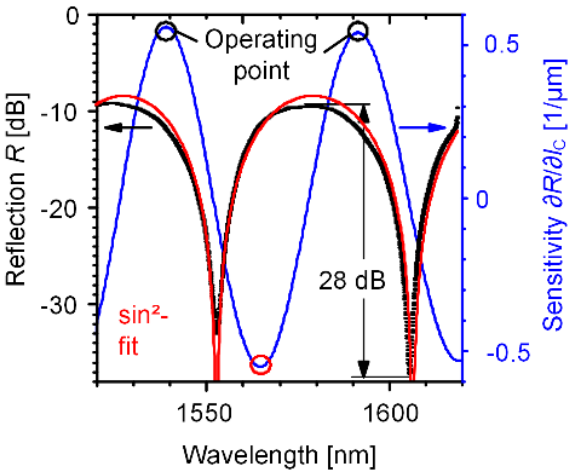

Figure B.3: Reflectivity (black) of the AFM position readout as function of readout laser wavelength. Unity power reflection (0 dB) corresponds to an Au-coated fiber reflector that we use as a reference. We achieve extinction ratios of up to 28 dB, indicating accurate design of the mirror M_I, see Figure 5.1. A sin²-shaped model function (red) is fitted to the measurement data to estimate the wavelength-dependent sensitivity (blue) of the power reflection factor with respect to the distance l_C between the mirror M_I and the facet of SMF2. Operating points of maximum sensitivity are indicated by black and red circles; the red circle denotes the operating point that is typically used in our experiments.

lc = 23.3 µm, which is only 1 µm below the designed value of 24.3 µm. The deviation of 1 µm is attributed to a vertical offset in the positioning of the printed structure with respect to the surface of the fiber facet. The interferometric position sensor exhibits an extinction ratio of 28 dB, indicating that the coupling efficiency of the freeform mirror into the SMF matches indeed well to the reflection of light from the inside the SMF facet. From the fit, we can also deduce the dependence of R on Δz_M by taking the derivative $\partial R/\partial z_m$. We can then identify favorable operating wavelengths that maximize the sensitivity of the displacement measurement, indicated by black and red circles in Figure B3. In these operating points, the power reflection factor corresponds to the mean of the minimum and the maximum value. The measured mirror displacement in Figure 6.1(c) was acquired in such an operating point, assuming an approximately linear relationship between the mirror displacement Δz_M and the change ΔR of the power reflection factor. The ratio of the tip displacement and the displacement of mirror M_I, can be directly deduced from the static displacement ratio of $DR_{stat,meas} = |\Delta z / \Delta z_M| = 13.4$ (Figure 5.1I). This value is in excellent agreement with the simulated $DR_{stat,sim}$ of 13.6 (Figure B.4(a) and Appendix B.2). To confirm that the position sensor signal may indeed be evaluated by a linear approximation about an operating point, we repeat the measurement depicted in Figure 5.1(c) with a much larger tip displacement of approximately 15 µm, which reveals the interference fringes in the read-out signal (Figure B.4(b)). By observing two maxima of the interferometric position sensor, we can again determine the absolute displacement of the mirror and compare it to the tip displacement, thereby obtaining a second displacement ratio of $DR'_{stat,meas} = |\Delta z / \Delta z_M| = 12.4$ between tip and readout mirror in the static case. The value of $DR'_{stat,meas}$ for the large-range displacement, agrees reasonably well with its counterpart obtained for small displacements and is only slightly smaller than the simulated value of $DR_{stat,sim}$ of 13.6, see Section B.2.

B.4 Thermo-Mechanical Simulation and Modeling

To study the dynamic behavior of our SPM engine system upon optical actuation, we perform an experiment in which we feed a step-like optical excitation to the AFM actuator while measuring the displacement of the cantilever by the

interferometric AFM position detector. For adjusting the operating point of the position detector in the experiment, we again tune the read-out wavelength of the position detector over a wide range to observe maxima and minima of the wavelength-dependent power reflection spectrum (Figure B3 and Appendix B.3). We then adjust the wavelength to an operating point of maximum sensitivity, for which the power reflection factor corresponds to the mean of the minimum and the maximum value, indicated by red respectively black circle in Figure B3. The rise time of the excitation step function in the experiment was approximately 50 µs – much shorter than any of the time constants associated with the mechanical movement of the structure that we describe in the following. The measured displacement is depicted as a black trace in Figure B5, indicating the time-dependent change $\Delta l_{C,meas}$ of the measured distance l_C between the facet of SMF2 and the surface of mirror M_I. We observe a slight initial overshoot of the step response and a subsequent reduction of the displacement for $t \geq 1.16$ ms. This behavior is attributed to the dynamics of heat influx and subsequent heat spreading within the structure: The steep initial increase of the displacement is caused by heating of the top side of the cantilever adjacent to the irradiated Cr/Au layer, while the bottom part is still at its initial temperature. The heat distribution then spreads out and finally reaches the lower surface of the cantilever, thereby reducing the temperature gradient across the local cantilever cross-section. This leads to partial relaxation, finally reaching an equilibrium and a stationary temperature distribution across the structure.

To confirm this explanation, we perform a simulation using COMSOL's Heat Transfer Module and Solid Mechanics Module. A crucial parameter to reproduce the measured results is the thermal contact conductance h_c between the polymer structure of the SPM engine and the underlying silica fiber array. We find a thermal contact conductance $h_c = 3.5 \cdot 10^4$ W/K/m² to give best agreement between simulation and experiment, see green curve in Figure B5. In our simulations, we modeled the material of the 3D-printed structure as acrylic plastic, as given in the COMSOL material library, and changed the thermal expansion coefficient according to literature values of IP-Dip [169] to $5 \cdot 10^{-5}$ 1/K. The simulation also includes heat dissipation by irradiation and by thermal flux to air. For thermal excitation of the structure, we assumed a Gaussian distribution of the heating power P_H incident on the cantilever surface from below. The $1/e^2$-diameter of the power distribution was assumed to be 17 µm, corresponding to

the $1/e^2$ mode field diameter (MFD) of the optical intensity distribution associated with the exciting beam at a wavelength of 1550 nm. To approximately reproduce the displacement magnitude observed in the experiment, the heating power was adjusted to $P_H = 0.7$ mW. According to a separate wave-optical simulation with COMSOL, this heating power corresponds to an estimated optical power of approximately 2.9 mW that is incident at a wavelength of 785 nm on the metal layer on the top surface of the cantilever. The metal layer consists of approximately 5 nm chromium (Cr) and 100 nm gold (Au), and the absorption is mostly caused by the Cr layer directly adjacent to the polymer cantilever. Note that the estimated optical heating power of 2.9 mW is significantly smaller than the approximately 10 mW emitted from the fiber pigtail of the actuator laser into SMF1. We attribute the discrepancy to optical losses at the transition of the fiber pigtail of the laser (Nufern 780HP, core diameter 4.4 µm) and SMF1 (OFS AllWave Flex ZWP, core diameter approximately 10.0 µm) as well as to uncertainties of the Cr and Au layer thicknesses. We also qualitatively confirm the impact of the temperature gradient across the cantilever cross-section by investigating the temporal evolution of the heat distribution – Inset 1 of Figure B5 refers to the reversal point (P_1, t = 1.16 ms) of the simulated step response, while Inset 2 indicates the temperature distribution at during relaxation to thermal equilibrium (P_2, t = 3 ms).

For the simulation of the amplitude and phase of the tuning curve (Figure 6.1(d)), we start from the simulation model described above and expand it by introducing a sinusoidal temporal variation of the heating power and by including the damping parameter of the polymer. To this end, we first estimate the mechanical Q-factor of the cantilever by fitting a simple Lorentzian function to the amplitude of the measured resonance and find $Q = 10.4$. We then calculate the intrinsic loss parameter of the cantilever material from the mechanical Q-factor using the relation $\eta = 1/(2Q) = 0.048$. This value is in good agreement with expectations for typical polymers [143]. The low quality factor is typical for cantilevers made from polymers and allows for fast scanning, which may be inferred from the so-called material-bandwidth product [143], which amounts to 86 in our case. Using the extracted intrinsic loss parameter of the material in the simulation allows to reproduce the red traces for the amplitude, and the green trace for the phase response plotted in Figure 6.1. In these simulations, we additionally adjusted the amplitude and Young's modulus to match the

measured data. For the measured phase, we compensate a delay of the digital signal processing in the measurement system of 2.2 µs to obtain the green curve in Figure 5.1(d).

For fitting the measured frequency-dependent amplitude response $a(f)$ shown in Figure 5.3(b), we use a model function of the form

$$a(f) = A_0 + \left(\frac{A_1}{\sqrt{(f - f_\mathrm{r})^2 + (\Delta f_\mathrm{FWHM}/2)^2}} \right) \exp\left(A_3 \sqrt{f} \right) \qquad \text{(B.1)}$$

with a constant offset A_0, a scaling factor A_1, the resonance frequency f_r and the full width at half maximum Δf_FWHM, as well as a parameter A_3 related to thermal excitation as fit parameters. This model consists of a Lorentzian, representing the fact that the cantilever represents a harmonic mechanical oscillator, along with a frequency-dependent mechanical excitation of the form $\exp\left(c_1 \sqrt{f}\right)$ caused by the low-pass characteristics of the thermo-mechanical oscillation. To approximate these low-pass characteristics, we start from the general solution of the thermal energy density distribution $u(\mathbf{r},t)$ in a homogeneous medium upon excitation with a heating power density [170] $p(\mathbf{r},t)$,

$$u(\mathbf{r},t) = \int_{0}^{t} \int_{-\infty}^{\infty} h(\mathbf{r} - \mathbf{r}_0, t - t_0)\, p(\mathbf{r}_0, t_0) \mathrm{d}^3\mathbf{r} \mathrm{d}t_0, \qquad \text{(B.2)}$$

where the heat kernel $h(\mathbf{r},t)$ represents the fundamental solution to the heat equation upon an impulse-like excitation in space and time,

$$h(\mathbf{r},t) = \frac{1}{(4\pi a t)^{3/2}} \exp\left(-\frac{|\mathbf{r}|^2}{4at} \right). \qquad \text{(B.3)}$$

Disregarding the impact of the exact 3D heat distribution on the mechanical expansion of the cantilever, the temporal transfer function can be approximated by taking the Fourier transform of the heat kernel in Equation (B.3) with respect to time,

$$\tilde{h}(f) = A_4 \exp\left(A_3 \sqrt{f} \right). \qquad \text{(B.4)}$$

In this relation, A_3 and A_4 represent time-independent parameters that may still depend on space. A_4 is merged into A_1 in Equation (B1).

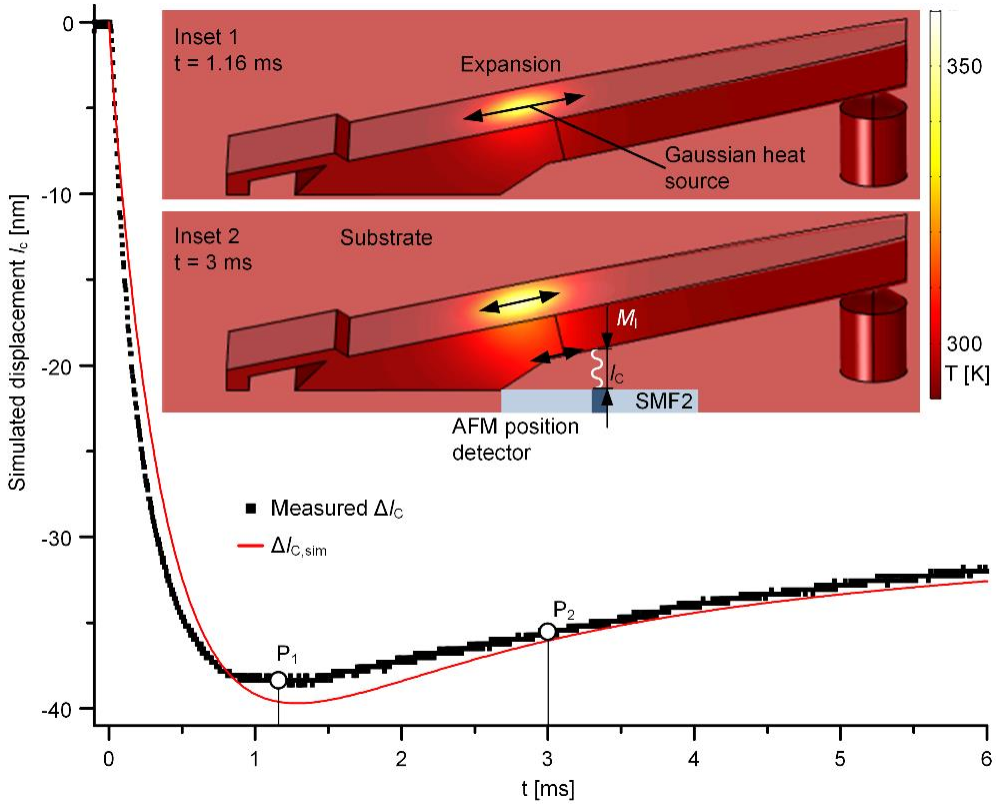

Figure B.5: Measured (black) and simulated displacement (red) response of the SNOM-type cantilever for a step-like opto-thermal excitation. The quantity Δl_C corresponds to the vertical displacement of mirror M_l. As an excitation, we assume a Gaussian distribution of the heating power incident on the cantilever surface from below. The $1/e^2$-diameter of the power distribution was assumed to be 17 µm, corresponding to the $1/e^2$ mode field diameter (MFD) of the optical intensity distribution associated with the exciting beam. Both the simulation and the measurement indicate a slight Initial overshoot of the step response and a subsequent reduction of the displacement for $t \geq 1$ ms. The steep initial increase of the displacement is caused by heating of the top side of the cantilever adjacent to the irradiated Cr/Au layer, while the bottom part still is at its initial temperature, see Inset 1. The heat distribution then starts to spread out and finally reaches the lower part of the cantilever, thereby reducing the temperature gradient across the local cantilever cross-section, see Inset 2. This leads to partial relaxation, finally reaching an equilibrium which is given by the stationary temperature distribution across the structure. **Inset 1:** Temperature distribution at maximum displacement (point P_1, t = 1.16 ms), featuring a strong temperature gradient between the hot upper surface of the cantilever and its lower surface. **Inset 2:** Temperature distribution as the heat spreads across the structure of the cantilever (point P_2, t = 3 ms). The associated reduction of the temperature gradient across the cantilever leads to a relaxation of the cantilever displacement. For $t \rightarrow \infty$, the cantilever displacement converges to a constant steady-state value.

B.5 Highly Sensitive Position Readout

The sensitivity of the AFM position readout can be increased by using highly reflective mirrors to increase the optical Q-factor of the underlying Fabry-Pérot cavity. Such cavities could be used for highly sensitive AFM measurements, e.g., in a temperature-controlled vacuum environment. Higher Q-factors cannot be achieved by utilizing a bare single-mode fiber (SMF) facet, as the Fresnel flection at the SMF (typical < 4 %) is too low. To overcome this limitation, we cover the fiber array with a thin semi-transparent Au layer (Figure B.6(a)). Together with the Au-covered curved mirror surface at the cantilever, the coating of the SMF facet allows increasing the optical Q-factor to values well in excess of 1000 (Figure B.6(b)). The Au thickness amounts to 20 nm at the SMF facet and to 70 nm for the top coating of the cantilever. Note that we did not use a Cr adhesion layer, neither at the SMF facet nor at the cantilever, since this would cause high absorption. Note also that the rather low extinction ratio of the dips in the power reflection factor, as shown in Figure B.6, can be increased by optimizing the reflectivity of the semi-transparent Au layer on the fiber facet.

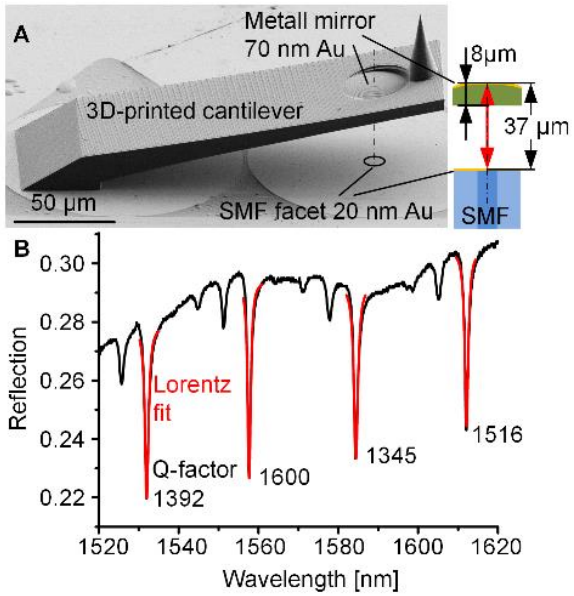

Figure B,6: Cantilever with high-Q optical cavity for sensitive position read-out. A, Scanning electron microscope (SEM) image of the cantilever on a single-mode fiber (SMF) array. **Inset:** Cross-section of the Fabry-Pérot cavity formed by the Au-coated SMF facet and the Au mirror on top of the cantilever. The top surface of the cantilever and the SMF facet are coated with 70 nm thick and 20 nm thick Au layers. **B,** Reflectivity of the cavity for different wavelengths. The Q-factor has been determined by individual Lorentzian fits (red) and is indicated for every dip.

From Figure B.6(b), we can extract the free-spectral range between the resonance dips, which indicates an optical cavity length of 46 µm. The cavity length was designed to a geometrical length of 37 µm. Considering 8 µm of light

propagation inside the cantilever with n = 1.53, this amounts to an optical path length of 41 µm. The difference of 5 µm between measured and calculated optical cavity length is attributed to a systematic up-bending of the comparatively thin cantilever (Figure B.10(a)). This up-bending can be avoided by a different design with a thicker cantilever, which was key to achieve the highly reproducible cantilever height shown in Figure 5.5. Besides the main resonance dips of the cavity formed by the Au mirrors, we find smaller dips from reflections at the dielectric photoresist-air interface at the bottom side of the cantilever. These reflections may be avoided by tilting the dielectric-air interface. The calculated optical Q-factor of 1600 is in good agreement with the estimated optical Q-factor of

$$Q = 4\pi L/\lambda(1 - R_{\mathrm{Au}}R_{20\mathrm{nm\,Au}}) \approx 1800,$$

where $L = 41\,\mu\mathrm{m}$ is the cavity length, $\lambda = 1550\,\mathrm{nm}$ the wavelength and $R_{\mathrm{Au}} = 0.98$ and $R_{20\mathrm{nm\,Au}} = 0.81$ are the calculated power reflection factors of the 70 nm-thick and the 20 nm-thick Au-layer.

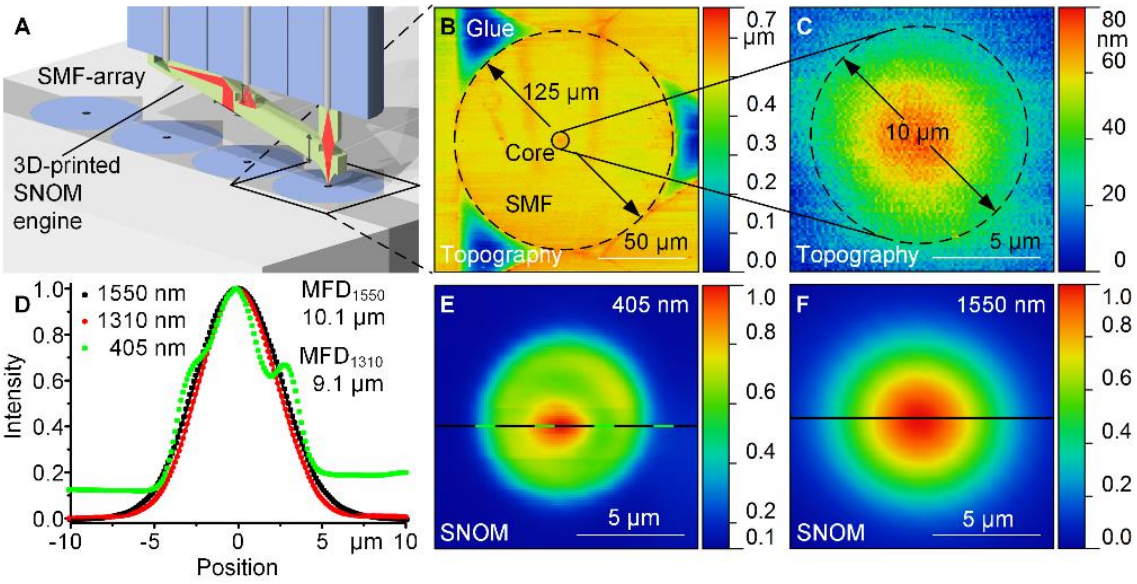

Figure B.7: Measurements of the topography and the optical near-field of a single-mode fiber (SMF). **A,** Illustration of the experimental setup. **B,** Topography of an SMF in a V-groove array. The fiber facet is indicated by a circle of 125 µm diameter. **C,** Magnification of **b**. A topographic artifact due to heating of the cantilever tip by light coupled out of the SMF is visible in the center of the fiber core [171]. **D,** Intensity profiles taken along the dashed lines in (F) (black, 1550 nm), I (green 405 nm) and a corresponding scan of taken at a wavelength of 1310 nm (red). For 1310 nm and 1550 nm, a Gaussian fit was applied. The associated $1/e^2$-widths of the intensity distributions match well to the specifications of the SMF. **E,** Optical field measured at the facet of a coiled near-infrared SMF operated at a wavelength of 405 nm. The image indicates multimode operation of the fiber. **F,** Optical field of the SMF when operated at 1550 nm, showing single-mode behavior.

B.6 Scanning Near-Field Optical Microscope (SNOM) Measurements

The SNOM engine to characterize the SMF and laser mode field corresponds to the one depicted in Figure 6.1(a) without the illumination of the SNOM tip, which is not needed for the characterization of active components. In a first experiment, we validate the functionality and the precision of our SNOM engine by sampling the optical field of a standard SMF facet at several different wavelengths, see Figure B.7(a) for the associated setup. The topography of the overall fiber facet is shown in Figure B.7(b), and Figure B.7(c) displays a

magnification of the fiber-core region while illuminating the fiber from the other end with an optical power of approximately 3 mW at a wavelength of 1550 nm. The mound in the middle of the fiber core is a measurement artifact that originates from the heat of the tip by the light emitted from the fiber facet and thereby expands the tip while scanning across that region [171]. This expansion effect vanishes completely when the fiber is not illuminated. This effect is also be observed in conventional SNOM [171]. The results of the corresponding SNOM measurements, which have been taken simultaneously with the AFM scans, are shown in Figure B.7(e) and Figure B.7(f). Figure B.7I shows a SNOM image of the facet of a coiled-up fiber (AllWave® FLEX, OFS, USA) that is designed for single-mode operation in the near-infrared but operated with a 405 nm laser. As expected, multimode behavior is clearly visible. Figure B.7(f) shows a SNOM image of the same SMF illuminated at 1550 nm. Figure B.7(d) shows the intensity distribution along selected cross-sections of both SNOM images, indicated by dashed lines in Figure B.7(e) and Figure B.7(f), along with an equivalent measurement taken at a wavelength of 1310 nm. Gaussian fits of measurements at 1310 nm and 1550 nm show $1/e^2$-MFD of 9.1 µm and 10.1 µm that closely match the specifications of the SMF [172].

We then perform a second experiment in which we measure the mode field at the facet of a horizontal-cavity surface-emitting laser (HCSEL), *i.e.*, of a distributed-feedback laser (DFB) that is equipped with an etched 45°-mirror to redirect the emitted light towards the surface-normal of the chip (Figure B.8(a)). Figure B.8(b) shows the topography of the emission window obtained by using the AFM functionality of our SPM engine. The AFM measurement contains features such as bulges along the edge of the emission facet. For SNOM measurements, Figure B.8(c), the HCSEL is operated at a wavelength around 1550 nm and a power of 1.5 mW, measured in the far-field of the device by using an integrating sphere. From the SNOM data, we extract mode field diameters (MFD) of 3.5 µm and 3.2 µm along the slow and the fast axis of the beam, respectively, both calculated by the second order-momentum method. These values are in good agreement with far-field measurements of similar HCSEL, which result in an MFD [173] of approximately 3 µm. Note that the AFM image, Figure B.8(b), and the SNOM image, Figure B.8(c), were simultaneously acquired while operating the laser. This feature allows correlating the position

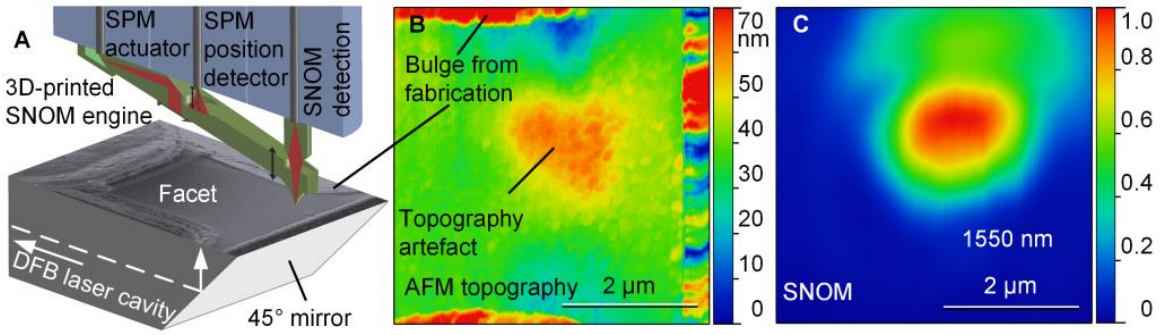

Figure B.8 AFM and SNOM imaging of a horizontal cavity surface-emitting laser (HCSEL) facet. **A,** Schematic of the measurement (not to scale): The HCSEL combines a distributed-feedback laser cavity with an etched 45°-mirror to redirect the emitted light towards a surface-normal direction. The facet is investigated during the operation of the laser using a 3D-printed SNOM engine. The rendering of HCSEL comprises an SEM image that is projected onto the top facet of the device. **B,** AFM topography of the laser facet, revealing the 3D topography of the bulges that are visible in the projected SEM image. When moved over the emission spot of the laser, the tip heats up, leading to a mound-like topographic artifact [171], which disappears once the laser is turned off. **C,** SNOM-image of the laser facet, acquired simultaneously to **b**. The laser emission spot is clearly visible, and the size of the mode field is in good agreement with far-field measurements of the laser.

of laser emission with respect to mechanical features of the facet. For the AFM image, acquisition within the strong optical field of the laser emission leads to a topography artifact, *i.e.*, a shallow mound on top of the flat device facet (Figure B.8(b)), similarly to the one observed for scanning of the fiber surface (Figure B.7(c)). This mound is caused by heating the tip when exposed to the light beam of the laser, and it disappears once the laser is turned off. This effect is also be observed in conventional SNOM [171].

We also realize SNOM engines that allow for illumination of the tip, see Figure 5.4. As a sample, we used optical nanoantenna structures on a Si surface. Due to appreciable background reflection caused by the high index contrast at the silicon-air interface, the signal never approaches zero, also in the absence of nano-antennae. To demonstrate that this contrast is not limited by the SNOM engine itself, we perform a second measurement, using s silicon photonics (SiP) grating coupler as a sample (Figure B.9). SiP grating couplers consist of regularly spaced grooves etched into the top surface of a SiP waveguide (Figure B.9(a)) and are used for coupling of free-space beams into a guided mode of a

silicon photonic waveguide [174], [175]. In our experiments, we illuminate the SNOM tip using a laser emitting at a wavelength of 960 nm. We optimize the polarization to achieve maximal contrast when scanning across the grating strips. The detected SNOM intensity values have been normalized to the maximum value. For the grating coupler, we find a dynamic range of 11 dB of the SNOM signal. This indicates that the SNOM signal is highly dependent on the local light field in the vicinity of the tip and is not dominated by any intrinsic offset. Note that the SNOM signal seems to be highest within the etched grooves of the grating, which can be inferred by comparing the topography signal and the SNOM signals in Figure B.9(b) and (c). We attribute this observation to the excitation of resonant modes with a strong field concentration in the grating grooves.

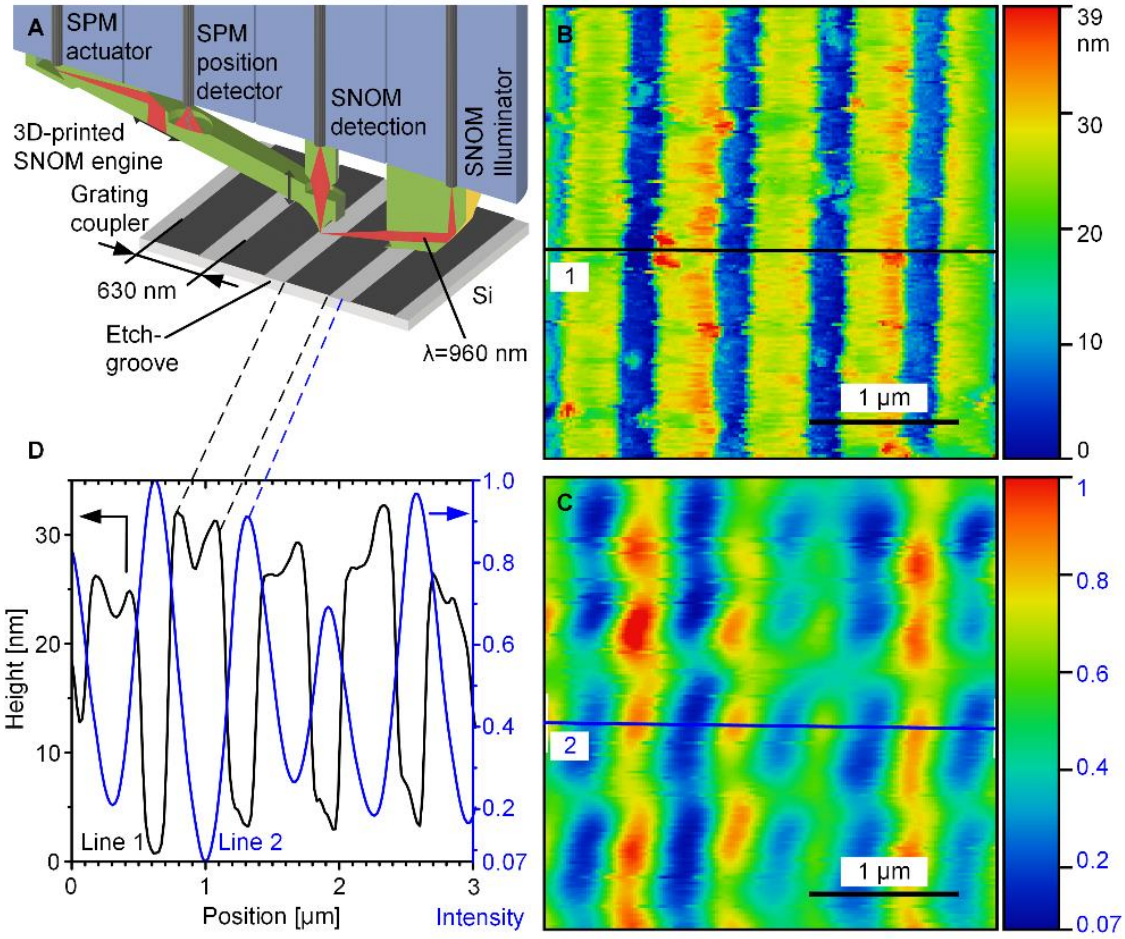

Figure B.9 Measurements of the topography and the optical near-field of a silicon grating coupler [175]. A, Measurement setup. The grating coupler consists of Si-strips etched into Si with a period of 630 nm and a depth of 150 nm. The SNOM tip is illuminated with a laser emitting a wavelength of 960 nm. B, Topography of the grating coupler. C, Optical near-field image of the grating coupler. The dynamic range of the measurement corresponds to 11 dB. The values have been normalized to the maximum value. The polarization of the SNOM illuminator has been optimized prior to measurement to achieve maximal contrast. D, Cross-section through b, black and c, blue. The highest intensity of the SNOM signal is measured at the gaps of the grating coupler.

B.7 Wafer-Level Fabrication and Reproducibility of SPM Engines

To demonstrate the reproducibility of printed SPM engines, we analysed arrays of 66 SNOM structures and 70 AFM structures on a quartz substrate with respect to their height and resonance frequency. We replaced the tip with a flat for accurate optical height measurements. The main difference between the two cantilever types was hence the thickness, which amounts to 10 µm for the AFM and to 20 µm for the AFM structure, see Figure 5.2 and Figure 5.4, respectively. To quantify the geometrical reproducibility of the structures, we measured the heights of the cantilevers above the substrate using a vertical scanning white-light interferometer (ContourGT-K, Bruker, USA). The results are indicated in Figure 6.5(c) for the SNOM cantilevers and in Figure B.10(a) for the AFM cantilevers. For the AFM (SNOM) cantilever, we measure an average height of 41.3 µm (69.0 µm) with a standard deviation of σ_h = 2.68 µm (σ_h = 0.69 µm). Note that the variation of the AFM cantilevers is considerably higher than that of the SNOM structures, which we attribute to the fact that the AFM-engine cantilever is thinner than the SNOM-engine cantilever and hence more vulnerable to internal tension that occurs during fabrication. As for the SNOM cantilevers in Figure 5.5(d), the variance of the resonance frequency of the AFM engines is measured by mechanically exciting the AFM engines using a piezo actuator below the substrate and by measuring the individual oscillation amplitudes using a deflection laser. The histogram of the measured resonance frequency is depicted in Figure B.10(b), indicating a standard deviation of σ_f = 3.91 kHz at an average resonance frequency of 183.1 kHz. This corresponds to a relative one-sigma uncertainty of 2.1 %. The resonance frequency could also be reproduced by a high-speed scanning vibrometer (Appendix B.2) with 191 kHz measured at a single cantilever.

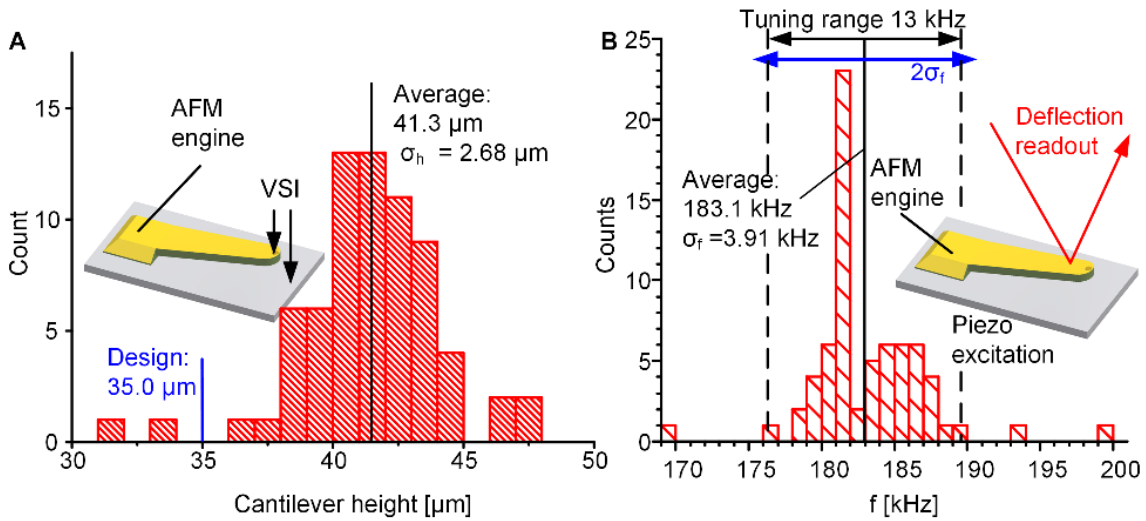

Figure B.10: Height and resonance-frequency statistics of 70 AFM-engines similar to the one used in Figure 5.2. **a**, Height statistics of cantilevers fabricated on a quartz substrate. To save writing time and to provide a sufficiently large measurement spot for the vertical scanning white-light interferometer (VSI), the tip was omitted. The height variation is considerably higher than for the SNOM-engine (Figure 6.5(c)), as the AFM-engine cantilever is thinner than the SNOM-engine cantilever, making it more vulnerable to internal tension that occurs during fabrication. **B,** Histogram displaying the resonance frequencies of 70 AFM engines fabricated on one substrate. A piezo actuator was used to mechanically excite the cantilevers with a frequency sweep, and the readout was performed individually for each cantilever using optical deflection. The $2\sigma_f$-variation is indicated by a blue arrow in comparison to the maximum tuning range accessible by heating the cantilever via the AFM engine actuator (Figure B.11).

B.8 Controlling and Fine-Tuning of Individual SPM Cantilevers

To allow for massively parallel SPM measurements with arrays of SPM (Figure 6.5), height and frequency control over individual cantilevers is essential. This can be accomplished by using an optical excitation signal that consists of a periodic power modulation for exciting the cantilever oscillation and a constant power background, which allows adjusting the profile stiffness of the cantilever.

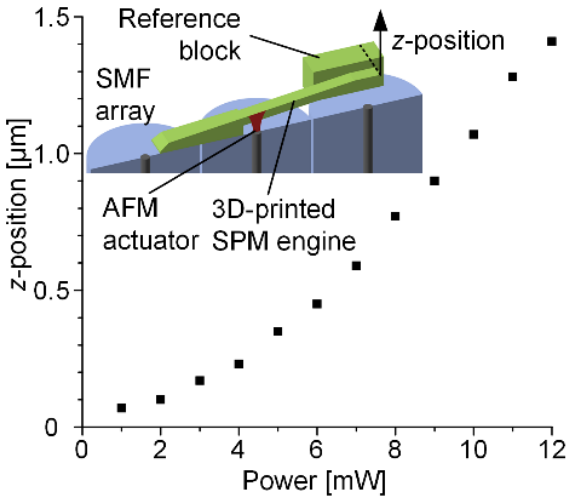

Figure B.11: Height difference of the cantilever with respect to a reference block is measured for different powers of the optical actuation signal. We find that the cantilever moves away from the fiber array. **Inset:** Cross-section through a fiber array and cantilever indicating the measurement position of the white-light vertical scanning interferometer.

To demonstrate this concept for the height adjustment, we fabricate a single tip-less cantilever on a fiber array (Figure B.11) alongside with two reference blocks. We then measure the height profile of both the cantilevers and the reference blocks with the AFM actuator switched off. Thereafter we repeat the measurement for constant powers of the AFM actuator between 1 mW and 12 mW and subtract the reference measurement. To quantify the movement of the cantilever, we evaluate the height difference from the reference block to the cantilever. We find that for increasing heating power, the cantilever moves up to 1.4 µm in positive z-direction, *i.e.*, away from the fiber array. Note that this behavior is qualitatively different from the effect discussed in Appendix B.4, where heating of the cantilever leads to a movement towards the fiber array. We attribute this to the fact that the cantilever used in Figure B11 was much thinner (width 30 µm, thickness 10 µm) than the one discussed in Appendix B.4 (width 30 … 50 µm, thickness 20 µm) and that hence the heat gradient across the cantilever cross-section has much less influence. We checked this assumption by thicker cantilever repeating the experiment with (width 50 µm, thickness 20 µm) comparable to the one used in Appendix B.4.

Here we could again observe a bending in negative z-direction, *i.e.*, towards the fiber array, for higher powers, which amounts to approximately 300 nm at 12 mW. We hence conclude that exposing printed cantilevers to a constant heating power at a selected position allows for fine-tuning the vertical position and hence to compensate fabrication tolerances.

Additionally, we show the possibility of thermal tuning to adjust the resonance frequency of a cantilever to the desired value (Figure B.11). To this end, we exploit the fact that the variation of the average power of the optical excitation allows heating the cantilever and thus adjusting its stiffness. This leads to a decrease of the resonance frequency by 2.13 kHz per milliwatt of average optical excitation power for the SNOM engine and 1.63 kHz/mW for the AFM engine. The tuning range is limited by the maximal power of the laser of approximately 12 mW and amounts to 15 kHz and 17 kHz for the AFM and SNOM engine, respectively (Figure B.10(b) and Figure 5.5(d)). Note that in both cases, the maximum frequency tuning allows to cover almost 2σf of the measured resonance frequency distribution, hence offering an effective means of compensating fabrication-related variations. We expect that systematic process optimizations might allow to further improve the reproducibility of the structure. When heating the structure, the mechanical Q-factor also changes (Figure B.12), indicating that there is additional mechanical damping at higher laser powers. This is plausible since heating of the polymer structure should lead to a softening of the material and hence damp mechanical oscillations.

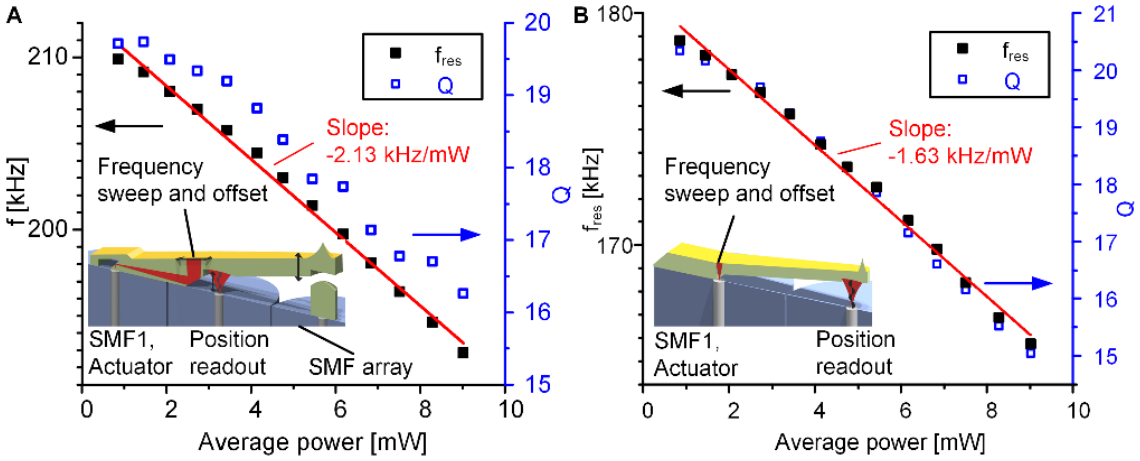

Figure B12: Tuning of mechanical resonance frequency for a, scanning near-field optical microscope (SNOM) engine and b, atomic force microscope (AFM) engine. Both structures are fabricated on single-mode fiber (SMF) arrays. Opto-thermal heating through SMF1 is used to excite the cantilevers with sinusoidal power modulation of variable frequency. Position-readout is accomplished by measuring the time-dependent reflectivity of the interferometric position sensor through SMF2. The average power of the opto-thermal excitation is adjusted by adding a constant offset to the modulation signal, varying the average temperature of the cantilever and hence its stiffness. To a first-order approximation, a linear dependence of the resonance frequency and the mechanical Q-factor on the average heating power is observable.

[end of Methods and Supplementary Information of publication [J2]*]*

C. Bibliography

[1] F. Kish *et al.*, “From Visible Light-Emitting Diodes to Large-Scale III-V Photonic Integrated Circuits,” in *Proceedings of the IEEE*, 2013, vol. 101, no. 10, pp. 2255–2270.

[2] R. Jones *et al.*, “Heterogeneously Integrated InP/Silicon Photonics: Fabricating Fully Functional Transceivers,” *IEEE Nanotechnol. Mag.*, vol. 13, no. 2, pp. 17–26, 2019.

[3] M. Hochberg and T. Baehr-Jones, “Towards Fabless Silicon Photonics,” *Nat. Photonics*, vol. 4, no. 8, pp. 492–494, 2010.

[4] E. R. H. Fuchs, R. E. Kirchain, and S. Liu, “The Future of Silicon Photonics: Not So Fast? Insights From 100G Ethernet LAN Transceivers,” *J. Light. Technol.*, vol. 29, no. 15, pp. 2319–2326, 2011.

[5] B. Snyder, B. Corbett, P. Obrien, and P. O’Brien, “Hybrid Integration of the Wavelength-Tunable Laser with a Silicon Photonic Integrated Circuit,” *J. Light. Technol.*, vol. 31, no. 24, pp. 3934–3942, 2013.

[6] T. Lamprecht *et al.*, “Passive Alignment of Optical Elements in a Printed Circuit Board,” in *Proceedings - Electronic Components and Technology Conference*, 2006, pp. 761–767.

[7] I. L. Bundalo *et al.*, “PIXAPP Photonics Packaging Pilot Line Development of a Silicon Photonic Optical Transceiver with Pluggable Fiber Connectivity,” *IEEE J. Sel. Top. Quantum Electron.*, 2022.

[8] P. Maier *et al.*, “3D-Printed Optical Elements for Coupling of VCSEL and Photodiode Arrays to Multi-Core Fibers in an SFP Transceiver Assembly,” *Opt. Fiber Commun. Conf.*, paper W2A.1, 2022.

[9] Y. Xu *et al.*, “Superconducting Nanowire Single-Photon Detector (SNSPD) with 3D-Printed Free-Form Microlenses,” *Opt. Express*, 2021.

[10] S. Singer *et al.*, “3D-Printed Facet-Attached Optical Elements for Beam Shaping in Optical Phased Arrays,” *arXiv:2203.12989*, 2022.

[11] M. Trappen *et al.*, “AFM Engine with Optical Actuation and Readout Printed on the Facet of a Multi-Core Fiber,” in *Conference on Lasers and Electro-Optics*, 2020, p. SM2N.7.

[12] M. Trappen *et al.*, “3D-Printed Optical Probes for Wafer-Level Testing of

Photonic Integrated Circuits," *Opt. Express*, vol. 28, no. 25, p. 37996, 2020.

[13] P. Hottinger *et al.*, "On-Sky Results for the Integrated Microlens Ring Tip-Tilt Sensor," *JOSA B*, vol. 38, no. 9, pp. 2517–2527, 2021.

[14] T. Anagnos *et al.*, "3D-M3: High-Spatial-Resolution Spectroscopy with Extreme AO and 3D-Printed Micro-Lenslets," *Appl. Opt.*, vol. 60, no. 19, pp. 108–121, 2021.

[15] J. Fischer, J. B. Mueller, J. Kaschke, T. J. A. Wolf, A.-N. Unterreiner, and M. Wegener, "Three-Dimensional Multi-Photon Direct Laser Writing with Variable Repetition Rate," *Opt. Express*, vol. 21, no. 22, p. 26244, 2013.

[16] J. Fischer, J. B. Mueller, A. S. Quick, J. Kaschke, C. Barner-Kowollik, and M. Wegener, "Exploring the Mechanisms in STED-Enhanced Direct Laser Writing," *Adv. Opt. Mater.*, vol. 3, no. 2, pp. 221–232, 2015.

[17] Menlo Systems GmbH, "Femtosecond Fiber Lasers." [Online]. Available: https://www.menlosystems.com/products/femtosecond-lasers-and-amplifiers/. [Accessed: 16-Jan-2020].

[18] Toptica Photonics, "Picosecond / Femtosecond Fiber Lasers." [Online]. Available: https://www.toptica.com/products/psfs-fiber-lasers/. [Accessed: 16-Jan-2020].

[19] M. Malinauskas, P. Danilevičius, and S. Juodkazis, "Three-Dimensional Micro-/Nano-Structuring via Direct Write Polymerization with Picosecond Laser Pulses," *Opt. Express*, vol. 19, no. 6, p. 5602, 2011.

[20] A. Trautmann, "Zwei-Photonen-Polymerisation als Methode zur Herstellung Medizintechnischer Funktionselemente," (doctoral thesis), https://tuprints.ulb.tu-darmstadt.de/8363/, 2019.

[21] Gooch & Housego, "Acousto-Optic Modulators (AOM)." [Online]. Available: https://gandh.com/product-categories/acousto-optic-modulators/. [Accessed: 16-Jan-2020].

[22] K. Y. Lee *et al.*, "Micromachining Applications of a High Resolution Ultrathick Photoresist," *J. Vac. Sci. Technol. B Microelectron. Nanom. Struct.*, vol. 13, no. 6, pp. 3012–3016, 1995.

[23] K. J. Schafer, J. M. Hales, M. Balu, K. D. Belfield, E. W. Van Stryland, and D. J. Hagan, "Two-Photon Absorption Cross-Sections of Common Photoinitiators," *J. Photochem. Photobiol. A Chem.*, vol. 162, no. 2–3, pp.

497–502, 2004.

[24] T. Zandrini *et al.*, “Effect of the Resin Viscosity on the Writing Properties of Two-Photon Polymerization,” *Opt. Mater. Express*, vol. 9, no. 6, p. 2601, 2019.

[25] A. Ovsianikov *et al.*, “Ultra-Low Shrinkage Hybrid Photosensitive Material for Two-Photon Polymerization Microfabrication,” *ACS Nano*, vol. 2, no. 11, pp. 2257–2262, 2008.

[26] J. Fischer, “Three-Dimensional Optical Lithography beyond the Diffraction Limit,” (doctoral thesis), Karlsruher Instituts für Technologie (KIT), DOI: 10.5445/IR/1000028704, 2012.

[27] K. Cicha *et al.*, “Evaluation of 3D Structures Fabricated with Two-Photon-Photopolymerization by Using FTIR Spectroscopy,” *J. Appl. Phys.*, vol. 110, no. 6, p. 064911, 2011.

[28] L. Zheng *et al.*, “Nanofabrication of High-Resolution Periodic Structures with a Gap Size Below 100 nm by Two-Photon Polymerization,” *Nanoscale Res. Lett.*, vol. 14, 2019.

[29] C. Arnoux *et al.*, “Understanding and Overcoming Proximity Effects in Multi-Spot Two-Photon Direct Laser Writing,” *Addit. Manuf.*, vol. 49, no. 102491, 2021.

[30] P. Kiefer *et al.*, “Sensitive Photoresists for Rapid Multiphoton 3D Laser Micro- and Nanoprinting,” *Adv. Opt. Mater.*, vol. 8, no. 19, p. 2000895, 2020.

[31] M. Thiel, J. Fischer, G. Von Freymann, and M. Wegener, “Direct Laser Writing of Three-Dimensional Submicron Structures Using a Continuous-Wave Laser at 532 nm,” *Appl. Phys. Lett.*, vol. 97, no. 22, 2010.

[32] P. Mueller, M. Thiel, and M. Wegener, “3D Direct Laser Writing Using a 405 nm Diode Laser,” *Opt. Lett.*, vol. 39, no. 24, p. 6847, 2014.

[33] J. B. Müller, “Exploring the Mechanisms of Three-Dimensional Direct Laser Writing by Multi-Photon Polymerization,” 2015.

[34] J. Fischer and M. Wegener, “Three-Dimensional Direct Laser Writing Inspired by Stimulated-Emission-Depletion Microscopy,” *Opt. Mater. Express*, vol. 1, no. 4, p. 614, 2011.

[35] B. Harke *et al.*, “Polymerization Inhibition by Triplet State Absorption for Nanoscale Lithography,” *Adv. Mater.*, vol. 25, no. 6, pp. 904–909, 2013.

[36] P. Prabhakaran, Y. Son, C.-W. Ha, J.-J. Park, S. Jeon, and K.-S. Lee,

"Optical Materials Forming Tightly Polymerized Voxels during Laser Direct Writing," *Adv. Eng. Mater.*, vol. 20, no. 10, p. 1800320, 2018.

[37] I. Sakellari *et al.*, "Diffusion-Assisted High-Resolution Direct Femtosecond Laser Writing," *ACS Nano*, vol. 6, no. 3, pp. 2302–2311, 2012.

[38] W. E. Lu, X. Z. Dong, W. Q. Chen, Z. S. Zhao, and X. M. Duan, "Novel Photoinitiator with a Radical Quenching Moiety for Confining Radical Diffusion in Two-Photon Induced Photopolymerization," *J. Mater. Chem.*, vol. 21, no. 15, pp. 5650–5659, 2011.

[39] A. Ovsianikov, X. Shizhou, M. Farsari, M. Vamvakaki, C. Fotakis, and B. N. Chichkov, "Shrinkage of Microstructures Produced by Two-Photon Polymerization of Zr-Based Hybrid Photosensitive Materials," *Opt. Express*, vol. 17, no. 4, p. 2143, 2009.

[40] G. Göring *et al.*, "Tailored Probes for Atomic Force Microscopy Fabricated by Two-Photon Polymerization," *Appl. Phys. Lett.*, vol. 109, no. 6, p. 063101, 2016.

[41] A. Zakhurdaeva, P.-I. Dietrich, H. Hölscher, C. Koos, J. Korvink, and S. Sharma, "Custom-Designed Glassy Carbon Tips for Atomic Force Microscopy," *Micromachines*, vol. 8, no. 9, p. 285, 2017.

[42] G. T. Reed, G. Mashanovich, F. Y. Gardes, and D. J. Thomson, "Silicon Optical Modulators," *Nat. Photonics*, vol. 4, no. 8, pp. 518–526, 2010.

[43] C. R. Doerr, "Silicon Photonic Integration in Telecommunications," *Front. Phys.*, vol. 3, p. 37, 2015.

[44] T. Baehr-Jones, T. Pinguet, P. Lo Guo-Qiang, S. Danziger, D. Prather, and M. Hochberg, "Myths and Rumours of Silicon Photonics," *Nat. Photonics*, vol. 6, no. 4, pp. 206–208, 2012.

[45] EUROPRACTICE, "Si-Photonics ISiPP50G." [Online]. Available: https://europractice-ic.com/mpw-prototyping/siphotonics/imec/. [Accessed: 16-Jan-2020].

[46] Advanced Micro Foundry (AMF), "Technology Platforms & Device Library." [Online]. Available: http://www.advmf.com/technology-platforms-library/. [Accessed: 16-Jan-2020].

[47] D. Kohler *et al.*, "Biophotonic Sensors with Integrated Si3N4-Organic Hybrid (SiNOH) Lasers for Point-of-Care Diagnostics," *Light Sci. Appl. 2021 101*, vol. 10, no. 1, pp. 1–12, 2021.

[48] C. V. Poulton *et al.*, “Large-Scale Silicon Nitride Nanophotonic Phased Arrays at Infrared and Visible Wavelengths,” *Opt. Lett.*, vol. 42, no. 1, p. 21, 2017.

[49] P. Trocha *et al.*, “Ultrafast Optical Ranging Using Microresonator Soliton Frequency Combs,” *Science*, vol. 359, no. 6378, pp. 887–891, 2018.

[50] K. Wörhoff, R. G. Heideman, A. Leinse, and M. Hoekman, “TriPleX: A Versatile Dielectric Photonic Platform,” *Adv. Opt. Technol.*, vol. 4, no. 2, pp. 189–207, 2015.

[51] C. Koos, C. G. Poulton, L. Zimmermann, L. Jacome, J. Leuthold, and W. Freude, “Ideal Bend Contour Trajectories for Single-Mode Operation of Low-Loss Overmoded Waveguides,” *IEEE Photonics Technol. Lett.*, vol. 19, no. 11, pp. 819–821, 2007.

[52] B. Corbett *et al.*, “Transfer-Printing for Heterogeneous Integration,” in *Optical Fiber Communication Conference (OFC)*, 2019, paper M2D.1.

[53] G. A. Fish and D. K. Sparacin, “Optical Transceivers Using Heterogeneous Integration on Silicon,” in *Topics in Applied Physics*, vol. 122, pp. 375–395, 2016.

[54] J. S. Lee *et al.*, “Meeting the Electrical, Optical, and Thermal Design Challenges of Photonic-Packaging,” *IEEE J. Sel. Top. Quantum Electron.*, vol. 22, no. 6, pp. 409–417, 2016.

[55] S. Hardy, “Intel Shipping Silicon Photonics Optical Transceivers | Lightwave,” 2016. [Online]. Available: https://www.lightwaveonline.com/optical-tech/transmission/article/16654194/intel-shipping-silicon-photonics-optical-transceivers. [Accessed: 16-Jan-2020].

[56] R. Marchetti, C. Lacava, L. Carroll, K. Gradkowski, and P. Minzioni, “Coupling Strategies for Silicon Photonics Integrated Chips,” *Photon. Res.*, vol. 7, no. 2, pp. 201–239, 2019.

[57] P. O’Brien, L. Carrol, C. Eason, and J. S. Lee, “Packaging of Silicon Photonic Devices,” in *Silicon Photonics III*, Springer Berlin Heidelberg, 2016, pp. 217–236.

[58] A. Mekis *et al.*, “Advanced Silicon Photonics Transceivers,” in *Topics in Applied Physics*, vol. 122, pp. 349–374, 2016.

[59] G. B. Preve, “Silicon Photonics Packaging Automation: Problems, Challenges, and Considerations,” in *Silicon Photonics III*, Springer Berlin

Heidelberg, 2016, pp. 237–259.

[60] Epoxy Technology, "EPO-TEK H20E." [Online]. Available: http://www.epotek.com/site/administrator/components/com_products/assets/files/Style_Uploads/H20E.pdf. [Accessed: 26-Mar-2020].

[61] N. Lindenmann *et al.*, "Photonic Wire Bonding: A Novel Concept for Chip-Scale Interconnects.," *Opt. Express*, vol. 20, no. 16, pp. 17667–17677, 2012.

[62] N. Lindenmann *et al.*, "Connecting Silicon Photonic Circuits to Multicore Fibers by Photonic Wire Bonding," *J. Light. Technol.*, vol. 33, no. 4, pp. 755–760, 2015.

[63] M. R. Billah *et al.*, "Hybrid Integration of Silicon Photonics Circuits and InP Lasers by Photonic Wire Bonding," *Optica*, vol. 5, no. 6, pp. 2334–2536, 2018.

[64] NASA, "Exoplanet Exploration Program," 2021. [Online]. Available: https://exoplanets.nasa.gov/.

[65] S. Halverson, A. Roy, S. Mahadevan, and C. Schwab, "'Modal-Noise' in Single-Mode Fibers: A Cautionary Note for High Precision Radial Velocity Instruments," *Astrophys. J. Lett.*, vol. 814, no. 2, p. 6, 2015.

[66] A. Bechter *et al.*, "On-Sky Single-Mode Fiber Coupling Measurements at the Large Binocular Telescope," in *SPIE Astronomical Telescopes and Instrumentation*, 2016, p. 99092.

[67] J. Bland-Hawthorn, M. Englund, and G. Edvell, "New Approach to Atmospheric OH Suppression Using an Aperiodic Fibre Bragg Grating," *Opt. Express*, vol. 12, no. 24, p. 5902, 2004.

[68] G. Binnig, H. Rohrer, C. Gerber, and E. Weibel, "Tunneling through a Controllable Vacuum Gap," *Appl. Phys. Lett.*, vol. 40, no. 2, pp. 178–180, 1982.

[69] G. Binnig, C. F. Quate, and C. Gerber, "Atomic Force Microscope," *Phys. Rev. Lett.*, vol. 56, no. 9, pp. 930–933, 1986.

[70] F. Ohnesorge and G. Binnig, "True Atomic Resolution by Atomic Force Microscopy through Repulsive and Attractive Forces," *Science*, vol. 260, no. 5113, pp. 1451–1456, 1993.

[71] I. E. Dzyaloshinskii, E. M. Lifshitz, and L. P. Pitaevskii, "General Theory of Van Der Waals' Forces," *Sov. Phys. Uspekhi*, vol. 4, no. 2, p. 153, 1961.

[72] J. E. Jones, "On the Determination of Molecular Fields.—I. From the

Variation of the Viscosity of a Gas with Temperature," *Proc. R. Soc.*, vol. 106, no. 738, pp. 441–462, 1924.

[73] E. H. Synge, "A Suggested Method for Extending Microscopic Resolution into the Ultra-Microscopic Region," *Philos. Mag. J. Sci.*, vol. 6, no. 35, pp. 356–362, 1928.

[74] D. W. Pohl, W. Denk, and M. Lanz, "Optical Stethoscopy: Image Recording with Resolution λ/20," *Appl. Phys. Lett.*, vol. 44, no. 7, pp. 651–653, 1984.

[75] U. Dürig, D. W. Pohl, and F. Rohner, "Near-Field Optical-Scanning Microscopy," *J. Appl. Phys.*, vol. 59, no. 10, pp. 3318–3327, 1986.

[76] B. Hecht, H. Bielefeldt, Y. Inouye, D. W. Pohl, and L. Novotny, "Facts and Artifacts in Near-Field Optical Microscopy," *J. Appl. Phys.*, vol. 81, no. 6, p. 2492, 1998.

[77] B. Pezeshki *et al.*, "High Performance MEMS-Based Micro-Optic Assembly for Multi-Lane Transceivers," *J. Light. Technol.*, vol. 32, no. 16, pp. 2796–2799, 2014.

[78] Z.-N. Tian *et al.*, "Beam Shaping of Edge-Emitting Diode Lasers Using a Single Double-Axial Hyperboloidal Micro-Lens," *Opt. Lett.*, vol. 38, no. 24, pp. 5414–5417, 2013.

[79] C. Scarcella *et al.*, "Pluggable Single-Mode Fiber-Array-to-PIC Coupling Using Micro-Lenses," *IEEE Photonics Technol. Lett.*, vol. 29, no. 22, pp. 1943–1946, 2017.

[80] F. E. Doany *et al.*, "Multichannel High-Bandwidth Coupling of Ultradense Silicon Photonic Waveguide Array to Standard-Pitch Fiber Array," *J. Light. Technol.*, vol. 29, no. 4, pp. 475–482, 2011.

[81] D. Taillaert *et al.*, "An Out-of-Plane Grating Coupler for Efficient Butt-Coupling between Compact Planar Waveguides and Single-Mode Fibers," *IEEE J. Quantum Electron.*, vol. 38, no. 7, pp. 949–955, 2002.

[82] D. Taillaert, H. Chong, P. I. Borel, L. H. Frandsen, R. M. De La Rue, and R. Baets, "A Compact Two-Dimensional Grating Coupler Used as a Polarization Splitter," *IEEE Photonics Technol. Lett.*, vol. 15, no. 9, pp. 1249–1251, 2003.

[83] B. Snyder, P. O'Brien, and P. O 'brien, "Packaging Process for Grating-Coupled Silicon Photonic Waveguides Using Angle-Polished Fibers," *IEEE Trans. Components, Packag. Manuf. Technol.*, vol. 3, no. 6, pp.

954–959, 2013.

[84] C. Li, K. S. Chee, J. Tao, H. Zhang, M. Yu, and G. Q. Lo, “Silicon Photonics Packaging with Lateral Fiber Coupling to Apodized Grating Coupler Embedded Circuit,” *Opt. Express*, vol. 22, no. 20, 2014.

[85] J. H. Song, H. N. J. Fernando, B. Roycroft, B. Corbett, and F. H. Peters, “Practical Design of Lensed Fibers for Semiconductor Laser Packaging Using Laser Welding Technique,” *J. Light. Technol.*, vol. 27, no. 11, pp. 1533–1539, 2009.

[86] C. Kopp *et al.*, “Silicon Photonic Circuits: On-CMOS Integration, Fiber Optical Coupling, and Packaging,” *IEEE J. Sel. Top. Quantum Electron.*, vol. 17, no. 3, pp. 498–509, 2011.

[87] C. A. Edwards, H. M. Presby, and C. Dragone, “Ideal Microlenses for Laser to Fiber Coupling,” *J. Light. Technol.*, vol. 11, no. 2, pp. 252–257, 1993.

[88] S. M. Yeh, S. Y. Huang, and W. H. Cheng, “A New Scheme of Conical-Wedge-Shaped Fiber Endface for Coupling between High-Power Laser Diodes and Single-Mode Fibers,” *J. Light. Technol.*, vol. 23, no. 4, pp. 1781–1786, 2005.

[89] M. He, X.-C. Yuan, N. Ngo, J. Bu, and S. Tao, “Low-Cost and Efficient Coupling Technique Using Reflowed Sol-Gel Microlens,” *Opt. Express*, vol. 11, no. 14, pp. 1621–1627, 2003.

[90] N. Pavarelli *et al.*, “Optical and Electronic Packaging Processes for Silicon Photonic Systems,” *J. Light. Technol. Vol. 33, Issue 5, pp. 991-997*, vol. 33, no. 5, pp. 991–997, 2015.

[91] J. J. Fijol *et al.*, “Fabrication of Silicon-on-Insulator Adiabatic Tapers for Low-Loss Optical Interconnection of Photonic Devices,” in *Photonics Packaging and Integration III*, 2003, pp. 157–170.

[92] R. A. Modavis and T. W. Webb, “Anamorphic Microlens for Laser Diode to Single-Mode Fiber Coupling,” *IEEE Photonics Technol. Lett.*, vol. 7, no. 7, pp. 798–800, 1995.

[93] R. Dangel *et al.*, “Polymer Waveguides for Electro-Optical Integration in Data Centers and High-Performance Computers,” *Opt. Express*, vol. 23, no. 4, pp. 4736–4750, 2015.

[94] S. Kawata, H.-B. Sun, T. Tanaka, and K. Takada, “Finer Features for Functional Microdevices,” *Nature*, vol. 412, no. 6848, pp. 697–698, 2001.

[95] S. Maruo, O. Nakamura, and S. Kawata, “Three-Dimensional Microfabrication with Two-Photon-Absorbed Photopolymerization,” *Opt. Lett.*, vol. 22, no. 2, pp. 132–134, 1997.

[96] M. Deubel, G. von Freymann, M. Wegener, S. Pereira, K. Busch, and C. M. Soukoulis, “Direct Laser Writing of Three-Dimensional Photonic-Crystal Templates for Telecommunications,” *Nat. Mater.*, vol. 3, no. 7, pp. 444–447, 2004.

[97] M. Malinauskas *et al.*, “Femtosecond Laser Polymerization of Hybrid/Integrated Micro-Optical Elements and Their Characterization,” *J. Opt.*, vol. 12, no. 12, p. 124010, 2010.

[98] G. Cojoc *et al.*, “Optical Micro-Structures Fabricated on Top of Optical Fibers by Means of Two-Photon Photopolymerization,” *Microelectron. Eng.*, vol. 87, no. 5–8, pp. 876–879, 2010.

[99] T. Gissibl, S. Thiele, A. Herkommer, H. Giessen, and M. C. J. Large, “Sub-Micrometre Accurate Free-Form Optics by Three-Dimensional Printing on Single-Mode Fibres,” *Nat. Commun.*, vol. 7, pp. 11763–11772, 2016.

[100] T. Gissibl, S. Thiele, A. Herkommer, and H. Giessen, “Two-Photon Direct Laser Writing of Ultracompact Multi-Lens Objectives,” *Nat. Photonics*, vol. 10, no. 8, pp. 554–560, 2016.

[101] S. Thiele, T. Gissibl, H. Giessen, and A. M. Herkommer, “Ultra-Compact on-Chip LED Collimation Optics by 3D Femtosecond Direct Laser Writing,” *Opt. Lett.*, vol. 41, no. 13, pp. 3029–3032, 2016.

[102] Y. Fu, N. K. A. Bryan, and O. N. Shing, “Integrated Micro-Cylindrical Lens with Laser Diode for Single-Mode Fiber Coupling,” *IEEE Photonics Technol. Lett.*, vol. 12, no. 9, pp. 1213–1215, 2000.

[103] M. Moehrle *et al.*, “Ultra-Low Threshold 1490 nm Surface-Emitting BH-DFB Laser Diode with Integrated Monitor Photodiode,” in *2010 22nd International Conference on Indium Phosphide and Related Materials (IPRM)*, pp. 1–4, 2010.

[104] T. Suzuki *et al.*, “Cost-Effective Optical Sub-Assembly Using Lens-Integrated Surface-Emitting Laser,” *J. Light. Technol.*, vol. 34, no. 2, pp. 358–364, 2016.

[105] M.-C. Amann and W. Hofmann, “InP-Based Long-Wavelength VCSELs and VCSEL Arrays,” *IEEE J. Sel. Top. Quantum Electron.*, vol. 15, no. 3, pp. 861–868, 2009.

[106] M. Mack, M. Peterson, S. Gloeckner, A. Narasimha, R. Koumans, and P. De Dobbelaere, “Method and System for a Light Source Assembly Supporting Direct Coupling to an Integrated Circuit,” US20100006784 A1, 2008.

[107] M. Kowalczyk, J. Haberko, and P. Wasylczyk, “Microstructured Gradient-Index Antireflective Coating Fabricated on a Fiber Tip with Direct Laser Writing.,” *Opt. Express*, vol. 22, no. 10, pp. 12545–50, 2014.

[108] J. Bland-Hawthorn *et al.*, “PIMMS: Photonic Integrated Multimode Microspectrograph,” in *Proceedings of SPIE - The International Society for Optical Engineering*, p. 77350, 2010.

[109] I. Spaleniak, N. Jovanovic, S. Gross, M. J. Ireland, J. S. Lawrence, and M. J. Withford, “Integrated Photonic Building Blocks for Next-Generation Astronomical Instrumentation II: The Multimode to Single Mode Transition,” *Opt. Express*, vol. 21, no. 22, p. 27197, 2013.

[110] S. Shaklan and F. Roddier, “Coupling Starlight into Single-Mode Fiber Optics,” *Appl. Opt.*, vol. 27, no. 11, p. 2334, 1988.

[111] S. Esposito *et al.*, “Large Binocular Telescope Adaptive Optics System: New Achievements and Perspectives in Adaptive Optics,” in *Astronomical Adaptive Optics Systems and Applications IV*, 2011, p. 814902.

[112] N. Jovanovic, C. Schwab, N. Cvetojevic, O. Guyon, and F. Martinache, “Enhancing Stellar Spectroscopy with Extreme Adaptive Optics and Photonics,” *Publ. Astron. Soc. Pac.*, vol. 128, 2016.

[113] M. Glück, J.-U. Pott, and O. Sawodny, “Investigations of an Accelerometer-Based Disturbance Feedforward Control for Vibration Suppression in Adaptive Optics of Large Telescopes,” *Publ. Astron. Soc. Pacific*, vol. 129, no. 976, p. 065001, 2017.

[114] P. R. Gillingham, S. Miziarski, and U. Klauser, “Mechanical Features of the OzPoz Fiber Positioner for the VLT,” in *Optical and IR Telescope Instrumentation and Detectors*, p. 914, 2000.

[115] J. J. Bryant, J. W. O’Byrne, J. Bland-Hawthorn, and S. G. Leon-Saval, “Characterization of Hexabundles: Initial Results,” in *Monthly Notices of the Royal Astronomical Society*, vol. 415, no. 3, pp. 2173–2181, 2011.

[116] Zemax LCC, “OpticStudio.” [Online]. Available: http://www.zemax.com/os/opticstudio. [Accessed: 27-Jan-2017].

[117] Fibercore, “Product - Multicore Fiber.” [Online]. Available: http://fibercore.com/product/multicore-fiber. [Accessed: 20-Apr-2017].

[118] Nanoscribe GmbH. [Online]. Available: http://www.nanoscribe.de/en/products/. [Accessed: 27-Jan-2017].

[119] R. J. Harris *et al.*, “Photonic Spatial Reformatting of Stellar Light for Diffraction-Limited Spectroscopy,” in *Monthly Notices of the Royal Astronomical Society*, vol. 450, no. 1, pp. 428–434, 2015.

[120] S. Kirkpatrick, C. D. Gelatt, and M. P. Vecchi, “Optimization by Simulated Annealing,” *Science*, vol. 220, no. 4598, pp. 671–680, 1983.

[121] G. Binnig, C. F. Quate, and C. Gerber, “Atomic Force Microscope,” *Phys. Rev. Lett.*, vol. 56, no. 9, pp. 930–933, 1986.

[122] F. J. Giessibl, “Atomic Resolution of the Silicon (111)-(7x7) Surface by Atomic Force Microscopy.,” *Science*, vol. 267, no. 5194, pp. 68–71, 1995.

[123] S. M. Y. Sugawara, M. Ohta, H. Ueyama, “Defect Motion on an InP(110) Surface Observed with Noncontact Atomic Force Microscopy,” *Science*, vol. 270, no. 5242, pp. 1646–1648, 1995.

[124] D. Pires *et al.*, “Nanoscale Three-Dimensional Patterning of Molecular Resists by Scanning Probes.,” *Science*, vol. 328, no. 5979, pp. 732–5, 2010.

[125] P. Vettiger *et al.*, “The ‘Millipede’ - Nanotechnology Entering Data Storage,” *IEEE Trans. Nanotechnol.*, vol. 1, no. 1, pp. 39–55, 2002.

[126] E. Eleftheriou *et al.*, “Millipede - a MEMS-Based Scanning-Probe Data-Storage System,” *IEEE Trans. Magn.*, vol. 39, no. 2, pp. 938–945, 2003.

[127] Y. Sakiyama, A. Mazur, L. E. Kapinos, and R. Y. H. Lim, “Spatiotemporal Dynamics of the Nuclear Pore Complex Transport Barrier Resolved by High-Speed Atomic Force Microscopy,” *Nat. Nanotechnol.*, vol. 11, no. 8, pp. 719–723, 2016.

[128] A. P. Nievergelt, N. Banterle, S. H. Andany, P. Gönczy, and G. E. Fantner, “High-Speed Photothermal off-Resonance Atomic Force Microscopy Reveals Assembly Routes of Centriolar Scaffold Protein SAS-6,” *Nat. Nanotechnol.*, vol. 13, 2018.

[129] E. A. Lopez-Guerra, H. Shen, S. Solares, and D. Shuai, “Acquisition of Time-Frequency Localized Mechanical Properties of Biofilms and Single Cells with High Spatial Resolution,” *Nanoscale*, vol. 11, no. 18, pp. 8918–8929, 2019.

[130] P. Eaton and P. West, *Atomic Force Microscopy*. Oxford University Press, 2010.

[131] H. P. Lang *et al.*, "Sequential Position Readout from Arrays of Micromechanical Cantilever Sensors," *Appl. Phys. Lett.*, vol. 72, no. 3, p. 383, 1998.

[132] W. Hu *et al.*, "Demonstration of Microcantilever Array with Simultaneous Readout Using an In-Plane Photonic Transduction Method," *Rev. Sci. Instrum.*, vol. 80, no. 8, p. 085101, 2009.

[133] E. Betzig and R. J. Chichester, "Single Molecules Observed by Near-Field Scanning Optical Microscopy," *Science*, vol. 262, no. 5138, pp. 1422–1425, 1993.

[134] R. Zhang *et al.*, "Chemical Mapping of a Single Molecule by Plasmon-Enhanced Raman Scattering," *Nature*, vol. 498, pp. 82–86, 2013.

[135] R. Hillenbrand, T. Taubner, and F. Keilmann, "Phonon-Enhanced Light–Matter Interaction at the Nanometre Scale," *Nature*, vol. 418, no. 6894, pp. 159–162, 2002.

[136] J. Chen *et al.*, "Optical Nano-Imaging of Gate-Tunable Graphene Plasmons," *Nature*, vol. 487, pp. 77–81, 2012.

[137] W. Bao *et al.*, "Mapping Local Charge Recombination Heterogeneity by Multidimensional Nanospectroscopic Imaging," *Science*, vol. 338, no. 6112, pp. 1317–1321, 2012.

[138] W. D. Herzog, M. S. Ünlü, B. B. Goldberg, G. H. Rhodes, and C. Harder, "Beam Divergence and Waist Measurements of Laser Diodes by Near-Field Scanning Optical Microscopy," *Appl. Phys. Lett.*, vol. 68, pp. 688–690, 1998.

[139] T. Michels and V. Aksyuk, "Optical Probe for Nondestructive Wafer-Scale Characterization of Photonic Elements," *IEEE Photonics Technol. Lett.*, vol. 29, no. 8, pp. 643–646, 2017.

[140] B. Hecht *et al.*, "Scanning Near-Field Optical Microscopy with Aperture Probes: Fundamentals and Applications," *J. Chem. Phys.*, vol. 112, p. 7761, 2000.

[141] N. Alsharif, A. Burkatovsky, C. Lissandrello, K. M. Jones, A. E. White, and K. A. Brown, "Design and Realization of 3D Printed AFM Probes," *Small*, vol. 14, no. 19, p. 1800162, 2018.

[142] K. Edelmann *et al.*, "Light Collection from a Low-Temperature Scanning

Tunneling Microscope Using Integrated Mirror Tips Fabricated by Direct Laser Writing," *Rev. Sci. Instrum.*, vol. 89, no. 12, p. 123107, 2018.

[143] J. D. Adams, B. W. Erickson, J. Grossenbacher, J. Brugger, A. Nievergelt, and G. E. Fantner, "Harnessing the Damping Properties of Materials for High-Speed Atomic Force Microscopy," *Nat. Nanotechnol.*, vol. 11, no. 2, pp. 147–151, 2015.

[144] P. Trucano and R. Chen, "Structure of Graphite by Neutron Diffraction," *Nature*, vol. 258, no. 5531, pp. 136–137, 1975.

[145] H. I. Rasool, P. R. Wilkinson, A. Z. Stieg, and J. K. Gimzewski, "A Low Noise All-Fiber Interferometer for High Resolution Frequency Modulated Atomic Force Microscopy Imaging in Liquids," *Rev. Sci. Instrum.*, vol. 81, no. 2, p. 023703, 2010.

[146] K. Schoenwald, Z. C. Peng, D. Noga, S. R. Qiu, and T. Sulchek, "Integration of Atomic Force Microscopy and a Microfluidic Liquid Cell for Aqueous Imaging and Force Spectroscopy," *Rev. Sci. Instrum.*, vol. 81, no. 5, p. 053704, 2010.

[147] T. E. Schäffer, J. P. Cleveland, F. Ohnesorge, D. A. Walters, and P. K. Hansma, "Studies of Vibrating Atomic Force Microscope Cantilevers in Liquid," *J. Appl. Phys.*, vol. 80, no. 7, p. 3622, 1998.

[148] D. Ebeling, H. Hölscher, H. Fuchs, B. Anczykowski, and U. D. Schwarz, "Imaging of Biomaterials in Liquids: A Comparison between Conventional and *Q* -Controlled Amplitude Modulation ('Tapping Mode') Atomic Force Microscopy," *Nanotechnology*, vol. 17, no. 7, pp. S221–S226, 2006.

[149] H. Hölscher and U. D. Schwarz, "Q-Controlled Amplitude Modulation Atomic Force Microscopy in Liquids: An Analysis," *Appl. Phys. Lett.*, vol. 89, no. 7, p. 073117, 2006.

[150] A. H. Atabaki *et al.*, "Integrating Photonics with Silicon Nanoelectronics for the next Generation of Systems on a Chip," *Nature*, vol. 556, no. 7701, pp. 349–354, 2018.

[151] J. Wang *et al.*, "Multidimensional Quantum Entanglement with Large-Scale Integrated Optics.," *Science*, vol. 360, no. 6386, pp. 285–291, 2018.

[152] F. Kish *et al.*, "System-on-Chip Photonic Integrated Circuits," *IEEE J. Sel. Top. Quantum Electron.*, vol. 24, no. 1, pp. 1–20, 2018.

[153] K. Y. Yang *et al.*, "Bridging Ultrahigh-Q Devices and Photonic Circuits,"

Nat. Photonics, vol. 12, no. 5, pp. 297–302, 2018.

[154] M. Blaicher *et al.*, "3D-Printed Ultra-Broadband Highly Efficient Out-of-Plane Coupler for Photonic Integrated Circuits," in *Conference on Lasers and Electro-Optics*, 2018, p. STh1A.1.

[155] Telcordia, [Online]. Available: https://telecom-info.telcordia.com/site-cgi/ido/docs.cgi?ID=SEARCH&DOCUMENT=GR. [Accessed: 23-Jan-2020].

[156] IXYS Corporation, "Lead Free Solder Reflow for Semiconductor Power Devices," 2006. [Online]. Available: www.ixys.com. [Accessed: 16-Jan-2020].

[157] Z. L. and J. Liu, "The Nordic Electronics Packaging Guideline," *Microelectron. Int.*, vol. 17, no. 1, 2000.

[158] F. Eltes *et al.*, "An Integrated Cryogenic Optical Modulator," *Nat. Mater.*, vol. 19, pp. 1164–1168, 2019.

[159] J. Wang, F. Sciarrino, A. Laing, and M. G. Thompson, "Integrated Photonic Quantum Technologies," *Nat. Photonics*. Nature Publishing Group, 2019.

[160] R. Logan, M. Beranek, and D. Renner, "SAE ARP6318 Aerospace Photonics Technology Readiness Advancement and Insertion via Verification and Validation of Active Photonic Device Reliability and Packaging Durability," in *IEEE Avionics and Vehicle Fiber-Optics and Photonics Conference*, pp. 49–50, 2017.

[161] ASTM, [Online]. Available: https://compass.astm.org/EDIT/html_annot.cgi?E595+15. [Accessed: 23-Jan-2020].

[162] L. J. Jiang *et al.*, "Two-Photon Polymerization: Investigation of Chemical and Mechanical Properties of Resins Using Raman Microspectroscopy," *Opt. Lett.*, vol. 39, no. 10, p. 3034, 2014.

[163] J. S. Oakdale, J. Ye, W. L. Smith, and J. Biener, "Post-Print UV Curing Method for Improving the Mechanical Properties of Prototypes Derived from Two-Photon Lithography," *Opt. Express*, vol. 24, no. 24, p. 27077, 2016.

[164] Vanguard Automation GmbH, [Online]. Available: www.vanguard-automation.com.

[165] Vanguard Photonics GmbH, "Shop - Vanguard Photonics." [Online].

Available: http://www.vanguard-photonics.com/shop/. [Accessed: 13-Dec-2017].

[166] Z. Li *et al.*, "Silyl-Based Initiators for Two-Photon Polymerization: From Facile Synthesis to Quantitative Structure–Activity Relationship Analysis," *Polym. Chem.*, vol. 8, no. 43, pp. 6644–6653, 2017.

[167] H.-J. Butt and M. Jaschke, "Calculation of Thermal Noise in Atomic Force Microscopy," *Nanotechnology*, vol. 6, no. 1, pp. 1–7, 1995.

[168] E. D. Lemma *et al.*, "Mechanical Properties Tunability of Three-Dimensional Polymeric Structures in Two-Photon Lithography," *IEEE Trans. Nanotechnol.*, p. 1, 2016.

[169] J. Qu, M. Kadic, A. Naber, and M. Wegener, "Micro-Structured Two-Component 3D Metamaterials with Negative Thermal-Expansion Coefficient from Positive Constituents," *Sci. Rep.*, vol. 7, no. 1, p. 40643, 2017.

[170] K. Cole *et al.*, *Heat Conduction Using Green's Functions, 2nd Edition*. CRC Press, 2010.

[171] C. Lienau, A. Richter, and T. Elsaesser, "Light-Induced Expansion of Fiber Tips in near-Field Scanning Optical Microscopy," *Appl. Phys. Lett.*, vol. 69, p. 325, 1998.

[172] OFS Fitel, "AllWave® FLEX Zero Water Peak (ZWP) Single-Mode Ocean Fibers On OFS." [Online]. Available: http://fiber-optic-catalog.ofsoptics.com/item/single-mode-optical--fibers/ocean-fibers-2/flex-zero-water-peak-zwp-single-mode-ocean-fibers. [Accessed: 27-Jul-2017].

[173] M. R. Billah *et al.*, "Hybrid Integration of Silicon Photonics Circuits and InP Lasers by Photonic Wire Bonding," *Optica*, vol. 5, no. 7, p. 876, 2018.

[174] D. Taillaert *et al.*, "Grating Couplers for Coupling between Optical Fibers and Nanophotonic Waveguides," *Jpn. J. Appl. Phys.*, vol. 45, no. 8 A, pp. 6071–6077, 2006.

[175] Europractice, "EUROPRACTICE Si-Photonics Foundries and Technologies." [Online]. Available: https://europractice-ic.com/mpw-prototyping/siphotonics/. [Accessed: 07-Apr-2019].

D. Abbreviations and Symbols

D.1 Abbreviations

Apprehensions are presented in alphabetical order.

3D	Three-dimensional
AFM	Atomic force microscopy
AO	Adaptive optics
AOM	Acousto optical modulator
AR	Anti-reflective
Au	Gold
AWG	Arrayed waveguide grating
CWDM	Coarse wavelength division multiplexing
DETC	7-Diethylamino-3-thenoylcoumarin
DF	Deformable mirror
DFB	Distributed-feedback lasers
DR	Displacement ratio
EDFA	Erbium-doped fiber amplifier
FBG	Fiber Bragg grating
FC/APC	Fiber connecter angled physical contact
IC	Integrated circuit
FL	Freeform lens
fs	Femtosecond
FWHM	Full width at half maximum
HOPG	Cleaved highly oriented pyrolytic graphite

IFU	Integral field unit
InP	Indium phosphide
IR	Infrared
LA	Lens array
LD	Laser diode
LED	Light-emitting diode
LIDAR	Light distance and ranging
LIFT	Laser-induced Forward Transfer
LIMOS	Low index-contrast micro-optical system
LQG	Linear Gaussian control
MCF	Multi-core fiber
MCM	Multi-chip-module
MEMS	Micro-electro-mechanical system
MFD	Mode field diameter
MMF	Multi-mode fiber
MOB	Micro-Optical Bench
MOD	Modulator
MOFA	Micro-optical freeform assembly
MPO	Multi-fiber push on
MPW	Multi-project wafer
NA	Numerical aperture
OCT	Optical coherence tomography
PAC	Photo acid generator
PIC	Photonic integrated chip
ps	Picosecond

PSF	Point-spread-function
PWB	Photonic wire bonds
RIN	Relative intensity noise
RIN	Relative intensity noise
RMS	Root-mean-square
SEM	Surface electron microscopy
Si	Silicon
SiN	Silicon nitride
SiP	Silicon photonic
SMF	Single-mode fiber
SNOM	Scanning near-field optical microscopy
SOI	Silicon on insulator
SPM	Scanning probe microscopy
STED	Stimulated emission depletion
TIR	Total internal reflection
UV	Ultraviolet
VCSEL	Vertical cavity surface-emitting laser

D.2 Symbols

Greek symbols are presented in alphabetical order.

A	Half opening angle of a focused beam
β	Free-space propagation constant
γ	Slope of the contrast function
$\Delta z_{\mathrm{M}}, \Delta z, \Delta l_{\mathrm{C,meas}}$	Displacement
Δx	Dimension

δ	Displacement
η	Coupling efficiency
λ	Wavelength
ρ	Density
$\sigma_{\mathrm{f}}, \sigma_{\mathrm{h}}, \sigma_{\eta}$	Standard derivation
$\tau_{\mathrm{exp.}}$	Exposure time
$\tau_{\mathrm{exp,1}}, \tau_{\mathrm{exp,2}}$	Time for scanning along one line

Latin symbols are presented in alphabetical order.

A	Half extension of the voxel transversal (to *z*-)direction
a'	Offset due to radical diffusion transversal (to *z*-)direction
a_0, a_2, a_4, a_6, a_8	Coefficients
A_0, A_2, A_3, A_4	Fitting coefficients
A_N / n	Numerical aperture
b	Half extension of the voxel in axial (*z*-)direction
b'	Offset due to radical diffusion in axial (*z*-)direction
b_0, b_2, b_4, b_6, b_8	Coefficients
c_{AFM}	Spring constant
C	Degree of conversion
d_{l}	Distance between layers
d_{s}	Distance between scanning lines
D	Two-photon dose
DR	Displacement ratio
E	Youngs modulus
f_{r}	Resonance frequency
$f, f_{\mathrm{i}}, f_{\mathrm{Total}}$,	Focal length
$h(\mathrm{r},t)$	Solution of heat equation

h(f)	Fourier transform of h with respect to time
h_1, h_2	Heights
h_C	Thermal conductance
I_{Laser}	Optical intensity
I	Current
I_t	Threshold current
l_c	Distance
L	Distance
M_I	Mirror
m	Integer number
n, n_0	Refractive index
N	Integer number
p	Power density distribution
P_1, P_2	Points
P_m, P_C	Points
P, P_H	Power
P_1, P_2, P_S	Optical power
Q	Quality factor
$\mathbf{r}$	Position vector
r, r_1	Radius
R, R_{total}	Reflectivity
s	Spin
S	Signal
t	Time
T	Artifact
u	Energy density distribution
x, y, z	Cartesian coordinates

x_t, y_t, z_t	Cartesian coordinates
x_1, y_2, z_3	Cartesian coordinates

Danksagung

Diese Promotion entstand in den Jahren 2014 bis 2020 am Institut für Photonik und Quantenelektronik (IPQ) und am Institut für Mikrostrukturtechnik (IMT).

An erster Stelle möchte ich mich bei meinem Doktorvater Prof. Christian Koos für die ausgezeichnete Betreuung und Ausbildung während meiner Promotion bedanken. Ich schätze den persönlichen Einsatz, den hohen Anspruch an die Qualität wissenschaftlicher Arbeit und die unzähligen hilfreichen Diskussionen sehr. Insbesondere möchte ich mich auch für das außergewöhnliche Vertrauen und die Freiheit, neue Themenfelder zu erkunden, bedanken.

Ebenso möchte ich mich bei Prof. Wolfgang Freude bedanken für die zahlreichen Besprechungen von Manuskripten, die offenen und hilfreichen Anregungen sowie die Geduld und Sorgfalt bei Gesprächen jeglicher Art.

Insbesondere möchte ich mich bei Prof. Hendrik Hölscher für die gemeinsame Arbeit am Thema 3D-gedruckter Rastersondenmikroskope bedanken. Weiterhin möchte ich mich bei Prof. Sebastian Randel für die Unterstützung meiner Arbeit und die erfolgreiche Zusammenarbeit bedanken.

Weiterhin möchte ich mich bei allen Kollegen und Kooperationspartnern für die Zusammenarbeit, die vielen hilfreichen Gespräche und Unterstützung bedanken. Allen voran Florian Rupp, Gerald Göring, Norbert Schneider, Matthias Blaicher, Muhammad Rodlin Billah, Tobias Hoose, Yilin Xu, Nicole Lindenmann, Mareike Trappen, Simon Schneider, Aleksandar Nesic und Pascal Maier.

Besonders bedanken möchte ich mich bei allen Kollegen am Institut für Photonik und Quantenelektronik und am Institut für Mikrostrukturtechnologie: Carsten Eschenbaum, Christoph Füllner, Lothar Hahn, Denis Ganin, Stefan Singer, Wladislaw Harmann, Kira Köhnle, Yasar Kutuvantavida, Tobias Harter, Clemens Kieninger, Daria Kohler, Matthias Lauermann, Pablo Marin-Palomo, Sasha Mühlbrandt, Claudius Weimann, Tobias Wienhold, Stefan Wolf, Sentayehu Fetene Wondimu und Heiner Zwickel.

Bedanken möchte ich mich auch bei Bernadette Lehmann, Andrea Riemensperger, Maria-Luise Koch und Tatiana Gassmann für die administrative

Unterstützung und bei Oswald Speck, Volker Bös, Lisa Nolte, Martin Winkeler und Steffen Pfeifer für die technische Unterstützung.

Vielen Dank an Mareike Trappen, Ingo Reuter, Simon Stöhr, Jürgen Mathes, Dazhong Sun, Andrei Krochin, Christian Bremauer, Manuel Steidle, Johannes Wörle, Lukas Hampel, Lydia Yatcheva und Shishir Chandrasheklarholla, deren Arbeiten ich betreuen durfte und die wesentlich zum Erfolg dieser Promotion beigetragen haben.

Ganz besonders möchte ich mich bei meiner Schwester Anastasia für das detaillierte und sehr hilfreiche Korrekturlesen bedanken sowie bei meiner Frau Anna, meiner Tochter Katharina sowie meinen Eltern Dagmar und Christoph für die Unterstützung und Geduld während meiner Promotion und für das Verständnis, wenn „Papa weg!“ war.

List of Publication

Journal publication

Only journal publications that are part of this work or directly related to this work are listed here in chronological order and labeled [J…].

[J1] Trappen, M.; Blaicher, M.; **Dietrich, P.-I.;** Dankwart, C.; Xu, Y.; Hoose, T.; Billah, M. R.; Abbasi, A.; Baets, R.; Troppenz, U.; Theurer, A.; Woerhoff, K.; Seyfried, M.; Freude, W.; Koos, C. “3D-Printed Optical Probes for Wafer-Level Testing of Photonic Integrated Circuits” *Opt. Express* **28**, 37996-38007, 2020.

[J2] **Dietrich**[5]**, P.-I.**; Göring[5], G.; Trappen[5], M.; Blaicher, M.; Freude, W.; Schimmel, T.; Hölscher, H.; Koos, C. "3D-Printed Scanning-Probe Microscopes with Integrated Optical Actuation and Read-Out," *Small* **16**, 1904695, 2019.

[J3] **Dietrich, P.-I.**; Blaicher, M.; Reuter, I.; Billah, M. R.; Hoose, T.; Hofmann, A.; Caer, C.; Dangel, R.; Offrein, B.; Troppenz, U.; Möhrle, M.; Freude, W.; Koos, C. "In situ 3D Nanoprinting of Free-Form Coupling Elements for Hybrid Photonic Integration," *Nat. Photonics* **12**, 241-247, 2018.

[J4] **Dietrich**[5]**, P.-I.**; Harris[5], R. J.; Blaicher, M.; Corrigan, M. K.; Morris, T. M.; Freude, W.; Quirrenbach, A.; Koos, C. "Printed Freeform Lens Arrays on Multi-Core Fibers for Highly Efficient Coupling in Astrophotonic Systems," *Opt. Express* **25**, 18288-18295, 2017.

[5] Contributed equally.

[J5] Göring[5], G.; **Dietrich[5], P.-I.**; Blaicher, M.; Sharma, S.; Korvink, J.; Schimmel, T.; Koos, C.; Hölscher, H. "Tailored Probes for Atomic Force Microscopy Fabricated by Two-Photon Polymerization," *Appl. Phys. Lett.* **109**, 063101, 2016.

[J6] Schneider, S.; Lauermann, M.; **Dietrich, P.-I.**; Weimann, C.; Freude, W.; Koos, C. "Optical Coherence Tomography System Mass-Producible on a Silicon Photonic Chip," *Opt. Express* **24**, 1573-1586, 2016.

Patent publications

[P1] Koos, C; Hoose, T.; **Dietrich, P.-I.**; Blaicher, M.; Gödecke, M.; Lindenmann, N. (2016). Verfahren und Vorrichtung zur lithographischen Erzeugung einer Zielstruktur an einer nichtplanaren Ausgangsstruktur (DE102016214606B3).

[P2] Lauermann, M.; Koos, C; **Dietrich, P.-I.**; (2018). Vorrichtung und Verfahren zur optischen Charakterisierung oder Bearbeitung eines Objekts (DE102018221670A1).

[P3] **Dietrich, P.-I.**; Koos, C; Blaicher, M.; Reuter, I. (2016). Verfahren zur Herstellung eines optischen Systems und optisches System (DE102016221464A1).

[P4] **Dietrich, P.-I.**; Gerald, G.; Blaicher, M.; Trappen, M.; Hölscher, H.; Koos, C. (2017). Mikro-Optomechanisches System und Verfahren zu seiner Herstellung (DE102017221952B3).

[P5] Schneider, N.; Worgull, M.; Koos, C; **Dietrich, P.-I.**; Verfahren zur Herstellung eines Formkörpers (DE102018208273A1).

Conference publications

Conference contributions that present content not covered by journal publication and are based or directly related to this work are labeled [C…].

[C1] Trappen, M.; **Dietrich, P.-I.**; Burger, P.; Blaicher, M.; Göring, G.; Schimmel, T.; Freude, W.; Hölscher, H.; Koos, C. "AFM engine with optical actuation and readout printed on the facet of a multi-core fiber," in *Conference on Lasers and Electro-Optics (CLEO)*, 2020 , paper SM2N.7.

[C2] Blaicher, M.; Billah, M. R.; Hoose, T.; **Dietrich, P.-I.**; Hofmann, A.; Randel, S.; Freude, W.; Koos, C. "3D-Printed Ultra-Broadband Highly Efficient Out-of-Plane Coupler for Photonic Integrated Circuits," in *Conference on Lasers and Electro-Optics (CLEO)*, 2018, paper STh1A.1.

[C3] **Dietrich, P.-I.**; Reuter, I.; Blaicher, M.; Schneider, S.; Billah, M. R.; Hoose, T.; Hofmann, A.; Caer, C.; Dangel, R.; Offrein, B.; Möhrle, M.; Troppenz, U.; Zander, M.; Freude, W.; Koos, C. "Lenses for Low-Loss Chip-to-Fiber and Fiber-to-Fiber Coupling Fabricated by 3D Direct-Write Lithography," in *Conf. on Lasers and Electro-Optics (CLEO)*, 2016 paper SM1G.4.

[C4] **Dietrich, P.-I.**; Wondimu, S. F.; Wienhold, T.; Steidle, M.; Hofmann, A.; Lindenmann, N.; Billah, M. R.; Hoose, T.; Blaicher, M.; Freude, W.; Koos, C. „Herstellung mikrooptischer Komponenten durch Zwei-Photonen-Polymerisation," in *Mikro System Technik-Kongress*, 2015, paper 1570106799.